

UNIVERSIDADE FEDERAL DE MINAS GERAIS  
Instituto de Ciências Exatas  
Programa de Pós-graduação em Física

Nestor Javier Fajardo Reina

**Structural, electronic and mechanical  
properties of two-dimensional silica  $SiO_2$**

Belo Horizonte

2023

Nestor Javier Fajardo Reina

**Structural, electronic and mechanical  
properties of two-dimensional silica  $SiO_2$**

Tese de doutorado apresentada ao Programa de Pós-graduação em Física da Universidade Federal de Minas Gerais como requisito parcial para a obtenção do título de Doutor em Física.

Orientador: Prof. Dr. Ricardo Wagner Nunes

Belo Horizonte

2023

Dados Internacionais de Catalogação na Publicação (CIP)

F175s Fajardo Reina, Nestor Javier.  
Structural, electronic and mechanical properties of two-dimensional silica SiO<sub>2</sub>  
/ Nestor Javier Fajardo Reina. – 2023.  
123f. : il.

Orientador: Ricardo Wagner Nunes.  
Tese (doutorado) – Universidade Federal de Minas Gerais,  
Departamento de Física.  
Bibliografia: f. 113-123.

1. Silica. 2. Estrutura eletrônica. 3. Defeitos pontuais. 4. Propriedades mecânicas. I. Título. II. Nunes, Ricardo Wagner. III. Universidade Federal de Minas Gerais, Departamento de Física.

CDU – 539.2 (043)



UNIVERSIDADE FEDERAL DE MINAS GERAIS  
INSTITUTO DE CIÊNCIAS EXATAS  
PROGRAMA DE PÓS-GRADUAÇÃO EM FÍSICA

### ATA DE DEFESA DE TESE

**ATA DA SESSÃO DE ARGUIÇÃO DA 413ª TESE DO PROGRAMA DE PÓS-GRADUAÇÃO EM FÍSICA, DEFENDIDA POR NESTOR JAVIER FAJARDO REINA** orientado pelo professor Ricardo Wagner Nunes, para obtenção do grau de **DOUTOR EM CIÊNCIAS, área de concentração Física**. Às 14 horas de vinte e oito de fevereiro de dois mil e vinte e três reuniu-se, por videoconferência, a Comissão Examinadora, composta pelos professores **Ricardo Wagner Nunes** (Orientador - Departamento de Física/UFMG), **Bernardo Ruegger Almeida Neves** (Departamento de Física/UFMG), **Edmar Avellar Soares** (Departamento de Física/UFMG), **Pedro Paulo de Mello Venezuela** (Instituto de Física/UFF) e **Rodrigo Barbosa Capaz** (Instituto de Física/UFRJ), para dar cumprimento ao Artigo 37 do Regimento Geral da UFMG, submetendo o Mestre **NESTOR JAVIER FAJARDO REINA** à arguição de seu trabalho de Tese de Doutorado, que recebeu o título de "**Structural, electronic and mechanical properties of two-dimensional silica SiO<sub>2</sub>**". O candidato fez uma exposição oral de seu trabalho durante aproximadamente 50 minutos. Após esta, os membros da comissão prosseguiram com a sua arguição, e apresentaram seus pareceres individuais sobre o trabalho, concluindo pela aprovação do candidato.

Belo Horizonte, 28 de fevereiro de 2023.

Prof. Ricardo Wagner Nunes  
Orientador do estudante  
Departamento de Física/UFMG

Prof. Bernardo Ruegger Almeida Neves  
Departamento de Física/UFMG

Prof. Edmar Avellar Soares  
Departamento de Física/UFMG

Prof. Pedro Paulo de Mello Venezuela  
Instituto de Física/UFF

Prof. Rodrigo Barbosa Capaz  
Instituto de Física/UFRJ

**Candidato:** Nestor Javier Fajardo Reina

Documento assinado eletronicamente por **Nestor Javier Fajardo Reina, Usuário Externo**, em 01/03/2023, às 10:10, conforme horário oficial de Brasília, com fundamento no art. 5º do [Decreto nº 10.543, de 13 de novembro de 2020](#).



Documento assinado eletronicamente por **Bernardo Ruegger Almeida Neves, Professor do Magistério Superior**, em 01/03/2023, às 13:57, conforme horário oficial de Brasília, com fundamento no art. 5º do [Decreto nº 10.543, de 13 de novembro de 2020](#).



Documento assinado eletronicamente por **Ricardo Wagner Nunes, Professor do Magistério Superior**, em 01/03/2023, às 19:37, conforme horário oficial de Brasília, com fundamento no art. 5º do [Decreto nº 10.543, de 13 de novembro de 2020](#).



Documento assinado eletronicamente por **Rodrigo Barbosa Capaz, Usuário Externo**, em 03/03/2023, às 14:26, conforme horário oficial de Brasília, com fundamento no art. 5º do [Decreto nº 10.543, de 13 de novembro de 2020](#).



Documento assinado eletronicamente por **Edmar Avellar Soares, Professor do Magistério Superior**, em 06/03/2023, às 11:27, conforme horário oficial de Brasília, com fundamento no art. 5º do [Decreto nº 10.543, de 13 de novembro de 2020](#).



A autenticidade deste documento pode ser conferida no site [https://sei.ufmg.br/sei/controlador\\_externo.php?acao=documento\\_conferir&id\\_orgao\\_acesso\\_externo=0](https://sei.ufmg.br/sei/controlador_externo.php?acao=documento_conferir&id_orgao_acesso_externo=0), informando o código verificador **2110412** e o código CRC **9BB636A0**.

# Agradecimentos

Ao Senhor Jesus-Cristo pelo carinho e a esperança sempre renovada em promesas eternas e escritas na Sagrada Escritura que é inerrante, permanente, viva e eficaz.

A minha família da Colômbia: meu Pai Nestor e minha mãe Luz Teresa pelo apoio constante e livre de toda expectativa, me considero muito privilegiado por ter eles na minha vida, a pesar da distância, sempre presentes. Aos meus irmãos Angélica e Alejandro pelo carinho e apoio na distância. Que o Senhor Jesus-Cristo cuide, proteja e abençoe vocês abundantemente.

A Márcia minha esposa, um exemplo constante de coragem, determinação e perseverança no meio das dificuldades. Que o Senhor Jesus-Cristo te abençoe e me permita seguir disfrutando de tua companhia por longos anos cheios de vida e saúde.

Ao Ricardo, meu orientador que sabe encontrar em pequenos resultados perolas preciosas e esperanças de possibilidades futuras. Ele tem me apoiado no meio de variados desafios externos sempre com alegria, esperança e confiança. Tive o privilegio de contar com seu apoio econômico quando acabou a bolsa de estudos e começou a pandemia, até a finalização de este trabalho, sem este apoio teria sido impossível a continuação e finalização do mesmo. Que o Senhor Jesus-Cristo te abençoe Ricardo pelo carinho além de toda expectativa, o exemplo de calidez e grande humanidade, que voce possa desfrutar de longos anos, lucidez mental e saúde ao lado de aqueles que você ama.

Ao Pastor Edmir Guimarães e à Igreja Batista Anel de Selar, pelo carinho e apoio constante. O Pastor Edmir nos ajudou a mim e a minha esposa para encontrar um lugar mais sadio para morar e viver, numa fase de intensas dificuldades que tivemos de enfrentar. Pastor Edmir, que o Senhor Jesus-Cristo a vida verdadeira que foi manifestada continue sendo a luz que guia os seus passos e os destinos da Igreja, bênçãos sem medida para você e sua família.

Aos colegas do grupo de Estrutura Eletrônica, em primeiro lugar ao Matheus pela ajuda sempre oportuna em relação ao cluster, solucionando diversidade de problemas. Ao Ananias que muito me ajudou com metodologias de aplicação de stress-strain no SIESTA, ao Orlando que também me ajudou muito nos primeiros passos. Ao Samuel pelo carinho e amizade. Aos meninos novos: Hiago, Eduardo, Leonardo e Davi pela companhia durante esta fase final do meu trabalho.

Aos professores do grupo de Estrutura Eletrônica, especialmente ao professor Chacham em relação com intuições profundas respeito do material que estudamos, ele foi sempre uma guia constante. Á professora Simone pelo carinho e simpatia. Também ao professor Mario Mazzoni pela disponibilidade e simplicidade, e pelo excelente curso de Estado sólido. Aos

estudantes do Mario: Guilherme, Alan e Titú, pela proximidade e carinho.

Aos colegas da física: Wilmer, Bárbara, Dani, Ana Clara, Filomeno e Leonardo, pelo carinho e companhia. Quero agradecer especialmente ao Renan, pela amizade, ajuda e humanidade.

A todos os professores do departamento, especialmente em esta fase final ao Professor Ado Jorio, à Professora Sílvia Helena e às secretarias da posgraduação Ana e Marília, pela paciência, compreensão e apoio, extendendo os prazos além do possível para que nós pudéssemos terminar este trabalho.

A Gislene da Biblioteca pela simplicidade, o carinho e ajuda sempre que foi preciso.

Ao CNPq pelo apoio financeiro durante o tempo dos 4 anos de duração da bolsa.

*"E disse-me:  
A minha graça te basta,  
porque o meu poder se aperfeiçoa na fraqueza".  
(Bíblia Sagrada, 2 Coríntios 12, 9)*



# Resumo

Neste trabalho são estudadas as propriedades estruturais, eletrônicas e mecânicas de uma bicamada de SiO<sub>2</sub> bidimensional, considerando defeitos pontuais nativos e impurezas substitucionais: Al, B e P, assim como alguns defeitos topológicos. Este estudo é realizado usando a metodologia da teoria do funcional da densidade (DFT) como implementado nos softwares SIESTA e VASP. Identificamos uma marcada tendência à formação de estados de defeito fortemente localizados no gap de energia assim como ressonâncias fortemente localizadas nas bandas de valência e de condução, com certa independência do fato dos estados ser rastos ou profundos dentro do gap. Estes estados altamente localizados são consequência do confinamento quântico e o fortalecimento da interação de Coulomb, em este sistema bidimensional. A rede da sílica 2D responde localmente às deformações induzidas pelos defeitos pontuais estudados, que temos explicado postulando excitações de baixa energia: modos de tressura e de rotação. Acreditamos que estes modos estão em profunda relação com a resposta mecânica da sílica 2D. As vacâncias de oxigênio e o oxigênio intersticial se comportam como centros de captura de carga anfotéricos na sílica 2D. A impureza de Al induz separação de spin, mostrando um grau diferente de localização para cada canal de spin. O defeito Stone-Wales (SW) mostra um comportamento inesperado: é energeticamente mais favorável virar as duas camadas, que virar somente uma. Usando a metodologia proposta por Wu, Zhang e Pantelides (WZP), mostramos que, quando dopado com fósforo, são permitidos unicamente o estado neutro e o negativamente carregado. A sílica 2D exibe um comportamento mecânico singular: como os silicatos 3D ( $\alpha$ -quartz), na região linear mostra dois regimes diferentes de elasticidade, e em contraste, a sílica 2D mostra uma ampla faixa de resposta elástica, tendo a capacidade de retornar ao estado fundamental não deformado partindo de altos valores de deformação, tanto na direção ZZ quanto na direção AC. A superfície de energia deste sistema possui muitos estados metaestáveis, e a transição entre eles pode ser explicada pelo envolvimento dos graus de liberdade associados aos modos de tressura e rotação das ligações Si-O-Si. Neste trabalho propomos que uma espécie de hiperelasticidade neste material é dirigida, não pelos mecanismos usuais, tais como formação de discordâncias ou fluxo plástico, mas por transições induzidas pela deformação, onde o sistema começa uma nova resposta elástica a partir de um mínimo novo oferecido pela superfície de energia.

**Palavras-chave:** Sílica 2D. Estrutura eletrônica de defeitos pontuais. Propriedades mecânicas em sílica bidimensional. Resposta mecânica anômala. Stress-strain em sílica 2D. Hiperelasticidade. Native defects. Defeitos substitucionais. Estados rastos. Estados profundos.

# Abstract

Structural, electronic and mechanical properties of pristine 2D-SiO<sub>2</sub> bilayer, considering neutral native defects, and substitutional impurities: Al, B and P, and also some topological defects, have been addressed, by employing the Kohn-Sham DFT approach as implemented in SIESTA and VASP softwares. We identify a marked tendency for the appearance of strongly spatially localized defect states in the energy gap and resonances in the valence and conduction bands, with some independence of being shallow or deep within the band gap. This highly located states are consequence of quantum confinement and enhanced Coulombic effects in this 2D system. The 2D-SiO<sub>2</sub> lattice responds locally to the induced deformation in the studied point defects, and we propose low energy structural excitations: scissor and rotation modes as responsible. We believe these soft modes are in deep relation with the mechanical response of 2D-SiO<sub>2</sub>. Oxygen vacancies and single interstitials are found to be amphoteric trapping centers in 2D-SiO<sub>2</sub>. The aluminium impurity induces spin separation, showing a different degree of localization of each spin channel. The Stone-Wales (SW) defect shows an interesting behaviour: it is energetically more feasible to turn both layers than to turn just one. Using the Wu, Zhang and Pantelides's (WZP) methodology we show that only neutral and negative charged states are allowed in the phosphorus impurity. The 2D-SiO<sub>2</sub> bilayer displays a singular mechanical behaviour: as in the 3D counterpart ( $\alpha$ -quartz), exhibits two different elastic linear regimes; and in contrast, 2D-SiO<sub>2</sub> exhibits a wide range of elastic response, being able to return to the unstrained ground state starting from large strains in ZZ and AC directions. The energy surface of this system exhibits many available metastable states, and the transit between them can be driven by scissor and rotation degrees of freedom associated with the Si-O-Si bonds. We propose a kind of hyperelasticity in this material is driven not by usual mechanisms such as formation of dislocations or plastic flow, but by strain-induced transitions, where the system starts a new elastic response from a new minimum offered by the many-minima energy surface.

**keywords:** 2D silica. Electronic structure of point defects. Mechanical properties in 2D materials. Anomalous mechanical response. Stress-strain in 2D silica. Hyperelasticity. Native defects. Substitutional defects. Shallow states. Deep states.

# Contents

<b>Introduction</b>	<b>12</b>
<b>I Theoretical Foundations</b>	<b>20</b>
<b>1 Density functional theory</b>	<b>21</b>
1.1 Hohenberg-Kohn theorems . . . . .	21
1.2 Kohn-Sham equations . . . . .	24
1.3 Two kinds of electrons and two kinds of basis: wave planes and atomic orbitals	25
1.4 Exchange and correlation functional . . . . .	27
<b>2 Theory of elasticity</b>	<b>29</b>
2.1 Basics in theory of elasticity . . . . .	29
2.2 Information contained in stress-strain curves . . . . .	31
2.3 Units and orders of magnitude . . . . .	32
<b>3 Theory of defects</b>	<b>34</b>
3.1 General theory of point defects . . . . .	34
3.2 States induced by point defects . . . . .	35
3.2.1 Effective Mass Theory: EMT states . . . . .	37
3.2.2 Resonant scattering - states within the bands . . . . .	39
3.3 Theory of charged defects . . . . .	41
3.4 Fundamental approach: Wu, Zhang and Pantelides (WZP) . . . . .	44
<b>II Results</b>	<b>46</b>
<b>4 Native defects</b>	<b>47</b>
Introduction . . . . .	47
4.1 Methodology . . . . .	48
4.2 Vacancies . . . . .	49
4.2.1 Middle-Layer Oxygen Vacancy: $V_{\text{O}}^{\text{mid}}$ . . . . .	50
4.2.2 External-Layer Oxygen Vacancy: $V_{\text{O}}^{\text{ext}}$ . . . . .	52
4.2.3 Silicon Vacancy: $V_{\text{Si}}$ . . . . .	55

4.3	Interstitials . . . . .	57
4.3.1	Oxygen Split-Interstitials: $I_{\text{O}}^{\text{ext}}$ and $I_{\text{O}}^{\text{mid}}$ . . . . .	59
4.3.2	Silicon Interstitial: $I_{\text{Si}}$ . . . . .	62
4.4	Formation energy of vacancies and interstitials . . . . .	63
4.5	Partial Conclusions - native defects . . . . .	67
<b>5</b>	<b>Substitutional impurities</b>	<b>69</b>
	Introduction . . . . .	69
5.1	Substitutional Aluminium . . . . .	71
5.2	Substitutional Boron . . . . .	74
5.3	Formation Energy of substitutional impurities . . . . .	76
5.4	Partial Conclusions - substitutional impurities . . . . .	78
<b>6</b>	<b>Anomalous mechanical response of two-dimensional <math>\text{SiO}_2</math></b>	<b>79</b>
	Introduction . . . . .	79
6.1	The structural ground state of 2D- $\text{SiO}_2$ : methodological issues . . . . .	81
6.2	Anomalous response of 2D- $\text{SiO}_2$ to bending deformations . . . . .	86
6.3	Response of 2D- $\text{SiO}_2$ to quasi-static(QS) tensile uniaxial strain . . . . .	92
6.4	Partial conclusions - anomalous mechanical response of two-dimensional $\text{SiO}_2$ . . . . .	99
<b>7</b>	<b>Topological defects</b>	<b>101</b>
<b>8</b>	<b>Charged defects</b>	<b>103</b>
8.1	Partial Conclusions - Charged defects . . . . .	106
<b>9</b>	<b>Publications</b>	<b>108</b>
<b>10</b>	<b>Conclusion and perspectives</b>	<b>109</b>
	<b>Bibliography</b>	<b>112</b>

# Introduction

Looking at the many material structures presents in nature, additionally enriched with immense variety of colors, textures and hardnesses would lead us, in a first sight, to suppose that this unbelievable diversity is irreducible to a few fundamental bricks. Overstating the idea, and based in the external differences, we would conclude that there are as many materials as objects in nature. However, after Mendeleiev's periodic table, and subsequent developments, this immense variety was reduced to 118 chemical elementary bricks or atoms, each one of them, in turn, is reduced to protons, electrons and neutrons. This tremendous reduction from diversity in direction to unity, is made by paying a price: the number of individual identities of each substance is diminished. The fact that the positive charge is concentrated in a point, as was proved in the classical Rutherford's alpha-scattering experiments, allows each atomic species to carry its own chemical identity. On the other hand, the electronic cloud exhibits a more delocalized nature, leading the chemical identity in the hands of the electronic charge distribution, when a molecule or solid is built. This observations support the Dalton's atomic hypothesis: atoms retain their identity even when in chemical combination with other atoms. Thus, to define atoms in molecules is an identity problem that is in the root of density functional theory, and has been discussed by remarkable authors [1, 2], leading to other DFT schemes [3–5]. The prize of binding atoms is to deform the electronic cloud, more or less far from the spherically symmetric configuration. On the other side, the identity ambiguity introduced by the distortion of the free atom, being placed in a solid or molecule, lead us again to the world of rich multiplicity.

Within the atomic hypothesis, to build a piece of quartz, for instance, we join together  $\sim 10^{23}$   $\text{SiO}_2$  units in a regular arrangement. Each atom offers two types of electrons: those strongly bonded to the atomic nucleus, characterized by a more localized nature and by being chemically inert (core electrons); and the valence electrons, of a more delocalized nature, responsible for building the chemical bonds. Atoms are glued together with the valence electronic "jelly", through the cohesion energy coming from the compromise between: the attractive Coulomb force between electrons and ions, the repulsive force between electrons, the repulsive force between the ions and the electronic kinetic energy, leading to a stable minimum energy structure. This picture, modeled within the standard density Functional theory (DFT) is able to explain a great variety of physical properties: crystal structure, electrical behaviour, deformation response and mechanical properties, lattice vibrations, absorption spectrum, etc.

Stackings of two-dimensional (2D) materials that interact through van der Waals interactions (usually called van-der-Waals stackings) are the current paradigm for the investigations

of prospective electronic devices built from 2D materials, because they offer the possibility of modulating the electronic and structural properties of the ensuing materials along the stacking direction.

Over the last decade,  $\text{SiO}_2$  has been synthesized in 2D forms (2D- $\text{SiO}_2$ ) [6–9], with potential applications as a highly permselective membrane and also as a prototype material where the glass transition can be directly observed [10]. This 2D- $\text{SiO}_2$  bilayer is the thinnest possible system with  $\text{SiO}_2$  stoichiometry that is fully chemically saturated, i.e., devoid of dangling bonds. It interacts weakly with the substrates on which it is grown, via van der Waals interactions [6].

Being the thinnest possible chemically-saturated  $\text{SiO}_2$  layer, and a mechanically- and chemically-stable van-der-Waals-interacting 2D-material with an experimental band gap of 6.7 eV [6], the most important prospective application of a 2D- $\text{SiO}_2$  bilayer should be as an ultrathin insulating layer in van-der-Waals stackings.

As in most of the three-dimensional (3D) polymorphs of silica, 2D- $\text{SiO}_2$  is built from a structural motif of corner-sharing tetrahedra, where oxygen atoms in each of the four shared vertices are bonded to two silicon atoms in the centers of adjoining tetrahedra, resulting in a  $\text{SiO}_2$  stoichiometry. In the case of 2D- $\text{SiO}_2$ , this motif is structured as a bilayer consisting of two mirror-image layers of  $\text{SiO}_2$  tetrahedra sharing an oxygen layer in the middle. Oxygens in this middle layer sit on the vertices shared by the mirror-image tetrahedra from the “top” and “bottom” external layers, as shown in Fig. 1. On the two external layers, each oxygen atom sits on a vertex shared by two adjoining tetrahedra.

Systematic investigation of the fundamental physical properties of silicate-based 3D compounds have been of paramount importance in the development of silicon-based technology, ranging from fiber optics to semiconductor devices. In the solid form, three-dimensional  $\text{SiO}_2$  (3D- $\text{SiO}_2$ ) appears in several crystalline phases such as  $\alpha$ -quartz and  $\beta$ -quartz, among others, and also in amorphous phases such as natural silica, glass, and opal. Most of these 3D solids consist of networks of the aforementioned structural motif of corner-sharing tetrahedra. In the following paragraphs we will present results already obtained in this work in relation with the pristine 2D  $\text{SiO}_2$  bilayer.

The equilibrium structure of crystalline 2D- $\text{SiO}_2$  is a bilayer composed of two (top and bottom) mirror-image external layers, with nominal  $\text{Si}_2\text{O}_3$  stoichiometry, sharing an intermediate (or middle) layer of oxygen atoms. Oxygen atoms in the middle layer are bonded to two Si atoms, one directly above it in the top layer and another directly below it in the bottom layer, resulting in the overall  $\text{SiO}_2$  stoichiometry, as shown in Fig. 1. The Si atoms in each of the two external layers form AA-stacked honeycomb structures, with one oxygen atom in the middle of each Si-O-Si link, forming oxygen external sublayers. Overall, the lattice structure of 2D- $\text{SiO}_2$  is a hexagonal lattice with twelve atoms per primitive cell, belonging to the  $D_{6h}$  symmetry group, the same as graphene. The resulting values from our *ab initio* calculations for the structural parameters shown in Fig. 1 are included in Table 1. Si-O bonds involving a middle-layer O atom ( $d_{\text{Si-O}}^{\text{mid}} = 1.65 \text{ \AA}$ ) are slightly smaller than Si-O bonds involving an external-layer O atom ( $d_{\text{Si-O}}^{\text{ext}} = 1.67 \text{ \AA}$ ), both values being slightly larger than Si-O bonds

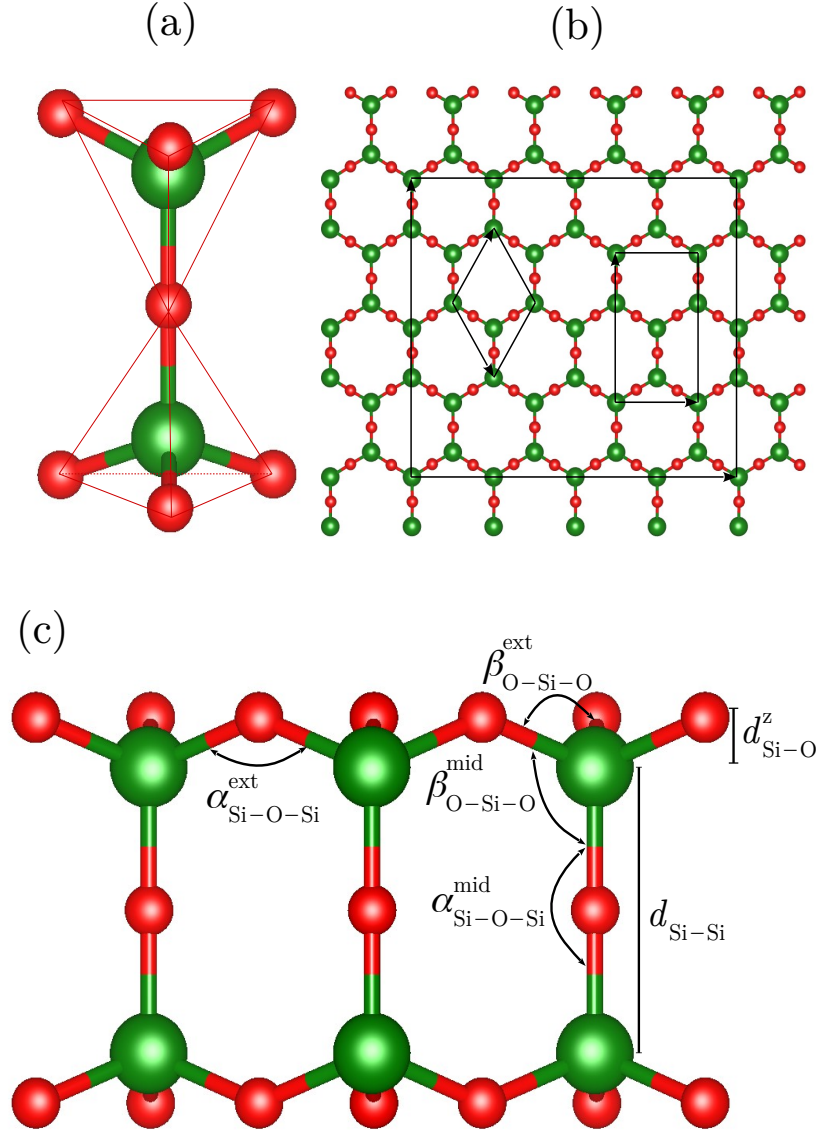


Figure 1: Atomic structure of a 2D-SiO<sub>2</sub> bilayer. (a) Side view of the structural motif of mirror-image tetrahedra sharing a vertex. Oxygen atoms (red spheres) sit on the vertices and silicon atoms (green spheres) at the center of each tetrahedron. (b) Top view of the 2D-SiO<sub>2</sub> bilayer. Si atoms form top and bottom AA-stacked honeycomb sublattices with an O atom in the middle of Si-O-Si links. The diamond-shaped primitive 12-atom cell, a rectangular 24-atom unit cell, and the 192-atom  $[(4 \times 2) \times \text{the rectangular unit cell}]$  supercell used in most of our calculations are indicated by black lines. (c) Side view showing the structural parameters of the 2D-SiO<sub>2</sub> bilayer. Definitions and values of the bond angles and bond lengths shown in the figure are included in Table I.

in 3D  $\alpha$ -quartz (1.61 Å). The tetrahedral O-Si-O angles involving one middle-layer O atom ( $\beta^{\text{mid}}_{\text{O-Si-O}} = 110.2^\circ$ ) are slightly larger than the O-Si-O angles with both O atoms on an external layer ( $\beta^{\text{ext}}_{\text{O-Si-O}} = 108.8^\circ$ ). The former (latter) are larger (smaller) than the ideal tetrahedral angle of  $109.5^\circ$  by  $0.7^\circ$  only. The Si-O-Si angle is  $\alpha^{\text{mid}}_{\text{Si-O-Si}} = 180^\circ$  for bonds joining Si atoms in the two sublayers, with an oxygen atom in the middle layer, and  $\alpha^{\text{ext}}_{\text{Si-O-Si}} = 139.6^\circ$

Table 1: Geometric parameters of the structure of a 2D-SiO<sub>2</sub> bilayer. Distances in Å and angles in degree. Available experimental values, in parenthesis, are from Refs. [11, 12].  $d_{\text{Si-Si}}$   $\equiv$  distance between the two external Si honeycomb layers.  $d_{\text{Si-O}}^{\text{ext}}$   $\equiv$  distance between nearest-neighbor Si and O atoms in the same external layer.  $d_{\text{Si-O}}^z$   $\equiv$  distance between Si and O sublayers in the same external layer.  $\alpha_{\text{Si-O-Si}}^{\text{ext}}$   $\equiv$  Si-O-Si angle at external-layer O atom vertex.  $\alpha_{\text{Si-O-Si}}^{\text{mid}}$   $\equiv$  Si-O-Si angle at intermediate-layer O atom vertex.  $\beta_{\text{O-Si-O}}^{\text{ext}}$   $\equiv$  tetrahedral O-Si-O angle involving external-layer O-atoms.  $\beta_{\text{O-Si-O}}^{\text{mid}}$   $\equiv$  tetrahedral O-Si-O angle involving one middle-layer O-atom.

$d_{\text{Si-Si}}$	$d_{\text{Si-O}}^{\text{ext}}$	$d_{\text{Si-O}}^z$	
3.30	1.67	0.58	
	(1.67±0.08, 1.66±0.06)	(0.55±0.04)	
$\alpha_{\text{Si-O-Si}}^{\text{ext}}$	$\alpha_{\text{Si-O-Si}}^{\text{mid}}$	$\beta_{\text{O-Si-O}}^{\text{ext}}$	$\beta_{\text{O-Si-O}}^{\text{mid}}$
139.6	180	108.8	110.2
(140.5)	(180)	(109.4±8.1, 110.1±5.7)	

for the Si-O-Si bonds with the three atoms on the same external layer. The distance between the two Si honeycomb sublayers is 3.30 Å. On each external layer, the O-atom sublayer is at a distance of 0.58 Å from the Si sublayer. All structural values are in very good agreement with the scanning-tunneling-microscopy (STM) results from Refs. [12], also included in Table 1.

The band structure and DOS of 2D-SiO<sub>2</sub> are shown in Fig. 2. In the top we show the electronic bands in the (-11.7, 2.0) eV interval, with the DOS shown on the right. In the lower panels we show separately the DOS for the valence (left panel) and conduction bands (right panel) in the corresponding energy intervals, as well as the PDOS of the atomic orbitals that give significant contributions to the electronic bands shown in the figure.

Unlike the case of  $\alpha$ -quartz, that has an indirect band gap (top of the valence band at the K and M points and bottom of the conduction band at the  $\Gamma$ -point, in the Brillouin zone) [13], in 2D-SiO<sub>2</sub> we obtain a direct gap with the two band extrema at the  $\Gamma$ -point. We recall that a transition from indirect to direct band gap, on going from the 3D to the 2D forms, occurs also in the case of 2D hexagonal metal dichalcogenides [14, 15].

The Kohn-Sham-GGA value we obtain for the fundamental band gap is 5.6 eV. An important difference we obtain, between the electronic bands of the 2D and 3D forms of SiO<sub>2</sub>, is the width of the highest part of the valence band, which is 3.2 eV in 3D  $\alpha$ -quartz [13] and only 0.9 eV in 2D-SiO<sub>2</sub>, which is indicative of enhanced correlation effects in the 2D form. Moving down in energy in the valence band, this narrow band is followed by a pseudogap of  $\sim 0.2$  eV, related to a region populated solely by highly dispersive bands (hence the low DOS). Moving further down in energy, we find another rather narrow ( $\sim 0.3$  eV) set of bands followed by another pseudogap, and yet another narrow set of bands, with a width of  $\sim 1.2$  eV. In this latter set of bands, at -1.73 eV below the top of the valence band ( $\epsilon_{vb}$ ), we observe a very strong van Hove singularity, associated to a set of flat bands in this energy range, that should give rise to a strong peak in the ultraviolet absorption signal of a 2D-SiO<sub>2</sub> layer. A true gap of  $\sim 0.3$  eV separates these bands from another set of bands, that display another pseudogap in their highest part.

The orbital composition of the valence bands, shown in Fig. 2(c) and Fig. 3(a), is similar



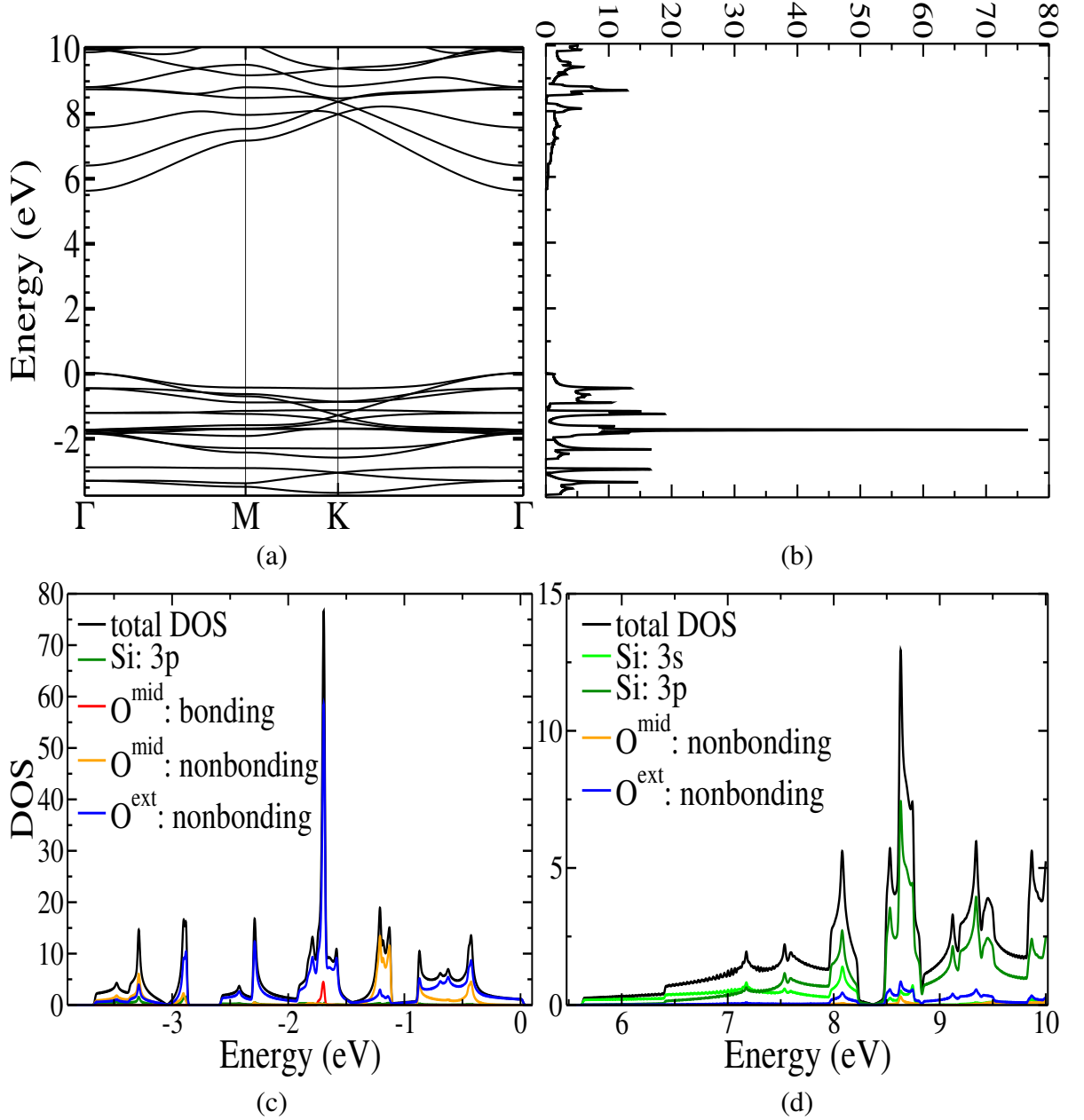


Figure 2: (a) Band structure and (b) density of states (DOS) of a 2D-SiO<sub>2</sub> bilayer. (c) DOS and orbital-projected density of states (PDOS) of the valence bands. (d) DOS and PDOS of the conduction bands. In all panels, the zero of the energy scale is at the top of the valence band.

to that of 3D-SiO<sub>2</sub>, being mostly derived from the nonbonding orbitals of the oxygen atoms. The orbital character of the strong van Hove singularity is essentially the nonbonding orbitals of the oxygen atoms from the external layers, with a small contribution from bonding orbitals of the middle-layer O atoms. This observation can be assured with more detail examining the local density of states of the van Hove singularity<sup>1</sup>, we find that effectively, the strong peak comes mainly from  $p_z$ -like orbitals on the external layer oxygens (see figure 4 and blue line in figure 2c), with a little contribution from middle layer oxygens (see figure 4 and red line in figure 2c). This is the only feature of the DOS of the three highest set of valence bands that has some contribution from bonding oxygen orbitals. Note that, overall, Si orbitals give

<sup>1</sup>We use a 0.02 eV energy window

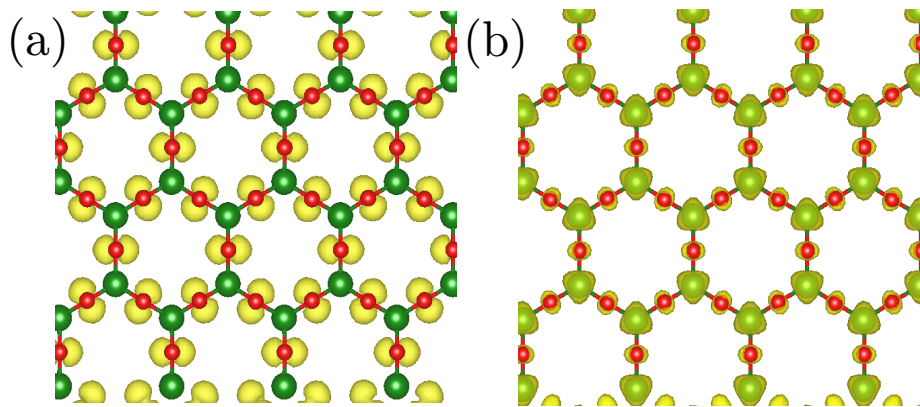


Figure 3: Isosurfaces of charge density for bands at (a) the top of the valence band and (b) bottom of conduction band. The top of the valence band shows an orbital composition dominated by the nonbonding orbitals from oxygen atoms, while the bottom of the conduction band is composed mainly of silicon bonding orbitals.

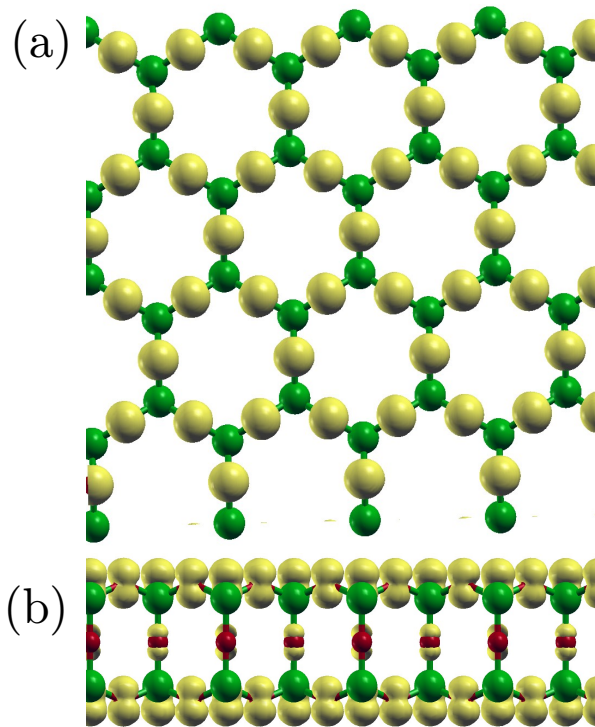


Figure 4: Isosurfaces of charge density at the van Hove singularity. (a) Top view of the van Hove orbitals. (b) Side view of the van Hove orbitals. The van Hove singularity comes mainly from  $p_z$ -like orbitals from oxygens on the external layers, plus a small contribution from  $p_z$ -like orbitals from oxygens in the middle layer.

a negligible contribution to the valence bands.

Regarding the conduction bands, the scenario is also similar to quartz, with the conduction bands being derived primarily from the  $s$  and  $p$  orbitals of the Si atoms, as shown in Fig. 2(d) and Fig. 3(b), for an interval of  $\sim 2.4$  eV up from the bottom of the conduction band ( $\epsilon_{cb}$ ). States at the bottommost part of the conduction band are nearly entirely derived from the Si

$s$  orbitals, and the conduction bands remain mostly of  $s$  character up to  $\sim 1.7$  eV above  $\varepsilon_{cb}$ . Moving up from this point, the states develop a predominant Si  $p$ -orbital character, with a progressively decreasing contribution of the Si  $s$  orbitals. Starting at  $\sim 2.4$  eV above  $\varepsilon_{cb}$ , the nonbonding orbitals of the external-layer O atoms give a small but sizeable contribution to the conduction-band states.

Several interesting properties emerge due to the 2D nature of the 2D-SiO<sub>2</sub> bilayer in contrast with  $\alpha$ -quartz, considered as a representative of the 3D behaviour. This work drew attention to the fact that defect states induced by point defects are influenced by quantum confinement and enhanced Coulombic effects. It is known that, often, exciton binding energies in lower dimensional systems are one or two orders of magnitude larger than in 3D crystals [16, 17], as a consequence to the weakened electronic screening associated with the 2D nature, leading to a more strong binding energy associated. Thus as our results have suggested to the 2D-SiO<sub>2</sub> silica, the defect's wave function of the electronic states introduced in the fundamental band gap and resonances induced into the edge of the valence and conduction bands, shown a strongly localized nature.

More interesting yet is to think of mechanical properties in the context of reduced dimensionality. 3D forms of quartz, glass and ceramics are known to be brittle materials [18], where the fracture induced by strain is nucleated by the preexisting microscopic cracks, leading to sudden fracture or also slow crack growth. The 2D-SiO<sub>2</sub>, in strike contrast with the brittle quartz, glass and ceramics, shows a wide range of elastic response. Just to have an idea, the elastic limit before plastic deformation, for a metal is  $\sim 0.2$  % [19], while our 2D-SiO<sub>2</sub> exhibits  $\sim 30$  % or more. In intuitive terms, the elastic range is governed by the "memory" that a material has respect to the unstrained structure, that acts as reference to the stored elastic energy and determines the restorative force, being able to lead the material to the initial relaxed geometry. This peculiar elastic behaviour, we have explained as driven by strain-induced transitions, with the capacity to recover the pristine geometry starting from a nanotube configuration or a high strained structure. It would be interesting to say that in shape memory alloys, such as Ni-Ti (nitinol) an emblematic example of superelasticity, the reversible strain rests on the happening of a martensitic transformation as a consequence of stress-induced transition [18, 20–22]. So it could be interesting doing more studies to mapping the complete stress-strain curve in the quasi-static(QS) regime, to 2D-SiO<sub>2</sub>, through ciclical loading and unloading sequences.

Our work has been divided in two main parts: the first, covering the theoretical foundations; and the second is devoted to the results. Within the theoretical foundations, we begin with the density functional theory, showing that the electronic density  $n_0(\mathbf{r})$  determines completely the problem. In what follows, within the elasticity theory are presented the basics of deformation theory and a remark of units and orders of magnitude. Subsequently, on the theory of defects chapter, we introduce the main ideas related with point defects in solids, states induced by point defects (in the gap and into the bands - resonances) and mass effective states. Finally, is introduced the theory of charged defects in two subsections: the first, describing the *ad hoc* method, that corrects the spurious Coulomb interactions, when exter-

nal charge are inserted; the second, introducing the more fundamental and consistent method developed by Pantelides et. al. [23] where external charges are not inserted in the system, but allowing the exchange of charges between the localized defect states and the delocalized states of the bands.

The results section, begins with the structure and charge density of defect states corresponding to several native defects. After this, as representatives of substitutional impurities, results involving Al and B in the place of Si are presented. Next, the anomalous response of this 2D material is studied, in contrast with some  $\alpha$ -quartz stress-strain behaviour, followed by the bending stiffness of 2D-SiO<sub>2</sub> bilayer, obtained through of building silica nanotubes. In what follows, study of quasi-static uniaxial strain-stress curves are presented. Consecutively, some preliminary results in formation energies from topological defects, observed in graphene and in other hexagonal two dimensional materials are presented. Finally, results to charged defects are presented in the case of substitutional phosphorus, taking into account the spin polarization, within the Wu, Zhang and Pantelides's fundamental approach [23].

Each results section is followed by partial conclusions, and at the final of the text general conclusions and perspectives of future developments are established.

# **Part I**

## **Theoretical Foundations**

# Chapter 1

## Density functional theory

The electric and mechanical behavior of a general system, as a molecule or solid is driven by the electric repulsion between strongly localized positive charges, partially screened by the 'electronic quantum glue' creating a stable structure with a minimum energy. The hamiltonian of the multielectronic system, in the Born-Oppenheimer approximation, is given by the kinetic electronic energy ( $\hat{T}$ ), the negative energy due to the attractive potential from the atomic nucleus ( $\hat{V}$ ), and the positive energy from the coulomb repulsion between the electrons ( $\hat{U}$ ):

$$\hat{H} = - \sum_{i=1}^N \frac{\hbar^2}{2m} \nabla_i^2 - \sum_{i,J} \frac{Ze^2}{|\mathbf{r}_i - \mathbf{R}_J|} + \frac{1}{2} \sum_{i \neq j} \frac{e^2}{|\mathbf{r}_i - \mathbf{r}_j|}. \quad (1.1)$$

We are looking for the ground state of the system:

$$\hat{H}|\Psi_0\rangle = E|\Psi_0\rangle. \quad (1.2)$$

The Density Functional Theory (DFT) is established on the fortunate fact that the ground state electronic density  $n_0(\mathbf{r})$ , contrary to expectations, contains exactly the same information that the ground state wave function  $\Psi(\mathbf{r}_1, \mathbf{r}_2, \dots, \mathbf{r}_N)$  [24]. In the Kohn-Sham (KS) scheme, the DFT methodology constructs the electronic density starting with single electron atomic orbitals, minimizing the energy of the system.

In the following, we present a review of the two fundamental theorems of Hohenberg e Kohn (HK), where it is demonstrated the formal equivalence between the Schrödinger equation and the DFT approach.

### 1.1 Hohenberg-Kohn theorems

In order to get a clear understanding about what is new in the DFT methodology, it is crucial to consider briefly the usual path to solve a quantum-mechanical problem [25]. To solve the Schrödinger equation, it is equivalent to solve the variational problem:

$$\delta[\langle\Psi|\hat{H}|\Psi\rangle - \lambda(\langle\Psi|\Psi\rangle - 1)] = 0, \quad (1.3)$$

Where  $\hat{H}$  is the hamiltonian of the system,  $\Psi$  is the wavefunction,  $\delta$  means the functional derivative of the quantity between the square brackets, and  $\lambda$  is the Lagrange multiplier that guarantees the extremization subject to the constrain required by the normalization of the wavefunction. The eigenstates of the Schrödinger equation are just those that make the energy of the system stationary, over variations of any wavefunction parameter. In the variational formulation, the true wavefunction of the ground-state is the only one which minimizes the energy functional. This functional depends on the external potential  $v(\mathbf{r})$  and the total number of electrons  $N$ , i.e., the energy is a *functional* of the  $N$  and  $v(\mathbf{r})$ .

$$E = E[N, v(\mathbf{r})] \quad (1.4)$$

The hamiltonian for a system of  $N$  electrons is completely determined by the external potential and the number of electrons. Further, the ground-state wavefunction is also so determined, and as a consequence, any observable of the system is fully determined. Different potentials  $v(\mathbf{r})$  produce different hamiltonians, leading to different ground-state wavefunctions, determining a unique solution of the system.

In the DFT method, we switch the couple  $N, v(\mathbf{r})$  as the independ variables to the electronic density  $n_0(\mathbf{r})$ .

$$E = E[n_0(\mathbf{r})]. \quad (1.5)$$

The ground-state electronic density  $n_0(\mathbf{r})$  is enough to determine the problem. In the first place, the electronic density determines the total number of electrons:

$$N = \int n_0(\mathbf{r}) d\mathbf{r}. \quad (1.6)$$

Secondly, the first HK theorem establishes that the external potential is determined uniquely (one to one) by the electronic density.

**Theorem 1** *First HK Theorem: the external potential has a one to one relationship with the ground-state electronic density. The external potential  $v(\mathbf{r})$  it is determined uniquely, except for an additive constant, by the electronic density of the ground-state  $n_0(\mathbf{r})$ . The external potential is a unique functional of the density.*

The demonstration is suspiciously simple, it consists in supposing that two different potentials lead to the same density. This hypothesis leads to a mathematical inconsistency [26] [27], and to the conclusion that each ground state density has one and only one associated external potential. This result assures the complete equivalence between the DFT method and the Schrödinger equation. The DFT method has to guarantee that the ground-state density  $n_0(\mathbf{r})$  is as good as the wavefunction to describe the ground-state, i.e., it is mandatory the existence of a unique density associated with a given external potential to have a unique solution that determines the problem without ambiguities.

This theorem has two corollaries: in the first place, determining the external potential without ambiguities, determines also the hamiltonian, and as a consequence the ground-state

wavefunction, i.e., the wavefunction is also an unique functional of the density. Secondly, since it is given that all observables can be calculated as the expected value in the ground state, it follows that all observables are also unique functionals of the density.

Between the physical observables, we can consider the energy of the system. Here it appears the second theorem of HK, affirming that the ground-state energy, as a functional of the electronic density, follows a variational principle [26] [27]. The energy calculated with any trial density, is bigger or equal than the true ground-state energy, obtained of course with the true ground-state density. This theorem is crucial to guide the practical way to get the true density.

**Theorem 2** *Second HK Theorem: variational energy principle.*

*To any trial density  $n(\mathbf{r})$  such that  $n(\mathbf{r}) \geq 0$  and  $\int n(\mathbf{r})d\mathbf{r} = N$ ,*

$$E_0 \leq E[n(\mathbf{r})], \quad (1.7)$$

*where*

$$E[n(\mathbf{r})] = \int n(\mathbf{r})v(\mathbf{r})d\mathbf{r} + F_{HK}[n(\mathbf{r})], \quad (1.8)$$

*and*

$$F_{HK}[n(\mathbf{r})] = \langle \Psi | \hat{T} + \hat{U} | \Psi \rangle. \quad (1.9)$$

To demonstrate this theorem looks, at the first sight unnecessary, because we already have a variational principle to the energy establishing the existence of the lower bound (equation 1.3). However it has to be demonstrated, because it has already been established considering the energy as a wavefunction functional, but right now we have the energy as a density functional. The proof was presented initially by Hohenberg and Kohn in their foundational paper [26], yet Levy [28] [29] and Lieb [30] give a more explicit and compact proposal, extending the functional domain from  $v$ -representable potentials to  $N$ -representable ones, also including the possibility of degenerate ground-states.

It is important to note that the  $F_{HK}$  functional is universal, i.e., it is independent of the external potential, relying only on the electronic kinetic energy and their mutual interactions. For this reason its functional form has to be the same for atoms, molecules and solids, likewise the functional form of the Hartree energy is the same for any system without dependence on the number of electrons.

To summarize we can say that to each external potential, for instance the periodic potential from the ions in a crystalline solid, there is associated a unique ground-state electronic density. Therefore the DFT presents an alternative, exact in principle, and efficient procedure to find the ground-state of a quantum many particle system. But yet there remains an important issue: how to build the electronic density? which wavefunctions can be used as a starting point? This question is answered by the Kohn-Sham scheme, that builds the density from single electron orbitals.



## 1.2 Kohn-Sham equations

In the winter of 1964, Kohn and Sham (KS) [31] [27], inspired by Hartree's job, had the idea to deal with the interacting many-electron system employing an auxiliary system of non-interacting electrons which includes all the interacting many body effects as an effective potential. The starting point of KS is the energy functional written in a convenient way:

$$E_v[n] = \int n_0(\mathbf{r})V(\mathbf{r})d\mathbf{r} + F[n], \quad (1.10)$$

where,

$$F[n] = \frac{1}{2} \int \int \frac{n(\mathbf{r})n(\mathbf{r}')}{|\mathbf{r} - \mathbf{r}'|} d\mathbf{r}d\mathbf{r}' + G[n], \quad (1.11)$$

with  $G[n]$  given by,

$$G[n] = T_s[n] + E_{xc}[n]. \quad (1.12)$$

Where  $T_s[n]$  is the kinetic energy functional related to a non-interacting electron system and  $E_{xc}[n]$  is the exchange-correlation functional that will be explained in more detail in the subsection 1.4. The key point of KS was to suggest as *ansatz* to the kinetic energy part, the expression valid for a non-interacting electron system:

$$n(\mathbf{r}) = \sum_{i=1}^N \psi_i^*(\mathbf{r})\psi_i(\mathbf{r}) \quad (1.13)$$

$$T_s[n] = -\frac{\hbar^2}{2m} \sum_{i=1}^N \int \psi_i(\mathbf{r})^* \nabla^2 \psi_i(\mathbf{r}). \quad (1.14)$$

The energy functional can be written as:

$$E[n] = T[n] + U[n] + V[n] = T_s[n[\psi_i]] + U_H[n] + E_{xc}[n] + V[n]. \quad (1.15)$$

With these definitions, we can see that the exchange-correlation energy is, by definition:

$$E_{xc}[n] = T[n] - T_s[n] + U[n] - U_H[n]. \quad (1.16)$$

By the first HK theorem, the density of the auxiliary non-interacting system has to lead to the same electron density of the interacting system. The minimization of the energy functional with respect to the density (now depending implicitly on the single electron orbitals), leads to the true electronic density of the interacting system. We aim to solve the variational problem:

$$\delta[E[n] - \sum_{i=1}^N \epsilon_i(\psi_i^*(\mathbf{r})\psi_i(\mathbf{r}) - 1)] = 0 \quad (1.17)$$

where  $\epsilon_i$  are the Lagrange multipliers that take into account the constraint imposed by

having a fixed number of electrons  $N$ . The variational principle of HK lead us to the KS equations:

$$\left\{ -\frac{1}{2}\nabla^2 + V_{eff}(\mathbf{r}) \right\} \psi_i = \epsilon_i \psi_i, \quad (1.18)$$

where:

$$n(\mathbf{r}) = \sum_{i=1}^N |\psi_i(\mathbf{r})|^2, \quad (1.19)$$

and

$$v_{eff}(\mathbf{r}) = v(\mathbf{r}) + \int d\mathbf{r}' \frac{n(\mathbf{r}')}{|\mathbf{r} - \mathbf{r}'|} + v_{xc}(\mathbf{r}). \quad (1.20)$$

The KS equations are a set of  $N$  coupled equations, one for each electronic orbital. They have to be solved selfconsistently, with respect to the electronic density. The selfconsistent condition is the convergence of the density, i.e., the electronic density has to be the same on the input and the output of the selfconsistent cycle <sup>1</sup>.

To describe explicitly the KS equations, we need a basis of single electron wavefunctions to be used as starting point for the selfconsistency process. We can commonly consider two kinds of basis functions to expand the electronic density employed in electronic structure: plane waves and atomic orbitals.

### 1.3 Two kinds of electrons and two kinds of basis: wave planes and atomic orbitals

Looking for the physics of the chemical bonds, we can simplify further the problem by realizing that involved in the bonds are essentially the valence electrons, while the core electrons remain chemically unactive, just screening the nucleus, thus providing an effective Coulomb potential where the valence electrons move in <sup>2</sup>. The behavior of the valence electrons give to the solids their crystalline structure and electric properties. For instance, the valence electrons in diamond and graphene form covalent  $\sigma$  bondings that are strongly oriented and localized, and the  $\pi$  bonds explain the special electrical behavior of graphene. This split of the electrons in two types lead us naturally to think of two basis to expand the electronic density: associated with the core electrons that are strongly localized we can think of atomic orbitals; and associated with the valence electrons, that are more or less localized we can think of plane waves.

<sup>1</sup>The same in the computational sense, i.e., the difference between the input/output densities have to be less than some convergence criterium, typically  $\leq 10^{-6}$

<sup>2</sup>In some special cases, some of the core electrons have to be considered as valence electrons, as in the case of bismuth (cite), where 10 electrons belonging to the 3d orbital are taken from the core and placed in the valence, this kind of electrons are called semicore.

If we think of a solid as a stable structure built by the approximation of isolated atoms (Figure 1.1), the overlap of the Coulomb potentials due to each atomic nucleus leads to two domains: the interstitial-valence one, where almost cancelation between the ionic forces (over the electrons) leads to a potential relatively small, almost constant, generating a nearly-free electron region; and the ionic-core region, where the electrons are strongly localized and bounded to the ions, experiencing a strong attractive potential. Thus, the valence electronic wavefunction has to be of 'plane wave' kind on the interstitial region and 'atomic orbital' kind on the core region. In the core region the valence electrons have a more oscillatory behavior than in the interstitial one, indicating high kinetic energy. As a consequence, inside the core region the valence wavefunctions have to have oscillations carefully chosen in order to have states orthogonalized to the electronic core states. It is the physical origin of the old rule: eigenstates of the same hamiltonian with different eigenvalues must be orthogonal [32]. These considerations, guided Herring in 1940 to introduce the concept of *ortogonalized plane wave* [33], that according to Zeman [34] "*has been of the most fruitful developments in solid state theory since the work of Bloch in the early 1930's*". This useful concept was the origin of the theory of the pseudopotential developed originally by Phillips and Kleinman in 1959 [35].

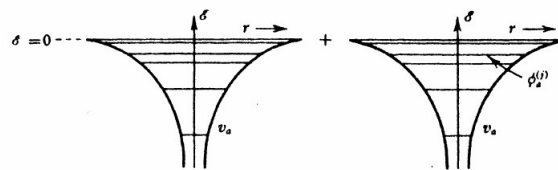


Fig. 54. Bound atomic orbitals of free atoms.

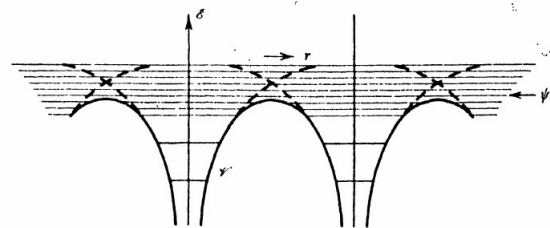


Fig. 55. Bloch states of crystal.

Figure 1.1: Solid built as approximation of isolated atoms. Source: [34]

The concept of pseudopotential has been successfully implemented in routine DFT calculations due to several reasons: in first place, the problem was simplified from the all electron problem to consider only the valence electrons under the influence of a 'pseudo-atom' made by the nucleus plus the core electrons. Secondly, in practice the pseudopotential is a data file minimizing computational costs. Thirdly, because we are interested only in the valence wavefunction in the interstitial region, the pseudopotential technique switches the oscillatory part in the core region by a smooth function that has the same behaviour starting from an appropriate cutoff radius.

Going back to the basis to expand the Kohn-Sham states, it is important to realize that the choice of plane waves or atomic orbitals to expand the eigenstates of KS has advantages and drawbacks: firstly, the wave plane basis is appropriated to describe a bulk material, because

the periodicity of the potential leads to a periodic electronic density that can be delineated with high resolution allowing a enough number of waves. Plane waves, also let transform the KS equations from differential to algebraic, that are easier to implement. As drawback, to deal with finite systems (monolayers, nanoribbons, molecules) the vacuum space between the periodic images have a high computational cost. The softwares Quantum Espresso [36] and VASP [37] use wave plane basis. Secondly, the atomic orbitals basis is localized and goes to zero to long distances (sparsity of the density matrix), as a result, it don't give additional computational cost dealing with vacuum space, so it is highly recommended to finite systems. One typical drawback is the appearing of fictitious forces due to the basis dependence on the atomic position. The SIESTA software [38] uses atomic orbital basis.

## 1.4 Exchange and correlation functional

The total energy of the system is a unique functional of the electronic density and can be expressed like:

$$E[n(\mathbf{r})] = T[n(\mathbf{r})] + V[n(\mathbf{r})] + U[n(\mathbf{r})] \equiv F[n(\mathbf{r})] + V[n(\mathbf{r})]. \quad (1.21)$$

Is is necessary to define the exchange-correlation energy in terms of Hartree and Hartree-Fock energy. Hartree equations already contain in the hamiltonian all the interactions, but these use as *ansatz* a wavefunction of distinguishable electrons (direct product of single electron wavefunctions). In addition, the Hartree-Fock approach takes into account the indistinguishability of identical particles, using as a trial wavefunction a Slater determinant, which is a wavefunction of a system of identical particles yet non-interacting. Hartree and Hartree-Fock equations are approximations to the complete problem where the wavefunction leaves to be a non-interacting one, due to the electronic correlation. To summarize, the Hartree problem isn't considering the electronic correlation nor the indistinguishability, and the Hartree-Fock approach isn't taking in count the electronic correlation. This regards allow us to define, in first place, the exchange energy  $E_x[n]$  as the difference in the energy expected value obtained between the Slater determinant  $|\Psi_{HF}\rangle$  and a direct product of single electronic wavefunctions  $|\Psi_H\rangle$ , isolating the exchange effect:

$$E_x[n] = \langle \Psi_{HF} | \hat{H} | \Psi_{HF} \rangle - \langle \Psi_H | \hat{H} | \Psi_H \rangle. \quad (1.22)$$

Next, we define the correlation energy as a difference in the energy expected value obtained between the true ground-state  $|\Psi\rangle$  and the one get with the Slater determinant  $|\Psi_{HF}\rangle$ , isolating the correlation effect:

$$E_c[n] = \langle \Psi | \hat{H} | \Psi \rangle - \langle \Psi_{HF} | \hat{H} | \Psi_{HF} \rangle. \quad (1.23)$$

We can restate the energy functional as:

$$E[n] = T[n] + U[n] + V[n] = T_s[n] + U_H[n] + E_{xc}[n] + V[n], \quad (1.24)$$

where,  $T_s[n]$  is the energy kinetic functional of a non-interacting electronic system (equation 1.14),  $U_H[n]$  is the Hartree energy, i.e., the electric classic energy between two electronic charge densities  $n(\mathbf{r})$  and  $n(\mathbf{r}')$ , given by:

$$U_H[n] = \frac{e^2}{2} \int \int \frac{n(\mathbf{r})n(\mathbf{r}')}{|\mathbf{r} - \mathbf{r}'|} d\mathbf{r} d\mathbf{r}', \quad (1.25)$$

and  $E_{xc}[n]$  is the exchange-correlation functional defined as:

$$E_{xc}[n] = T[n] - T_s[n] + U[n] - U_H[n]. \quad (1.26)$$

The exchange-correlation energy contains the difference between the kinetic energies with and without interaction, and the difference between the total interacting electronic energy and the Hartree one. Said otherwise, the effect of the interaction between the electrons is to introduce an additional energy term coming from the indistinguishability and from the correlation that modifies the total wavefunction. Handling with the exchange-correlation term is a subtle problem, and according to the spatial behaviour of the density it leads to different approximations, by example: the local density approximation (LDA), generalized-gradient approximation (GGA) and others [24] [39].

## Chapter 2

# Theory of elasticity

Matter is discontinuous, atomic positions are marked with by the high density atomic nuclei surrounded by an electronic quasi-continuous 'jelly', with a much lower density. As it is known, the valence electronic cloud behaves as a "spring media" joining the high density nuclei and being responsible for the electronic and mechanical properties of all materials. Looking at materials in this way, the first principles Density Functional Theory, appears as a well suited approach to describe a continuous of "spring media", taking into account, simultaneously, the continuous nature of the electronic jelly and the discrete nature of the ions.

### 2.1 Basics in theory of elasticity

Within the continuous media approximation [40–42], the deformation of a material is described by the *displacement vector*  $\mathbf{u}$  or in components  $u_i$ . It describes the displacement of a point of the body, from the initial position before the deformation  $x_i$  to a new position  $x'_i$ , as a result of an applied *stress*, defined as the force applied by unit area (usually measured in Pascals (Pa): Newtons per square meter - see section 2.3).

$$u_i = x'_i - x_i. \quad (2.1)$$

The  $\mathbf{u}$  vector is a function of the coordinates  $x_i$  before the deformation.

The differential squared distance between two points after the deformation  $dl'^2$ , in terms of the non deformed squared distance  $dl^2$  is:

$$dl'^2 = dl^2 + 2u_{ik}dx_i dx_k. \quad (2.2)$$

Where the tensor  $u_{ik}$  defined by:

$$u_{ik} = \frac{1}{2} \left( \frac{\partial u_i}{\partial x_k} + \frac{\partial u_k}{\partial x_i} + \frac{\partial u_l}{\partial x_k} \frac{\partial u_l}{\partial x_k} \right), \quad (2.3)$$

is called the *strain tensor*<sup>1</sup>. It is symmetrical, so it can be diagonalized in such a way that

---

<sup>1</sup>Those expressions use the sum convention: repeated index sum over all the values 1,2,3.

the mechanical response of a material to any applied stress can be expressed as compressions or extensions along the principal axes. As is usual in the elastic theory when the body is subjected to small deformations the second derivatives can be neglected <sup>2</sup>, so the strain tensor becomes:

$$u_{ik} = \frac{1}{2} \left( \frac{\partial u_i}{\partial x_k} + \frac{\partial u_k}{\partial x_i} \right) \quad (2.4)$$

In general, we have two types of strain: normal, when the deformation compresses (or expands) the material in the same direction of the stress; and shear, when the deformation tends to slide the material. Considering an one-dimensional normal strain and the displacement vector as a continuous variable of the position, the normal strain component is given by:

$$u_{xx} = \frac{\partial u_x}{\partial x}. \quad (2.5)$$

In the case of shear strain, we expect the displacement in the x direction to be proportional to the variation of the y coordinate in relation to x:

$$u_{xy} = \frac{1}{2} \left( \frac{\partial u_y}{\partial x} + \frac{\partial u_x}{\partial y} \right). \quad (2.6)$$

According with the Hooke law, experimental results shown that, to small deformations, the stress applied has a direct proportionality to the strain:

$$\sigma_{ij} = C_{ijkl} u_{kl}, \quad (2.7)$$

where  $\sigma_{ij}$  is the stress tensor with units of force per unit area, or energy per unit volume, meaning that the deformed body is storing elastic energy.  $C_{ijkl}$  are the elastic constants. There are, in principle,  $3^4=81$  elastic constants, however, this number can be strongly reduced by symmetry considerations. Considering the undeformed body as the equilibrium state where the forces experimented by each ion are zero, we have a quadratic expression to the energy stored by a deformed body, in terms of normal and shear deformations:

$$F = F_0 + \frac{1}{2} \lambda u_{ii}^2 + \mu u_{ik}^2, \quad (2.8)$$

where  $\lambda$  is called the Lamé's constant and  $\mu$  is the shear modulus. This statement is the tensor version of the familiar  $F = -kx$ , that expresses the force in the harmonic oscillator, and the energy expression is nothing more than the familiar  $E = -\frac{kX^2}{2}$ , expressing the equilibrium condition, characterizing zero internal forces, that excludes the linear term.

From any symmetric tensor three invariants can be defined [40,42], one of them being the sum of the diagonal elements:

$$u_{ii} = -\frac{p}{K}. \quad (2.9)$$

---

<sup>2</sup>It is worthy to note that it approximation requires the variations to be small, not the displacement vector itself.

The sum of the diagonal elements is proportional to the net change in the volume. As a consequence, it is proportional to the pressure  $p$ , with a minus sign because an increase in pressure implies a decrease in volume. The constant of proportionality is called the coefficient of hydrostatic compression or bulk moduli,  $B = \frac{1}{K}$ , that measures the relative variation of the volume of a material submitted to hydrostatic pressure, according to:

$$B = \frac{1}{K} = -\frac{1}{V} \left( \frac{\partial V}{\partial p} \right)_T. \quad (2.10)$$

In the case of isotropic materials it can be shown [40, 42] that the 81 elastic constants are reduced to only two independent elastic constants:  $\lambda$ , called the Lamé's constant, and  $\mu$  known as shear modulus. Because expansion on some direction combined with the mass conservation determine the contraction on both perpendicular directions, the volumetric and unidirectional elastic constants are all related:

$$E = \frac{9K\mu}{3K + \mu}, \nu = \frac{1}{2} \frac{3K - 2\mu}{3K + \mu}, \quad (2.11)$$

where  $E$  is the Young modulus that determines extension in one direction;  $\nu$  is known as Poisson's ratio, and measures the ratio between transverse compression to longitudinal extension. According to the continuum elastic theory, since  $K$  and  $\mu$  are always positive, the Poisson's ratio ranges between -1 (for  $K = 0$ , meaning an infinitely compressible solid) and  $\frac{1}{2}$  (for  $\mu = 0$ , meaning an incompressible solid). It is expected that, in the majority of materials, the poisson ratio is positive, meaning that to stretch the material in some direction causes contraction along the perpendicular direction coming from the mass conservation. However there are materials exhibiting anomalous behaviour, expanding in the perpendicular direction while being stretched, or contracting while being compressed. This class of materials is called auxetic. For example, in the silicates context, the  $\alpha$ -cristobalite polymorph of 3D silica exhibits a negative Poisson's ratio [43–45].

## 2.2 Information contained in stress-strain curves

Characterization of mechanical properties of materials is done by performing load experiments that lead to stress-strain curves. In such experiments a cylindrical sample is loaded axially. As it was mentioned in the previous section, the behaviour under small deformations is usually linear, characterized by the Young or uniaxial extension modulus:

$$\sigma_{xx} = E \left( \frac{l - l_0}{l_0} \right) = E\mu_{xx}; \quad (2.12)$$

where  $l_0$  is the equilibrium length,  $l$  is the deformed length, and  $E$  is as before, the Young modulus or extension coefficient. If we continue applying uniaxial stress, the material falls into the elastic non-linear region, where it is still able to recover its original form, but the relationship between stress and strain is not linear. Going further, eventually leads the material to the plastic region, where the deformation becomes permanent. The point at which the



nonelastic behaviour begins is called *yield point*. Brittle materials (like cast iron) do not show large plastic deformation before failure. On the other hand, aluminium, for example, expands in a wide interval, reducing substantially its cross sectional area before failure (see figure 2.1). Finally, the stretch breaks the material at a certain critical value of stress, characteristic of each material.

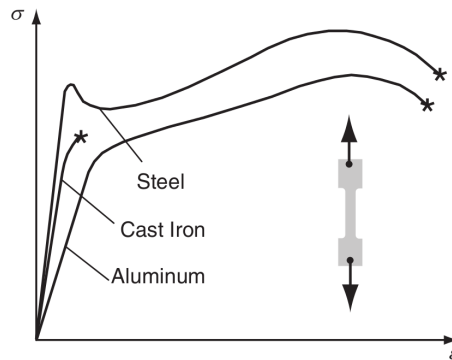


Figure 2.1: Typical uniaxial stress-strain curves for three structural metals. Source: [46]

Metal	Measured B
Li	11.5
Na	6.42
K	2.81
Rb	1.92
Cs	1.43
Cu	134.3
Ag	99.9
Al	76.0

Table 2.1: Bulk moduli in GPa for some typical metals. Source: [32].

In the 2D-materials case, it makes sense to consider not the elastic energy per volume unit, but the elastic energy stored per unit area. We then define the 2D Young modulus, in units of newtons per meter.

## 2.3 Units and orders of magnitude

It will be useful to do a brief revision of units. In the atomic orders of magnitude, the unit usually used for force is  $\frac{eV}{\text{\AA}}$ , and for stress is  $\frac{eV}{\text{\AA}^3}$ , meaning stored elastic energy per unit volume. To have an idea, the force between an electron and a proton in a hydrogen atom is  $\sim 82$  nanonewtons (nN) or  $51.5 \frac{eV}{\text{\AA}}$ . A common criterion to consider that a supercell is relaxed is that the force on any atom is less than  $0.01 \frac{eV}{\text{\AA}}$  ( $\sim 16$  piconewtons). This residual force is of the order of 0.02% of the force between the electron and proton in the hydrogen atom. Comparing with orders of magnitude of forces in atomic force microscopy (AFM), where between the tip and the sample, there appears attractive forces, in the non-contact mode (coming from

Van der Waals forces), or strongly repulsive in the contact-mode (coming from interatomic forces). In the non-contact mode, forces are in the  $\sim 10^{-12}$  N (piconewton) range, and in the contact mode in the  $\sim 10^{-8}$ - $10^{-6}$  N, i.e.,  $10$ - $10^3$  nN. Thus, the force between a proton and an electron in a hydrogen atom is, as expected, contained in the contact-AFM-mode range, and the residual forces in the geometry relaxing criterion are in the non-contact-mode range [47]. Also useful is the conversion factors from  $\frac{eV}{\text{\AA}^3}$  to GPa, or to  $\frac{N}{m}$  that is appropriated for 2D materials:

$$\sigma(\text{GPa}) = \sigma\left(\frac{eV}{\text{\AA}^3}\right) 160.22 \quad (2.13)$$

and

$$\sigma\left(\frac{N}{m}\right) = \sigma\left(\frac{eV}{\text{\AA}^3}\right) c(\text{\AA}) 16.022 \quad (2.14)$$

where  $c(\text{\AA})$  is the length of the supercell in the direction normal to the 2D-material layer in our calculations, and the 160.22 and 16.022 factors, come from the energy in joules contained in 1 eV, that is numerically the electron charge:  $1.6022 \times 10^{-19}$ . The relaxed pressure in a typical relaxed supercell will be in the range of  $\sim 0.01$  kbar or 9.87 atm. 1 GPa is equal to 9870 atm. Typical values of bulk modulus of metals are in the range of 1-10 GPa (see Table 2.1).

# Chapter 3

## Theory of defects

### 3.1 General theory of point defects

The semiconductor technology underwent a broad development driven by challenges during the World War II [48–52], for example for use in microwave detectors and radar technology. Initial research was focused on the growth of high-quality crystals and on manipulating the conductivity, while adding impurities in a non-homogeneous way, giving origin to semiconductor junctions (n-p, n-p-n, p-n-p), that are the bricks of the modern silicon technology. The huge semiconductor industry and multiple applications rest on the extensive range of resistivities that can be reached in semiconductors at room temperature, through impurity doping, as we can see in Table 3.1.

Table 3.1: Orders of magnitude electrical resistivity to different materials. Source: [53].

Type of material	Resistivity ( $\Omega\text{-m}$ )	Example
Metal	$10^{-8}$	cooper
Semimetal	$10^{-5}$	bismuth
Semiconductor	$10^{-4}$ to $10^{-11}$	silicon
Insulator	$10^{16}$ to $10^{24}$	diamond

Physical properties of semiconductors are deeply affected by defect engineering, in such a way that semiconductor development would have been irrelevant, if were not by a wide range of properties associated with the introduction of defects. In general terms, lattice defects can be classified in terms of the dimensionality of the disturbance to the crystal matrix, in three main categories: in first place, zero-dimensional point defects, i.e., vacancies, impurities and complexes of this defects <sup>1</sup>. In second place, one-dimensional line defects, as in the case of dislocations. Finally, two-dimensional planar defects, as in the grain boundaries and stacking faults. In the case of point defects we have: vacancy, when a atom is missing; interstitial, when a native atomic species occupies a place between the crystalline regular positions. A third class of point defect is the impurity, when a different atomic species replaces one of

<sup>1</sup>An interesting example is the  $NV^{-1}$  nitrogen-vacancy center in diamond, of interest in quantum information science [54]

the host atoms. In the case of SiO<sub>2</sub>, by example, a silicon atom can be replaced by a group III specie, such as boron (B) or aluminium (Al), or by a group V specie, such as nitrogen (N) or phosphorus (P). When comparing a vacancy with an impurity, it would be natural to expect that the impurity represents a lesser perturbation to the host crystal, because a complete atomic absence will affect the atomic crystal neighborhood more than an atomic specie that is contributing essentially with one electron or one hole to the solid.

Impurities can contribute to the host semiconductor with electrons (donor impurity) or holes (acceptor impurity), according to the valence of the dopant specie, and the position of the defect levels in the semiconductor gap. As a simple example consider a phosphorus (P) atom in a matrix of crystalline silicon. Its valence orbital configuration is  $s^2p^3$ . Eight electrons fill the four  $sp^3$  hybrid orbitals surrounding the phosphorus ion. Four electrons come from each silicon atom around and 4 electrons from the phosphorus impurity, having 2 electrons with antiparallel spin, in each covalent bond. In principle, the guest atom is pentavalent, so it contributes with 4 electrons, just as a Si host atom, leading one free electron that acts as a negative charged carrier. This electron remains weakly bounded to the dopant ion, having a very small binding energy (typically of tents of meV, little in comparison with a electron in the ground state of a hydrogen atom: -13.6 eV) building a hydrogen-like atom, with a smaller effective mass and a higer dielectric constant. Physically what is happening is that the effect of the solid (silicon matrix) on the guest atom is to create a polarization around the P atom, diminishing the interaction between the screened ion and the "free" electron. One of the effects of the solid polarization around the P atom is that the wave functions of the hydrogen-like atom are more extended, however, yet localized. So an impurity can originates a fascinant class of 'extended hydrogen-like' atoms. These shallow states are called effective mass states, and are described by the effective mass theory (EMT) valid only for shallow states, and it will be described in section 3.2.1.

## 3.2 States induced by point defects

The physical phenomena behind the electronic structure theory is the multiple quantum scattering experienced by valence electrons interacting with the ions of the solid. In this complex process the wave behaviour of the electrons leads to spatial regions of interference destructive and constructive, caused by the ionic periodic potential and the electronic repulsion. These regions are able to confine the electrons in places where the density is supported, as happens in the chemical bonds that give origin to the crystalline structure of the material and to the conduction electrons, in metals, that flows through the solid. Electrons in a solid are described by Bloch states, that describe the free movement of the electrons in metals. The periodic potential effect is incorporated in the new 'free' Bloch states. In this scenario a point defect behaves as a scattering center for the 'free' Bloch states, just as an atom can scatter a free electron. A point defect can create new bound states and also new scattering states such as ressonances and anti-ressonances. The mathematical background of quantum scattering is the complex analysis and the Sturm-Liouville theory of differential equations.

In spite of the complexity of the quantum multiple scattering physics, the quantum mechanics of the electrons in periodic lattices has been addressed at the beginning of the twenty century by Felix Bloch a swiss-american physicist [55]. Under the Ph.D. advisory of Werner Heisenberg, he was oriented by one main question: why conduction electrons in metals can be treated as an ideal gas?, how can them flow almost freely through the solid, despite of the ion scattering process? As the Bloch himself writes in his memorial notes [56]: *“When I started to think about it, I felt that the main problem was to explain how the electrons could sneak by all the ions in a metal to avoid a mean free path of the order of atomic distances. Such a distance was much too short to explain the observed resistances which even demanded that the mean free path become longer and longer with decreasing temperature. But Heitler and London had already shown how electrons could jump between two atoms in a molecule to form a covalent bond, and the main difference between a molecule and a crystal was only that there were many more atoms in a periodic arrangement. To make my life easy, I began by considering wave functions in a one- dimensional periodic potential. By straight Fourier analysis, I found to my delight that the wave differed from a plane wave of free electron only by a periodic modulation. This was so simple that I didn’t think it could be much of a discovery, but when I showed it to Heisenberg he said right away, “That’s it.” Well, that wasn’t quite it yet, and my calculations were only completed in the summer when I wrote my thesis on “The Quantum Mechanics of Electrons in Crystal Lattices”*

The Bloch’s answer was simple, just using straight Fourier analysis, he found that electrons in a periodic solid act as a plane wave enveloped by a periodic modulation. In the perfect crystal the wavefunctions are completely deslocalized, extending over all the crystal, as expected for Bloch functions. Once, the perfect periodicity of the crystal, is broken, by an impurity for instance, localized states are allowed. The presence of the point defect in the crystal region where the electronic density departs from the periodic scheme inherited from the Bloch theorem’s.

Going back to periodic point defects, we have essentially a similar result for the shallow gap states, for which the electron is weakly bonded to the defect, and behaves as a Bloch state enveloped by a weakly decaying exponential envelope. In general, we have to solve the Schrödinger equation that describes the states in the crystal with the impurity:

$$\hat{H}|\Phi_n\rangle = E_n|\Phi_n\rangle, \quad (3.1)$$

where the hamiltonian is composed by the electronic kinetic energy, and a one-electron potential that includes the perturbation imposed by the impurity:

$$\hat{H} = \hat{H}^0 + \hat{V}_{inp}, \quad (3.2)$$

The pristine part of the crystal is contained in  $\hat{H}^0$ . Just as it happens in the hydrogen atom, this equation has two types of solutions: states whose energy fall into the allowed energy bands - states of continuum, and states where the energy fall into the band gap - bound states. In general, due to the localized nature of the impurity-induced states, these appear

in the band structure, as non-dispersive states. For states inside the gap, Pantelides [57] distinguishes two cases: impurity potentials with a finite range, and Coulomb-kind impurity disturbances with a  $\frac{1}{r}$  nature. In the first case, the resulting states have wavefunctions with an exponential decay, far from the defect, giving rise to strongly localized states. Usually their energies are deep in the gap, distant to the bands edges more than 0.1 eV. In the second case, we have a hydrogenic-like spectrum and also hydrogenic-like bound wavefunctions, of two types: if the potential is attractive we have infinite states near the conduction band minimum (CBM); and if repulsive, we have infinite states near the valence band maximum (VBM). In both cases, the wavefunctions in the  $n \rightarrow \infty$  limit merge in a continuous way with the respective band edge. Now, in the case of impurity states within the region of the bands of the perfect crystal, we have scattering solutions that approach asymptotically the non-perturbed solutions. This solutions can give rise to resonances. If we have an attractive potential in combination with the centrifugal barrier, quasi-bound states may emerge [58,59]. In the resonance condition, the incident electrons coming from the conduction or valence band have a large probability of becoming temporarily trapped within the impurity state, tunneling through the centrifugal barrier. The resonance condition is verified in the density of states as a "hump" or "peak" that appears in comparison with the density of states from the crystal without the impurity. It is also possible to have anti-resonances, that manifests as a "reduction peak" in the density of states coming from certain region in the real space that avoids electrons. Just to have a intuitive sense of this phenomena, it is worth to recognize that in the dynamics of the planets, governed by an inverse square law of movement, a resonance is the temporary trapping of an object (as a comet for example) orbiting in some region of space; and an anti-resonance is the forbidden occupation of a certain space region.

Concerning the bound states, deep within the gap, they play a completely different role: while shallow states control the conductivity, deep states act as carrier trapping centers. Deep states work as recombination centers, controlling the lifetime of carriers, that can be useful in photocells for instance.

### 3.2.1 Effective Mass Theory: EMT states

This approximation is made following the Madelung's approach [60]. Semiconductor conduction properties are driven by shallow defects. In this kind of electronic states the potential coming from the defect can be considered as a weak perturbation in comparison with the periodic potential from the crystal. This perturbing potential gives origin to hydrogenic-like atoms displaying orbits with large radii. Taking into account that the electron travels through several unit cells, the screening effect of the crystal, over the potential originated from the defect, can be considered introducing a dielectric constant  $\epsilon$  in the perturbing potential:

$$U(r) = -\frac{e^2}{4\pi\epsilon\epsilon_0 r}. \quad (3.3)$$

The wave function describing an electron in presence of the potential can be built as a wave packet of Bloch functions  $\psi_n(\mathbf{k}, \mathbf{r})$ :

$$\psi(\mathbf{r}) = \sum_{n,\mathbf{k}} c_n(\mathbf{k},\mathbf{r})\psi_n(\mathbf{k},\mathbf{r}). \quad (3.4)$$

Inserting in the Schrödinger equation we have:

$$\sum_{n,\mathbf{k}} c_n(\mathbf{k})(E_n(-i\nabla) + U)\psi_n(\mathbf{k},\mathbf{r}) = E\psi. \quad (3.5)$$

Note that in this equation the periodic crystal potential no longer appears, being 'absorbed' by the  $-i\nabla$  operator (see Madelung [60] section 2.2.9). If the energy of the bounded electron is small in comparison with the band-gap energy, the energy denominators, in a typical perturbed wavefunction coming from valence band wavefunctions are negligible. So only Bloch states coming from the conduction band contribute. In case of a strong bounded electron, Bloch states from all the Brillouin zone have to be considered, and we depart from the shallow defect zone to the deep defect one, where the perturbing approach fails and Green function methods have to be applied [57, 61]. Within this approximation the band index disappears:

$$[E(-i\nabla) + U]\psi = E\psi \quad (3.6)$$

Because to the extended spatial character of the wavefunction of a shallow state, we have to have a very narrow character in the reciprocal space as is expected according to the uncertainty relation between the momentum and the position for a quantum mechanical particle. Taking vantage of this observation, our wave packet coming from a very narrow conduction band states, and considering the minimum of the conduction band as the zero energy, we can approach the whole packet as being essentially builded by the zero  $\mathbf{k} = 0$  vector as the greatest contribution, leaving to:

$$\psi = \left[ \sum_{\mathbf{k}} c(\mathbf{k})e^{i\mathbf{k}\cdot\mathbf{r}} \right] \psi(0,\mathbf{r}) \equiv F(\mathbf{r})\psi(0,\mathbf{r}), \quad (3.7)$$

and, the Schrödinger equation finally becomes a equation to the 'envelope function'  $F(r)$ :

$$[E(-i\nabla) + U]F(r) = EF(r). \quad (3.8)$$

This equation is just a hydrogenic equation and has as solution to the ground state the wavefunction:

$$F(r) = \frac{1}{\sqrt{\pi(a_0^*)^3}} e^{-\frac{r}{a_0^*}}, \quad (3.9)$$

with a effective Bohr radius given by:

$$a_0^* = \frac{4\pi\epsilon_0\hbar^2}{me^2} \frac{m}{m^*} \epsilon \quad (3.10)$$

and hydrogenic energies given by:

$$E = E_c - 13.6 \frac{m^*}{m\epsilon^2} \frac{1}{n^2} \quad (3.11)$$

Typically, while an hydrogen's electron in the ground state has a binding energy of -13.6 eV and a Bohr radius extension of 0.53 Å, a mass effective electron has a binding energy of -13.6 meV and a quite large radius 53Å, one hundred times larger. This qualitative approach to study impurity electronic levels is valid for states shallow enough that their wave functions are almost electron Bloch states, where the potential due to the impurity can be considered as a weak perturbation. Instead of we could initially think, despite of the orbit of the electron (that extends over hundreds of crystal cells) being larger, the hydrogen-like schrödinger equation describes more accurately the state, because in this case the electron is far away of the region where the impurity can be more perceived [62]. Completely analogous considerations, as in the donors can be made having acceptors, in this case related to the wavefunction and energies of the hole loosely bound to the impurity atom. If we have boron (B) in the site of silicon, for instance, it configures in principle an acceptor impurity, with a defect level placed inside the gap, near to the top of the valence band. Because boron belongs to the group III, we can expect a deficiency of one electron, i.e., a hole weakly bonded to the impurity ion.

### 3.2.2 Ressonant scattering - states within the bands

States within the energy bands, i.e., resonant (or anti-resonant) scattering, can be described in terms of Green functions including the impurity potential, defined by analogy with the Green function for the pristine crystal [57], as

$$G(E) = \frac{1}{E - H}, \quad (3.12)$$

Where  $H$  is the hamiltonian operator containing the perturbing potential. The density of states, i.e., the number of states per unit energy lying in the energy range between  $E$  and  $E + dE$ , is related with the Green function as:

$$D(E) = \frac{1}{\pi} \text{Im} \frac{d}{dE} \ln \det G(E), \quad (3.13)$$

$E$  is considered as a complex variable. The introduction of the impurity causes a change in the density of states, with respect to the cell without the point defect:

$$D(E) = D^0(E) + \Delta D(E), \quad (3.14)$$

Where  $\Delta D(E)$  is given by:

$$\Delta D(E) = \frac{1}{\pi} \text{Im} \frac{d}{dE} \ln \det (1 - G^0 U), \quad (3.15)$$

There are conservation of the number of states (Levinson's theorem [57]) derived by analytical properties of the operator  $1 - G^0 U$  (cite):



$$\int_{-\infty}^{\infty} \Delta D(E) dE = 0 \quad (3.16)$$

So when defect states appear into the gap, they come from missing states in the bands, or in other words, the emergence of defect states in the gap have to be necessarily balanced with the happening of antiressonances within the bands. The number of bound states appearing into the gap are equal to the states missing from the bands:

$$\int_{bands} \Delta D(E) dE = -N_b \quad (3.17)$$

The electrical behavior of a doped semiconductor, n or p type, is driven by states near to the band's edge described by the mass effective theory. The degree of deslocalization of this hydrogen-like state stimulates the possibility to transit between the shallow defect state and the edge of the band (the minimum of the conduction band to electrons, or the maximum of the valence band to holes).

Just to mention, it would be interesting to think about all the spectrum of the solutions and in the transitions between them. Ta a point defect we have three types of solutions: scattering states - rersonances in the bands, and bounded gap states: shallow and deep. The transitions between the solutions in this regions are called studies of analytical properties of the solutions, this approach have been worked, for example, by Walter Kohn [63] and D. Vanderbilt [64], studying what happens with the Bloch functions and the energies if we extend the dominium of the function from real wave vector values to complex values (analytic continuation). Intuitively, we can expect, that sometimes we have as  $\mathbf{k}$  an pure imaginary number, that reduces the oscillatory exponential function to a simple exponential decaying. Rougly speaking, real  $\mathbf{k}$  values lead to rersonant (or antiressonant) scattering states; complex  $\mathbf{k}$  values leads to shallow states, where the rate of the decaying is governed by the imaginary part; and pure imaginary  $\mathbf{k}$  vectors, leads to strongly localized states driven by a fast exponential law of decay as is it expected to deep states.

A few words about the relationship between symmetry and point defects. The symmetry of the defect is deeply related with the defect's states. The main ideia is that when we have broken symmetries in the crystal lattice, the states initially degenerated may unfold appearing with different energy and symmetry, stablishing the number of electrons that can be located in them. In covalently bounded solids, as is the case for group IV semiconductors, and c-BN and also our 2D silica, are based in a tetrahedral structure. That defect states come from hibridation of s, px,py and pz orbitals in a four-dimensional subspace. Initially they are degenerated, but in the case of a single vacancy or a substitutional impurity occurring in the tetrahedra center, the tetrahedral symmetry Td is broken, so the four-dimensional subspace generated by the sp3 orbitals becomes reductible in two irreductible representations: A1 ant T2. The defect levels are splitted in: one single level of A1 symmetry (s-like) and a threefold degenerate level with T2 symmetry (p-like) [65] [66].

### 3.3 Theory of charged defects

One of the main results of the existence of localized states within the gap is that the impurity can exist as an ionized ion in various charge states. When an impurity is inserted in a host crystal, and a mass effective state occurs, we have as starting point a neutral defect: the charge of the localized state is neutralized by the charge of the delocalized electrons coming from the bands. A neutral defect isn't yet a doped semiconductor, but if (suppose a state near to the conduction band) an electron occupying the impurity state, jump to the conduction band, we have as a result an empty localized state charged positively, because the lost of a negative charge. In the same way, consider a impurity state near to the valence band, in this case an electron jump from the valence band to the defect state filling a localized state initially empty, so the localized defect state is now charged negatively. It observation pointed by Pantelides [57] allows to define clearly charged states in semiconductors: "positively charged states are defined as donor states, and negatively charged states are defined as acceptor states". Somehow, charged states of an impurity ion are more like excited states, where the ground state are the neutral impurity. The neutral nature of the matter, will be considered deeply in the Pantelides fundamental approach (section 3.4), within the framework of the first principles simulation. In short, this approach take in account that a charged defect is created transferring electrons from (or to) the bands to (or from) the defect state without the introduction of fictitious external charges, making *ad hoc* corrections unnecessary. A key point to the understanding of this problem is the partition of the system complete in two subsystems: the point defect, considered as a little subsystem with localized wavefunctions, and the rest of the solid, considered as a bigger subsystem with delocalized wavefunctions.

Eventually to a defect state can be energetically favorable having charge states different from neutral. This possibility open new complexities and challenges to be solved by the metodological approaches used. In the framework of Kohn-Sham DFT, the approach to study this problem is to construct supercells big enough to isolate the defect and avoid interaction between the periodical images. This scheme works fine to neutral defects and allow to obtain formation energies without ambiguity, taking in count the computational cost increased with the supercell size. But in the charged defects case, this methodology introduce spurious Coulomb interactions between the periodic defect images, than can't be avoided increasing the supercell size. This problem divide our presentation in two main approaches: firstly, many literature papers and efforts to obtain the correct formation energy, substracting from the total energy the spurious electrostatic Coulomb energy, called *ad hoc* method. In a second place, Pantelides et. al. [23, 67] present a deeply theoretical revision about this subject, leading to a surprissing and simple statement: the *ad hoc* approach is based in a wrong energy formation expression and in violation of the principle of charge neutrality, because the charged defect is formed by charge exchange between the defect states and the solid bands, without external charges, so keeping the charge neutrality at the supercell. This last procedure is more convincing and consistent, so we apply this constrained DFT to study charged defects in silica 2D.

Just to have a main idea about the way to deal with this problem, it is necessary understand the path taken until here. This part is a resume of O'Hara - Pantelides considerations exposed in [67]. Neutral defects can be dealt using different size supercells until having convergence in the energy without any ambiguity. But, in the case of charged defects the long range of Coulomb interactions lead to a divergence in the energy. A way to facing with it, is to use the jellium approximation, dealing with the ions as a *continuum* of positive charge to neutralize the system, setting  $V(G=0)=0$ . This method eliminates the divergence, but not remove the long range Coulomb interactions between the periodic images. Leslie and Gillian [68] shown that formation energies not converge with the supercell size, being mandatory to extrapolate the energies to the limit of infinite supercell. This finite size scaling method uses the finite supercell energies to extrapolate the value to  $L$  infinite using some hypothetical scaling expression [69] [70], as can see in figure 3.1.

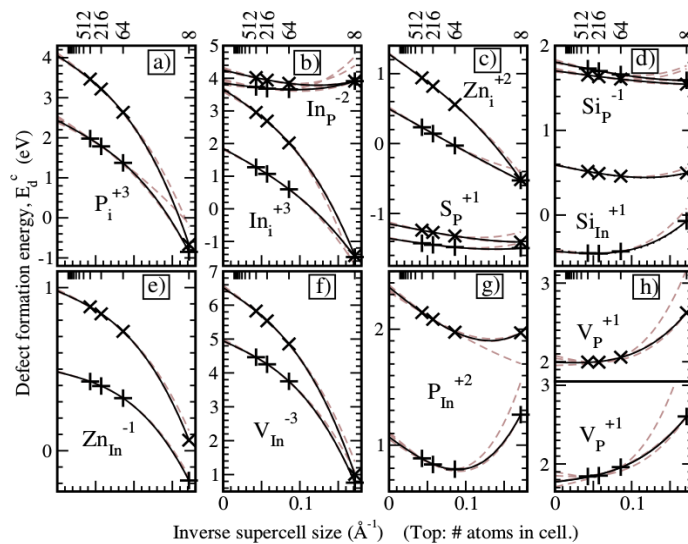


Figure 3.1: Scaling of unrelaxed (x) and relaxed (+) formation energies. Curves are fits to a multipolar scaling with  $n=3$ , similar to equation 3.18. The main idea is to fit the formation energy, from different supercell sizes (8, 64, 216, 512 atoms), in order to find the extrapolated infinite supercell limit. It is the best value to the formation energy. Figure from [69].

Later more sophisticated ways to correct the energies were developed, deserve special attention the Makov-Payne [71] and Lany-Zunger [72] schemes. Makov-Payne propose a multipolar correction that relates the energy not corrected  $E_T(L)$  with the right energy  $E_T(L \rightarrow \infty)$ :

$$E_T(L) = E_T(L \rightarrow \infty) - \frac{\alpha q^2}{2\epsilon L} - \frac{2\pi q Q}{3\epsilon L^3} + O[L^{-5}] \quad (3.18)$$

where  $q$  is the defect charge,  $Q$  is the quadrupole moment,  $\epsilon$  is the dielectric constant relative to the medium where charges are inserted,  $\alpha$  is the Madelung constant and  $L$  is the supercell size. This expression is valid only to 3D materials. Lany and Zunger [72] shown that the Makov-Payne correction term that scales as  $\frac{1}{L}$  remove long range interactions if other finite size effects are eliminated.

Transition to 2D materials lead to additional complexities, by example, in using the jell-

lium approximation appears new spurious interactions between the defect charge and the positive jellium filling the vacuum in the  $z$  direction, leading to linear divergence in the formation energies with the supercell size [73], as can see in the figure 3.2.

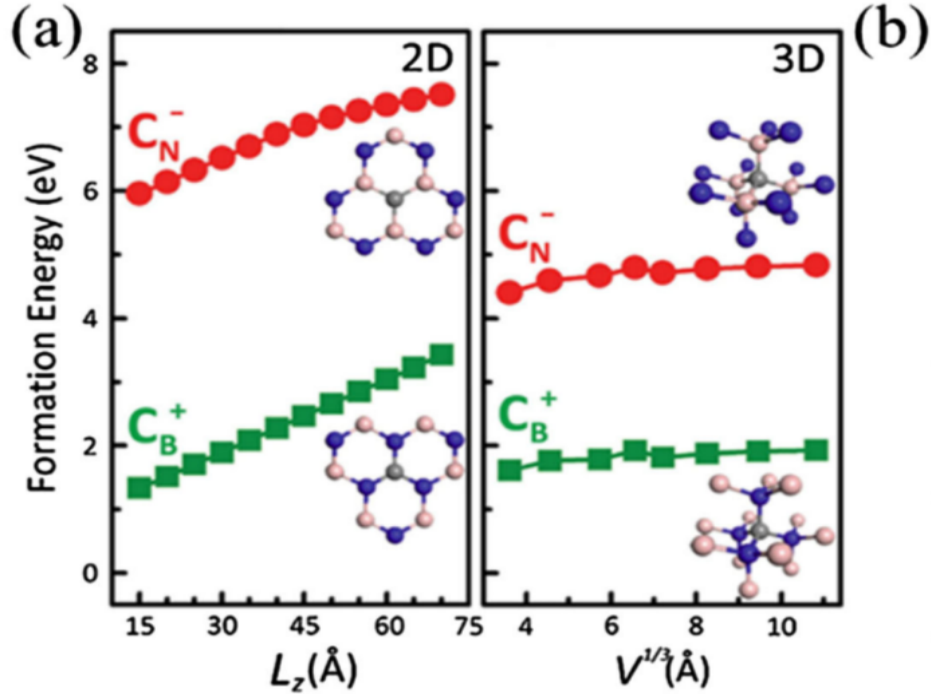


Figure 3.2: Calculated formation energy of charged  $C_N^-$  and  $C_B^+$  in 2D BN and 3D BN. To 2D BN the formation energy diverges. Figure from [73].

However, more analytical expressions to correct the energy in the case of 2D systems were presented: Wang et al [74] developed an efficient expression to obtain the ionization energy to a monolayer as a function of supercell side  $S$  and the vacuum size  $L_z$ , which asymptotic form is:

$$IE(S, L_z) = IE_0 + \frac{\alpha}{\sqrt{S}} + \frac{\beta}{S} L_z; \quad (3.19)$$

where  $IE_0$  is the ionization energy (i.e., the energy required to free electrons or holes from the dopants),  $\alpha$  is a defect specific madelung constant,  $\beta = \frac{q^2}{24\epsilon_0}$  is a constant that accompanies the 2D divergent term, and  $L_z$  is the size of the vacuum of the 2D supercell. After, the same authors generalize the expression to 2D systems with supercell side and arbitrary thickness  $d_0$  [75]:

$$E_{total} = \frac{q^2}{24\gamma L_x^2 \epsilon_0 \sin\theta} [(L_z - 4d_0) - 2d_0(1 - \frac{1}{\epsilon_\perp})] + \frac{q^2 d_0^3}{3\gamma L_x^2 \epsilon_0 \sin\theta} (\frac{1}{\epsilon_\perp} - 1) \frac{1}{L_z^2} + \frac{q^2 d_0^2}{4\gamma L_x^2 \epsilon_0 \sin\theta} (2 - \frac{4}{3\epsilon_\perp}) \frac{1}{L_z} \quad (3.20)$$

Constants are explained carefully at the reference [75]. After this brief 'state of the art' in relation with *ad hoc* correction methods, we are going to consider the more deeply analysis proposed by Pantelides.

### 3.4 Fundamental approach: Wu, Zhang and Pantelides (WZP)

Y. Wu, X. Zhang and S. Pantelides [23] [67] shown that: first, the expression commonly accepted to calculate formation energy of defects is more a ansatz or hipotese, but is not derived from fundamental principles. This expression, uses Fermi level as reference to the electrons energy, assumes that in fact electrons are removed from or added to the crystal, creating defects truly charged, and leading to spurious long range Coulomb interactions between the defect's periodic images. This interactions are cause of the cited divergences. Second, physicaly speaking, neutral defects become charged defects while electrons are exchanged between the defect states and the energy bands of the solid, so charged defects are charged in the sense them are ionized states keeping charge neutrality over the supercell. Third, schemes with truly charged defects violate a key statistical mechanics principle: the Fermi energy is determined by charge neutrality (the sum of electron charges in CB plus holes in the valence band plus charge in the defect levels must be zero (equation (6) from [67]):

$$p - n + \sum_q qC^q + q' C_{dop}^{q'} = 0, \quad (3.21)$$

where the neutral crystal carries: concentration  $p$  of holes, concentration  $n$  of electrons, concentration  $C^q$  of the different charge states  $q$  of a defect, and concentration  $C_{dop}^{q'}$  of ionized dopants carrying charge  $q'$ . In practical terms, the methodology proposed by Pantelides et. al. uses the usual selfconsistent electronic density convergence, as DFT do, but *constraining* the electronic population in the defect levels to obtain the charge state deserved. In the self-consistent relaxing process the electronic states are mixed enabling the charge neutralization between electrons in the bands and electrons at the defect states. Just to have a single clear example let's consider the defect states to phosphorus P substituing Si in the 2D SiO<sub>2</sub>. Finding the electronic density that minimizes the energy of the system, we calculate the bands structure (in a non polarized calculation) and find that the neutral defect state is a single semi-filled state just at the Fermi energy (see figure 3.3a).

This neutral defect state can change only to 2 charge states:  $q=+1$ , coming from the transference of one electron from the defect state to the conduction band minimum, leading the defect state empty of electrons and charged positively with charge= $+1$  (see figure 3.3b); and  $q=-1$ , coming from the transference of one electron from the valence band maximum to the only one available state in the neutral defect, leading the defect state filled and charged negatively with charge= $-1$  (see figure 3.3c). More charge states are not available, because we have just one defect state that admits only two electrons, according to Pauli's exclusion principle. In this first principles method we have two novelties, that were impossible in the old scheme where arbitrary number of charges can be added or removed from the crystal violating charge neutrality: in first place, given a point defect, we have charge states not allowed because of the number of defect states and the available electronic states. In second place, having more defect states in the gap, and more available states, we can have charge-degenerate states, i.e., identical value of charge builded with different electronic level populations.

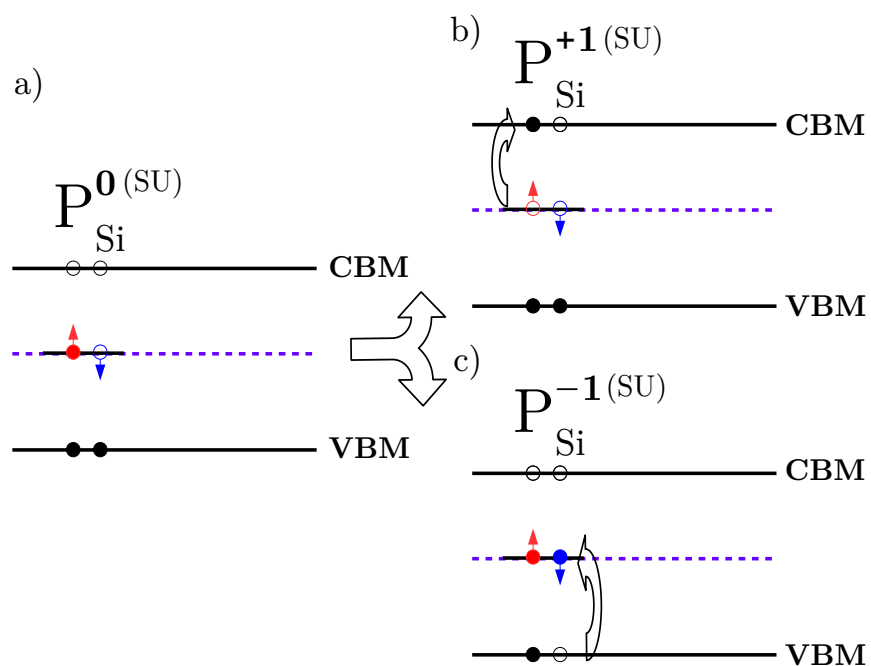


Figure 3.3: Scheme of energy levels of substitutional phosphorus in a Spin Unpolarized (SU) calculation. (a) Neutral defect. (b) Positively charged defect state, builded transferring a electron from the localized defect state to the conduction band minumim (CBM). (c) Negatively charged defect state, builded transferring a electron from the conduction band maximum (CBM) to the defect state.

# **Part II**

## **Results**

# Chapter 4

## Native defects

### Introduction

We begin to reviewing shortly main 3D silica electronic features as matter of reference in silica compounds and to do qualitative comparisons between 2D and 3D scenarios. The 3D polymorphs of silicate based compounds, range from several crystalline quartz phases (by example  $\alpha$  and  $\beta$  quartz) to amorphous phases such as, opal and glass. They have been extensively studied in the literature [76–84]. Between native defects the oxygen vacancy in 3D-SiO<sub>2</sub> is the main defect and is also responsible by deterioration of SiO<sub>2</sub> based electronic devices [85, 86]. Electron paramagnetic resonance (EPR) is a powerful technique that relies in the existence of unpaired electrons that absorb energy from a microwave field of radiation, signaling the identity of some point defect. In particular the most recurrent O-vacancy defect in quartz is the so called  $E'$  EPR center, consisting in an unpaired electron ( $S=1/2$ ). Also an  $E''$  center with two unpaired electrons in a triplet ( $S=1$ ) state has also been reported. [79].

In amorphous 3D-SiO<sub>2</sub> (a-SiO<sub>2</sub>), an  $E_{\delta}$  defect shows a very similar EPR profile as the  $E'$  center. Both  $E'$  and  $E_{\delta}$  have been assigned to the positively charged O-vacancy, based on theoretical *ab initio* calculations. [86] A more recent first principles study [87, 88] suggests that Si<sub>2</sub> dimers could be responsible for an unidentified paramagnetic center in vitreous 3D-SiO<sub>2</sub> (v-3D-SiO<sub>2</sub>). By examining nondimer configurations in positively-charged states, these authors consider puckered, unpuckered, doubly puckered, and forward-oriented configurations and find that the calculated EPR parameters of the puckered and unpuckered configurations support the assignment of an  $E'_{\delta}$  center in v-3D-SiO<sub>2</sub> to an unpaired spin localized at a three-fold coordinated silicon dangling bond. Moreover, the forward-oriented configurations are suggested as the assignment of an  $E'_{\alpha}$  center in v-3d-SiO<sub>2</sub>.

A feature of oxygen vacancies in the 3D polymorphs of SiO<sub>2</sub> that deserves mention, in the context of the present work, is the bistability of this defect in  $\alpha$ -quartz: in the neutral state, the O vacancy is stable in a dimer configuration, where a Si-Si bond is formed between the two Si dangling bonds that appear due to the removal of the O atom, while in the positively-charged state the defect assumes the so-called puckered configuration, where one of the Si atoms relaxes across the plane of its other three oxygen nearest neighbors and bonds with



another O-atom in the 3D network, to restore its fourfold coordination. [79, 80, 86].

The 3D polymorphs of SiO<sub>2</sub> are prone to carrier trapping and polaron formation. Intrinsic (involving polaron formation) and extrinsic (involving Ge or Li impurities) electron-trapping phenomena have been investigated using *ab initio* methods in  $\alpha$ -quartz and amorphous SiO<sub>2</sub>. [89, 90] In the case of 2D crystals, an issue that requires attention in the context of defect states is the influence of quantum confinement and enhanced Coulombic effects on the character of the wavefunction of the electronic states introduced in the fundamental band gap (and possibly strongly-localized resonances and antiresonances in the valence and conduction bands) by native defect and impurities. Regarding the issue of enhanced Coulombic effects, it is well known that, often, exciton binding energies in lower dimensional systems are one to two orders of magnitude larger than in 3D crystals. [16, 17].

## 4.1 Methodology

In our *ab initio* calculations, we have employed DFT in the Kohn-Sham framework, as implemented in the SIESTA software [38]. In order to model the structural and electronic properties of the pristine 2D-SiO<sub>2</sub> bilayer, a 12-atom primitive cell was used, with tight convergence parameters to obtain well converged structural properties, band structure, and density of states: a mesh cutoff of 800 Ry, with a 128x128x1 Monkhorst-Pack (MP) grid [91], and a gaussian smearing of 0.01 eV to draw curves for the density of states (DOS) and orbital-projected DOS (PDOS). For the structural relaxation of internal parameters, a tolerance on the residual forces of  $\leq 0.001$  eV/Å was imposed. All calculations in this work were performed using the experimental lattice constant of 5.42 Å, obtained by LEED, STM, and AFM measurements on ordered films of 2D-SiO<sub>2</sub> grown on Ru(0001) substrates [6, 7].

For the calculations of the properties of native defects, very good convergence with respect to supercell size was obtained with 192-atom supercells, except for the case of the external-layer oxygen vacancy, that required a 432-atom supercell in order to avoid spurious overlap between the defect states and their periodic images. For the self-consistency of the electronic charge density and the convergence of structural parameters, a 2x2x1 MP  $k$ -point grid and a mesh cutoff of 250 Ry were used in the 192-atom-supercell calculations, and a  $\Gamma$ -point sampling was used for the 432-atom calculation. In all supercell calculations, tolerance of  $\leq 0.01$  eV/Å was imposed on the residual forces in every atom. In order to obtain well converged DOS and PDOS for the defect supercells, MP grids of 16x16x1  $k$ -points were employed. In all cases, a double- $\zeta$  pseudoatomic basis set augmented with polarization orbitals (DZP basis) was employed, with an energy cutoff of 0.01 Ry, and the PBE-GGA functional to account for exchange and correlation effects [92]. Interactions between valence electrons and ionic cores were described by Troullier-Martins pseudopotentials [93]. Spin-polarization was considered in all cases.

In what follows, we discuss the spatial distribution of the electronic states that appear in the band gap due to the formation of each native defect we consider. We also discuss some examples of resonances that appear in the valence and conduction bands. We propose a simple

scheme to analyze the spatial structure of the defect-state wave functions, based on the orbital-projected density of states, that is described in detail in the Supplementary Information. In a few words, we analyze the PDOS to quantify and add up the contributions of the atomic-basis orbitals of each atom to the defect states (and resonances, in some cases), and plot this as a function of the distance of the atom from the defect center. We refer to these defect-state plots as wavefunction spatial profile,  $P_{wf}(R)$ .

With this simple scheme, we can distinguish between gap states and resonances that are very strongly localized, usually within  $\sim 5 \text{ \AA}$  from the defect center, and effective-mass-theory (EMT) states that show weaker exponential decay. EMT states, which are the standard description of shallow doping gap states in 3D crystals, are more delocalized, extending over a much larger portion of the lattice, away from the defect center. Furthermore, plots of isosurfaces of the charge density of the defect-state wavefunctions are also analyzed.

## 4.2 Vacancies

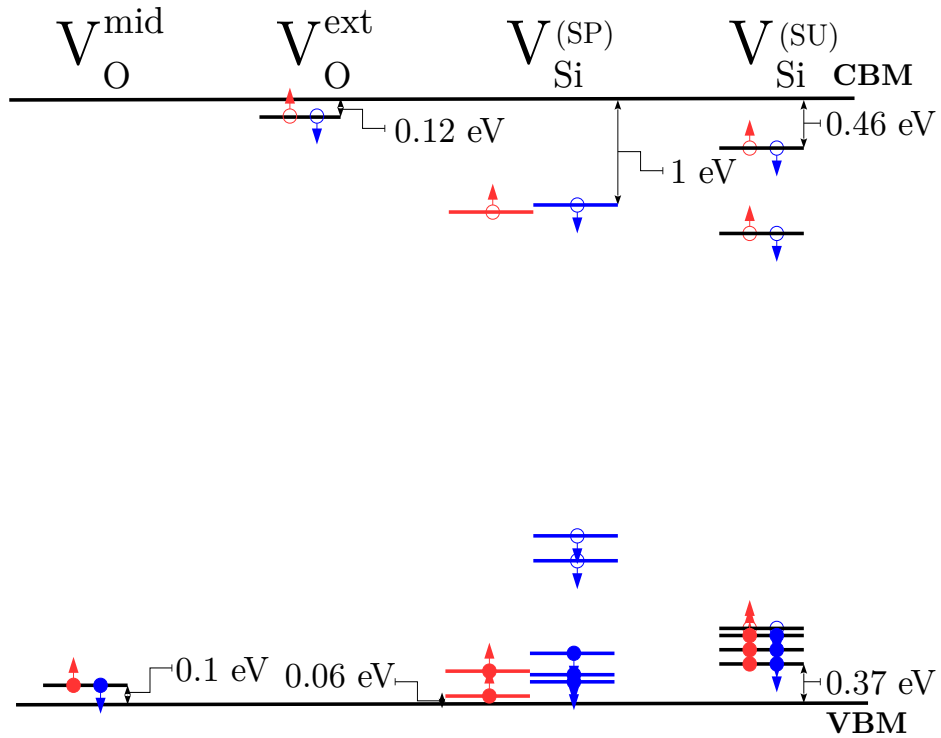


Figure 4.1: Schematic representation of the single-particle energy levels introduced in the fundamental band gap by oxygen and silicon vacancies in 2D-SiO<sub>2</sub>. To the silicon vacancy are showed the defect levels from spin polarized (SP), and spin unpolarized (SU) calculations.

We start our discussion of native defects in crystalline 2D-SiO<sub>2</sub> by examining the energy levels and the spatial distribution of the defect states generated by O and Si vacancies. As described above, in a freestanding bilayer of crystalline 2D-SiO<sub>2</sub> there are two inequivalent O-atom positions: (i) an interlayer one, in the intermediate layer of oxygen atoms connecting a Si atom on the top external layer to a Si atom on the bottom external layer; (ii) an intralayer

one, connecting two adjacent Si atoms on the same external Si honeycomb sublayer. In the case of Si, symmetry dictates that there is only one site, since all Si positions are symmetry related.

The defect levels of the three neutral vacancies are shown in Fig. 4.1. The labeling of the defects is as follows:  $V_{\text{O}}^{\text{mid}}$  is the interlayer oxygen vacancy that is formed by removing one oxygen atom from the middle (intermediate) layer.  $V_{\text{O}}^{\text{ext}}$  is the external-layer oxygen vacancy that is formed by removing one oxygen atom from either one of the two external layers.  $V_{\text{Si}}$  is a vacancy that is formed by removing a Si atom from either one of the two external layers.

### 4.2.1 Middle-Layer Oxygen Vacancy: $V_{\text{O}}^{\text{mid}}$

Let us first consider oxygen vacancies, the primary native defect center in crystalline and amorphous 3D-SiO<sub>2</sub>. [79] In the relaxed geometry of the  $V_{\text{O}}^{\text{mid}}$  defect, the local symmetry of the host lattice is only slightly broken at the defect site, due to small outwards in-plane shifts of the three middle-layer O atoms that are nearest to the vacant site, as shown in Figs. 4.2(a) and (b). Note that the top and bottom Si atoms, formerly bonded to the vacant O atom, move inwards towards the middle layer and form a 2.39 Å-long interlayer bond, 0.91 Å shorter than the original Si-O-Si chain and only 1.6% larger than a Si-Si bond in the diamond-structure bulk of a Si crystal (2.35 Å). These two Si atoms at the defect core are shown as grey spheres in Figs. 4.2(c) and (d).

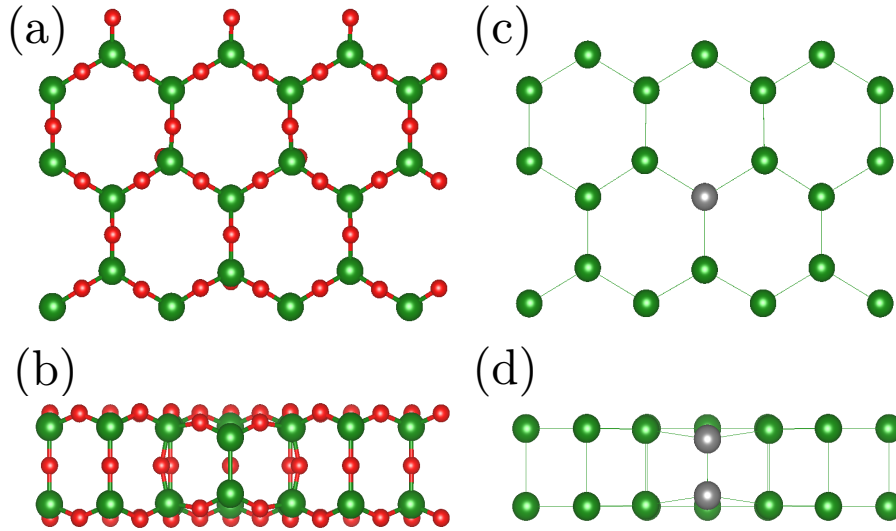


Figure 4.2: Relaxed geometry of the middle-layer oxygen vacancy,  $V_{\text{O}}^{\text{mid}}$ . (a) Top and (b) side views. Si (O) atoms are shown as green (red) spheres. (c) Top and (d) side views showing only the Si honeycomb sublattices. In (c) and (d), the two Si atoms that rebond at the defect core are shown as grey spheres, and the lines joining the Si atoms do not represent real bonds, and are drawn to show that the structure of the Si sublattices remain mostly undisturbed.

In Figs. 4.2(c) and (d), we show only the Si atoms in their positions in the  $V_{\text{O}}^{\text{mid}}$  configuration. We draw lines joining the Si atoms (that do not represent real bonds in 2D-SiO<sub>2</sub>) to show

that, after the removal of one middle-layer O atom, the lattice deforms very slightly and only in the very near vicinity of the defect core, and that the local structure of the Si honeycomb sublattices is very much unaffected after relaxation of the atomic structure of the defect.

Thus, we observe that the response of the atomic lattice to the formation of the  $V_{\text{O}}^{\text{mid}}$  defect consists essentially of two types of displacements of the O atoms in the middle of the Si-O-Si chains: (i) rotation about the axis joining the two Si atoms; (ii) displacements which change the angle at the O vertex in a Si-O-Si chain (a scissor mode). These rotation and scissor modes are low-energy structural excitations of the 2D-SiO<sub>2</sub> atomic lattice, and constitute the mechanism by which the 2D-SiO<sub>2</sub> lattice responds to the formation of all native defects in the present study. In a forthcoming publication, we will discuss the ubiquitous role of these structural modes in the response of 2D-SiO<sub>2</sub> lattice to external stresses and deformations.

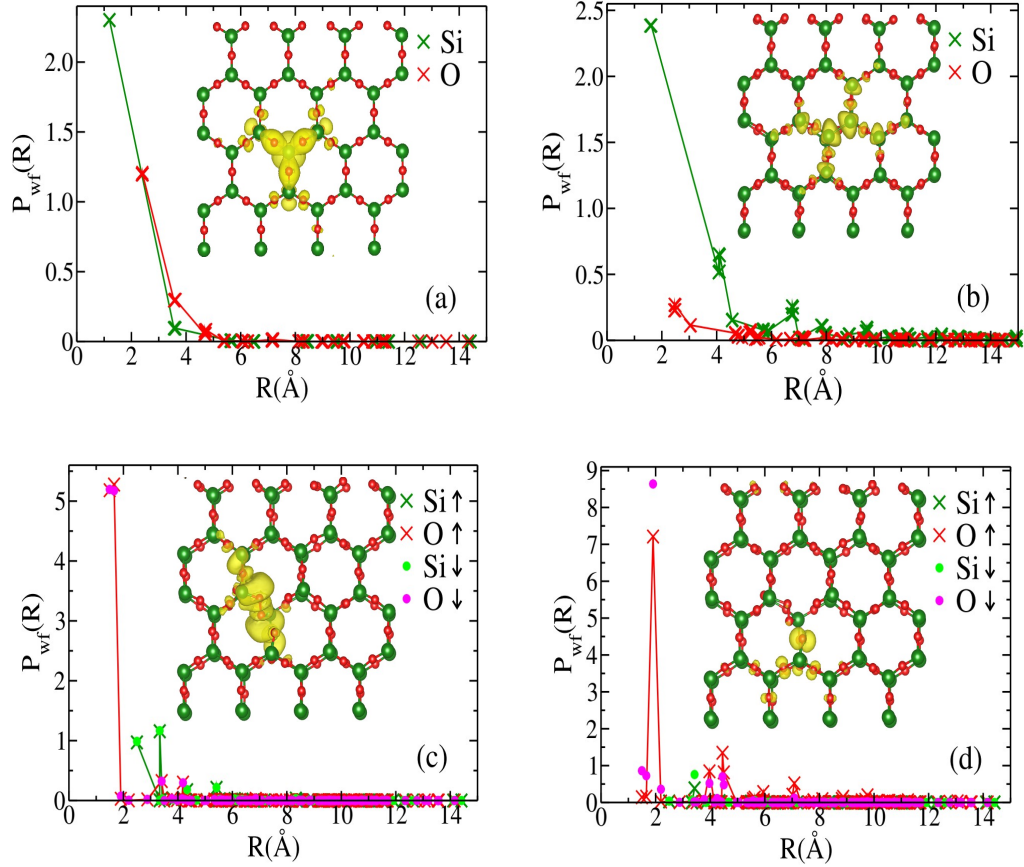


Figure 4.3: (a) Wave-function spatial profile as a function of the distance to the defect center,  $P_{\text{wf}}(R)$ , of a strongly-localized shallow defect state introduced in the band gap by the middle-layer oxygen vacancy,  $V_{\text{O}}^{\text{mid}}$ . (b)  $P_{\text{wf}}(R)$  of a strongly-localized shallow defect state introduced in the band gap by the external-layer oxygen vacancy,  $V_{\text{O}}^{\text{ext}}$ . (c)  $P_{\text{wf}}(R)$  of the strongly-localized spin-split pair of states introduced in the higher part of the band gap by the silicon vacancy,  $V_{\text{Si}}$ . Spin is indicated by arrows in the legend. The inset shows an isosurface of charge density of the majority-spin (spin up) state. (d)  $P_{\text{wf}}(R)$  of the rather shallow  $V_{\text{Si}}$  majority-spin state, at  $\varepsilon_{\text{vb}} + 0.06\text{eV}$ , and of its spin-split minority-spin partner at  $\varepsilon_{\text{vb}} + 0.48\text{eV}$ . The inset shows an isosurface of charge density of the shallow state. In (a), (b), and (d) insets display isosurfaces of the charge density of the shallow states, as another view of their strongly-spatially-localized character. In all cases, contributions to  $P_{\text{wf}}(R)$  from Si (O) orbitals are shown as dark and light green (red and magenta) symbols and guide-to-the-eye lines.

This  $V_{\text{O}}^{\text{mid}}$  defect geometry corresponds to the dimer configuration of O vacancies in 3D quartz and amorphous  $\text{SiO}_2$ . We recall that in the crystalline forms of 3D- $\text{SiO}_2$ , positively-charged O vacancies have another stable geometry, the so-called puckered configuration [79, 80, 86], where one of the Si atoms relaxes across the plane of its other three oxygen nearest neighbors and bonds with another O-atom in the 3D network, such as to restore its fourfold coordination. In the 2D- $\text{SiO}_2$  case, no other layer of O atoms is available, hence this puckered configuration cannot exist, since upon puckering the Si atom would find the vacuum above (below) the top (bottom) layer.

Figure 4.1(a) shows the band edges of the conduction and valence bands and the singly degenerate shallow level, at  $\varepsilon_{vb} + 0.10$  eV that is introduced in the gap by the  $V_{\text{O}}^{\text{mid}}$  defect in the neutral charge state. This level is fully occupied by two electrons with opposite spins, therefore  $V_{\text{O}}^{\text{mid}}$  is EPR inactive in the neutral state.

Considering only the energy eigenvalue for this defect state, we would be tempted to classify it as, potentially, a shallow acceptor doping level. However, the wave function of this state, shown in Fig. 4.3(a), displays a fast exponential decay, and is very strongly localized on the atoms in the immediate vicinity of the vacant O-atom site: orbitals from the two silicon atoms, nearest neighbors to the vacant site, account for 33% of the DOS peak of the defect state and the six nearest oxygen atoms (three on each of the two external layers) account for 51% of the defect-state DOS. Overall, the full wavefunction for the defect state is localized within  $\sim 5$  Å of the vacant site, as shown in Fig. 4.3(a). The inset in Fig. 4.3(a) shows an isosurface of the defect-state charge density, and provides another view of the strong localization of the shallow defect state. Therefore, despite being shallow in energy, the defect state is not an EMT state, and may act as a trapping center of carriers from the active layer in a prospective device employing 2D- $\text{SiO}_2$  as an insulating layer in a van der Waals stack.

This “pseudoshallow”  $V_{\text{O}}^{\text{mid}}$  defect state underscores a fairly general trend that we observe in the present work: a marked prevalence for the formation of strongly localized defect levels, be their energy shallow or deep within the band gap. Another trend we identify is the formation of localized states that are resonant within the bulk bands, near the edges of the valence and/or conduction bands.

In the case of  $V_{\text{O}}^{\text{mid}}$ , by zooming in on the electronic bands of the defect supercell, we identify three resonant states near the bottom of the conduction bands that are very strongly localized, within 4 Å from the defect center. This resonant states can be appreciated in detail looking to a highly converted density of states (DOS), identifying three plane states (indicated by red lines in the inset of the figure 4.4) and measuring the spatial localizations of the wavefunction of two of these resonances while the projected density of states  $P_{wf}$  (see figure). (the lowest and the highest in energy) The inset in this figure shows the bands for an interval of  $\sim 1.5$  from the bottom of the conduction band.

### 4.2.2 External-Layer Oxygen Vacancy: $V_{\text{O}}^{\text{ext}}$

By removing an oxygen atom from either one of the external layers, the intralayer  $V_{\text{O}}^{\text{ext}}$  defect, shown in Figs. 4.5(a) and (b), is formed. Its relaxed geometry shows an intralayer Si-Si

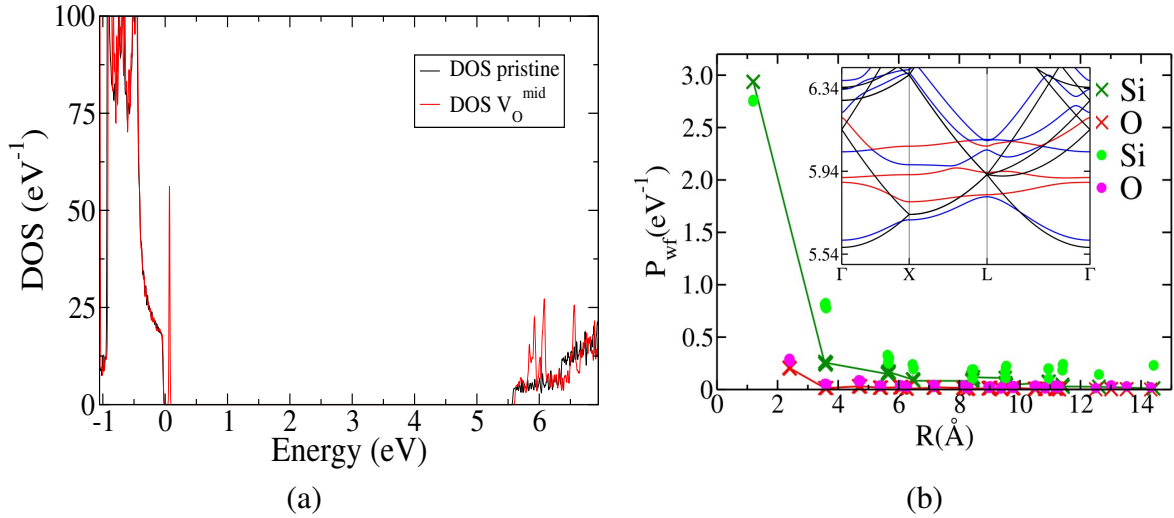


Figure 4.4: (a) Density of states (DOS) of the Middle-layer oxygen vacancy (red line) overlapped on the density of states from the bulk pristine supercell (black line). The defect state appears as a well defined peak near to the top of the valence band (defined as zero of energy). Three resonant states are showed in the botom of the conduction band. (b) Wave function spatial profiles, as a function of distance  $P_{\text{wf}}(R)$ , of the three strongly-localized defect-induced resonant states, neat to the bottom of the conduction bands, shown by red lines in the inset. In the inset, defect bands are shown as blue lines and bulk bands are shown as black lines.

bond, with a  $2.50 \text{ \AA}$  bond length replacing the Si-O-Si chain from which the O atom is removed. In this case also, the rotation and scissor modes of the O-atom sublattices dominate the response of the 2D-SiO<sub>2</sub> lattice to the introduction of the defect, and the symmetry of the Si sublattices is very nearly maintained, with a small symmetry reduction at the defect site due to the formation of the Si-Si bond, as shown in Fig. 4.5(c) and (d).

The  $V_O^{\text{ext}}$  defect is, in some respects, a reciprocal of the  $V_O^{\text{mid}}$ , in the sense that it introduces a singly-degenerate shallow defect state at  $\varepsilon_{cb} - 0.12 \text{ eV}$ . The defect level is empty in the neutral charge state of the defect, i.e., the neutral  $V_O^{\text{ext}}$  is also EPR inactive.

This is also a strongly localized pseudoshallow defect state, with most of its wavefunction concentrated on the orbitals of Si atoms within  $\sim 5 \text{ \AA}$  of the vacant site. In this case,  $\sim 62\%$  of the defect-state wavefunction derives from the atomic orbitals of the two silicon atoms that rebond after the removal of the oxygen atom, the four nearest oxygen atoms and the four next-nearest-neighbor silicon atoms, all in the same sublayer of the removed oxygen, as shown in Fig. 4.3(a). The figure shows the wavefunction fast spatial decay and the inset shows an isosurface of charge density for this gap state.

Again, despite being shallow in energy, the  $V_O^{\text{ext}}$  state in the topmost part of the band gap is not an EMT state, and may trap electron carriers from the active layer in a prospective 2D-semiconductor device employing 2D-SiO<sub>2</sub> as an insulating layer. Also in this case we identify strongly localized resonances near the bottom of the conduction band, as we can see examining the density of states of the supercell with the oxygen vacancy, zooming the bottom of the conduction band and also in the projected density of states that show the degree of localization of the wavefunction of the defect (see figure 4.6). That both oxygen vacancies display resonant states near the edge of the conduction band is related to the fact that a Si-

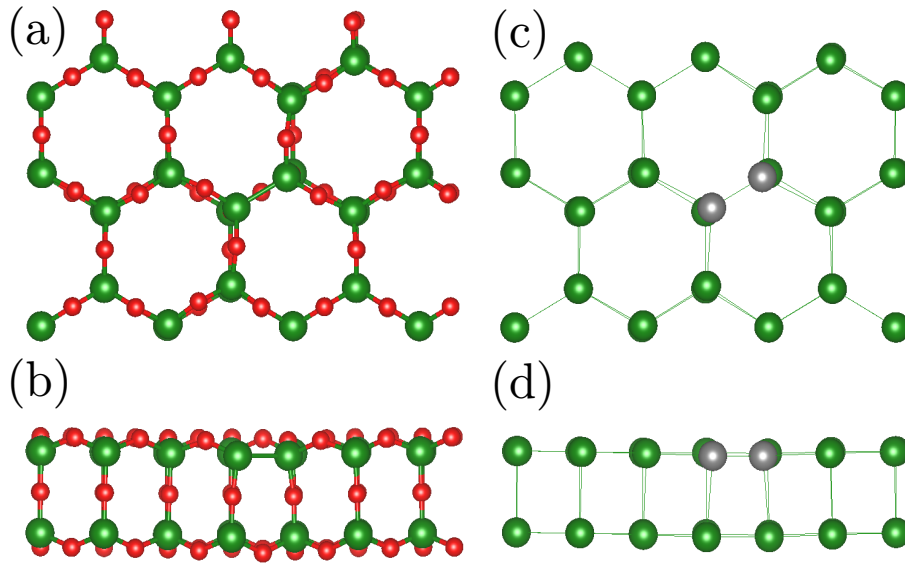


Figure 4.5: Relaxed geometry of the external-layer oxygen vacancy,  $V_{\text{O}}^{\text{ext}}$ . (a) Top and (b) side views. Si (O) atoms are shown as green (red) spheres. (c) Top and (d) side views showing only the Si honeycomb sublayers - see caption in Fig. 4.2. In (c) and (d), the two Si atoms that rebond at the defect core are shown as grey spheres.

Si bond is formed in the relaxed atomic structure of both defects, and the bottom of the conduction band derives entirely from Si orbitals.

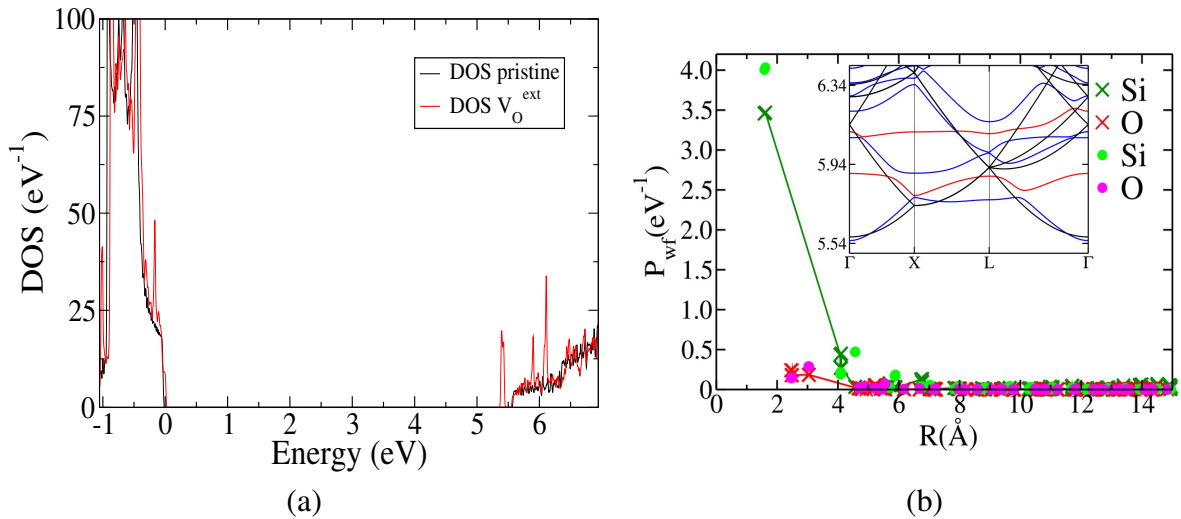


Figure 4.6: (a) Density of states (DOS) of the External-layer oxygen vacancy (red line) overlapped on the density of states from the bulk pristine supercell (black line). The defect state appears as a well defined peak near the bottom of the conduction band. Two resonant states are showed in the botom of the conduction band. (b) Wave function spatial profiles, as a function of distance  $P_{\text{wf}}(R)$ , of the two strongly-localized defect-induced resonant states, neat to the bottom of the conduction bands, shown by red lines in the inset. Defect bands are shown as blue lines and bulk bands are shown as black lines.

From the above discussion, we conclude that oxygen monovacancies are amphoteric trapping centers in 2D-SiO<sub>2</sub>, with activation of the nominally donor or acceptor states depending

on the Fermi level position and on whether the vacant site is on one of the external layers or in the middle oxygen layer.

### 4.2.3 Silicon Vacancy: $V_{\text{Si}}$

As discussed below, a silicon vacancy  $V_{\text{Si}}$  is a high-formation-energy defect, markedly so in Si-rich growth conditions. However, one must bear in mind that irradiation with high-energy electron beams has been used to introduce carbon vacancies (also high-formation-energy defects) in graphene, [94] and the same process may prove effective to engineer such defects in 2D-SiO<sub>2</sub>. Moreover, non-negligible concentrations of frozen-in Si vacancies result from rapid cooling of amorphous precursors, in 3D-SiO<sub>2</sub> samples. [79]

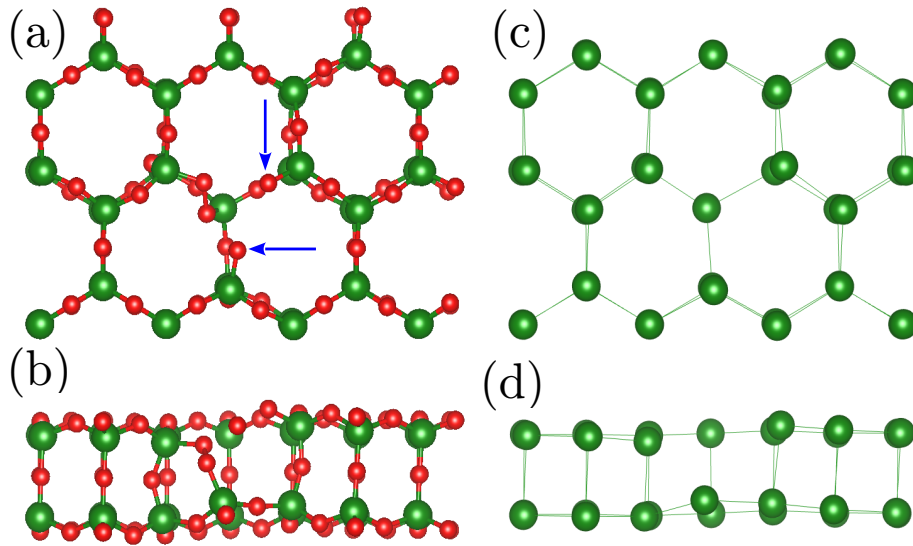


Figure 4.7: Relaxed geometry of the silicon vacancy,  $V_{\text{Si}}$ . (a) Top and (b) side views. Si (O) atoms are shown as green (red) spheres. In (a) the blue arrows show the two undercoordinated O atoms in the core of the defect. (c) Top and (d) side views showing only the Si honeycomb sublayers - see caption in Fig. 4.2.

Regarding the atomic structure, the relaxed geometry shows symmetry reduction over a somewhat larger portion of the surrounding lattice, when compared with  $V_{\text{O}}^{\text{mid}}$  and  $V_{\text{O}}^{\text{ext}}$ , and displays a partial reconstruction of the four broken bonds that appear due to the vacant Si atom. Figures 4.7(a) and (b) show the geometry of the partially reconstructed defect, after the removal of a Si from the top layer. As described above, in the pristine 2D-SiO<sub>2</sub> lattice each Si atom bonds to three O atoms in the same external sublayer and to one O atom in the intermediate layer. Upon removal of a Si atom, a bond is formed between an external layer O atom and the middle-layer O atom, such that a Si-O-O-Si chain is formed at the defect core, and each one of the other two external layer O atoms, formerly bonded to the vacant Si, are now undersaturated. The presence of O-atom dangling bonds, and the Si-O-O-Si bonding



chain, not present in the host lattice, are the main reasons for the high-formation energy of this defect.

Figures 4.7(c) and (d) show that even after the removal of a Si atom, substantial rebonding, and formation of the Si-O-O-Si chain, the two Si honeycomb sublattices are only mildly perturbed, being deformed more strongly only at the very core of the defect. Once again, we observe that in the relaxed geometry of the  $V_{\text{Si}}$  defect, besides the formation of the Si-O-O-Si chain, the scissor and rotation displacements of nearby O atoms constitute the mechanism by which the surrounding lattice responds to the perturbation.

Figure 4.1 shows the  $V_{\text{Si}}$  energy levels in the gap obtained from spin-unpolarized and spin-polarized calculations. The calculation without the inclusion of spin polarization yields five singly-degenerate defect states introduced in the fundamental band gap by the  $V_{\text{Si}}$  defect, four of them in the lower half and one in the upper half of the band gap. In the neutral state of  $V_{\text{Si}}$ , the three lower levels are fully occupied with two electrons of opposite spins, and the two higher levels are empty. These defect states are composed essentially of atomic orbitals of the two undersaturated external-layer oxygen atoms (indicated by blue arrows in Fig. 4.7), and the atoms in the Si-O-O-Si chain at the core of the defect. In the spin-unpolarized calculation, all five gap states of the  $V_{\text{Si}}$  defect are very strongly localized in the immediate neighborhood of the defect center, regardless of being shallow or deep in the band gap.

From a spin-polarized calculation, the inclusion of exchange splitting has a dramatic effect. In the minority-spin channel, shown as blue lines in Fig. 4.1, we obtain three occupied and three unoccupied gap states, while the majority spin channel has only three energy levels in the band gap, two of which are occupied. The  $V_{\text{Si}}$  defect has a net spin of  $1 \mu_B$  (one Bohr magneton) in the neutral state.

In order to understand this defect-level structure, we must consider that spin splitting has pushed majority spin states downwards, such that they become resonant within the valence band. The  $V_{\text{Si}}$  defect is a telling example of the occurrence of strongly-localized defect-induced resonances in a 2D-SiO<sub>2</sub> bilayer. Below, we describe a spin-split pair consisting of a minority-spin gap state and a majority-spin valence-band resonance.

Overall, for the  $V_{\text{Si}}$  defect we have the following scenario:

(i) the two defect states with opposite spins in the higher part of the gap, in Fig. 4.1(c) result from a small spin splitting (72 meV) of the higher gap state from the spin-unpolarized calculation in Fig. 4.1(d). These states are composed essentially of orbitals from the two O and two Si atoms (predominantly from the O atoms) forming the Si-O-O-Si chain at the core of the defect. The wave-function spatial profiles for these defect states are shown in Fig. 4.3(c). They mirror each other and show strong localization near at defect core. The inset shows an isosurface of charge density for the majority-spin gap state, providing another perspective on its strong spatial localization.

(ii) The suite of four gap states spanning a small energy interval in the bottom part of the gap, from the spin unpolarized calculation, gives rise to complex effects of exchange spin splitting that push majority-spin states into the valence band as resonances and pulls one resonant minority-spin state from the valence band into the gap.

Figure 4.3(d) shows the wavefunctions of the rather shallow  $V_{Si}$  defect level, a majority-spin state with an energy of  $\epsilon_{vb} + 0.06$  eV, and of its spin-split minority-spin partner at  $\epsilon_{vb} + 0.48$  eV. Both states are composed mainly of the dangling bond orbitals of the O atom indicated by a blue horizontal arrow in Fig. 4.7. An isosurface of charge density for the shallow majority-spin state is shown in the inset. This is a prototype example of the tendency of formation of shallow states with strongly localized wavefunctions that we identify in the 2D-SiO<sub>2</sub> bilayer.

By examining the band structure of the defect supercell, we are able to identify a strongly localized majority-spin valence-band resonance at  $\epsilon_{vb} - 0.20$  eV and its spin-split partner in the band gap, a minority spin state at  $\epsilon_{vb} + 0.26$  eV, both states derived mainly from dangling bonds of the other undercoordinated O atom in the core of the  $V_{Si}$  defect, indicated by a blue vertical arrow in Fig. 4.7. The density of states of the silicon vacancy, the wavefunction profiles for these spin-split partners and an isosurface of charge density for the minority-spin gap state are shown in figure 4.8. Note that the resonant state does not decay to zero away from the defect center due to some degree of hybridization with the delocalized states in the valence band. Moreover, the spin-splitting energy is much larger for these latter spin-split pairs of states (0.42 and 0.46 eV) than for the states in the higher part of the gap.

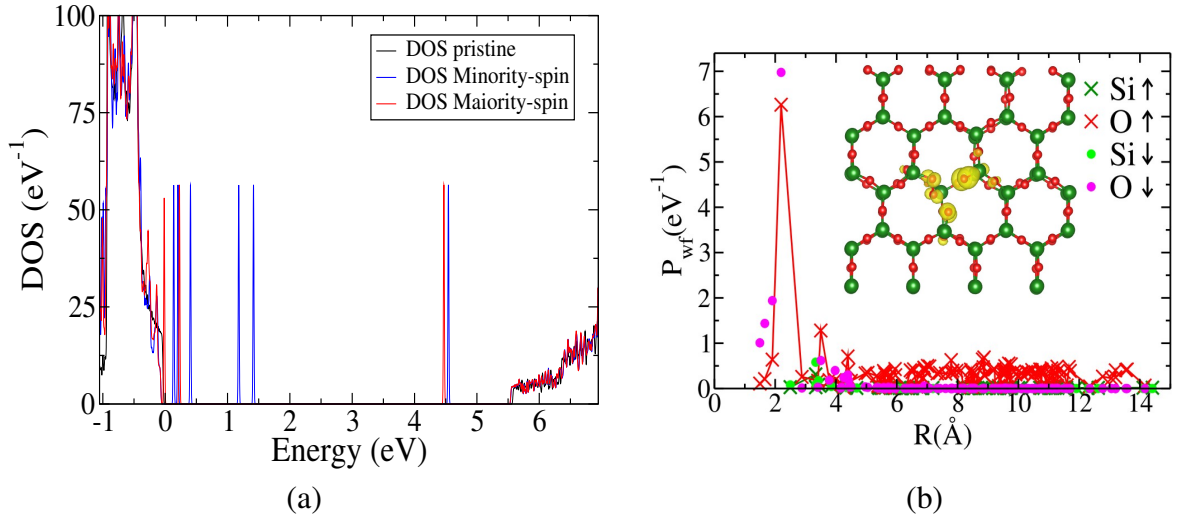


Figure 4.8: (a) Density of states (DOS) of the silicon vacancy (red and blue lines) overlapped on the density of states from the bulk pristine supercell (black line). The defect states appear as very well defined blue and red peaks on the gap, most of them near to the valence band. Blue lines indicate the spin minority channel and red lines the spin majority channel. Two resonant states are shown in the bottom of the conduction band. (b)  $P_{wf}(R)$  of a majority-spin valence-band resonance at  $\epsilon_{vb} - 0.2$  eV and of its spin-split partner in the band gap, a minority spin state at  $\epsilon_{vb} + 0.26$  eV, both states derived mainly from dangling bonds of the other undercoordinated O atom in the core of the  $V_{Si}$  defect. The inset shows an isosurface of charge density of the minority spin (spin down) state in the gap.

## 4.3 Interstitials

We shift gears now and consider single O and Si interstitials. Figure 4.9 shows the initial positions that we consider for an interstitial Si or O atom before geometry optimization: (a) an

additional O (Si) atom placed on an interstitial site in the oxygen middle layer; (b) additional Si atom placed at the center of an external-layer hexagon; (c) additional O atom placed on an external-layer hexagon.

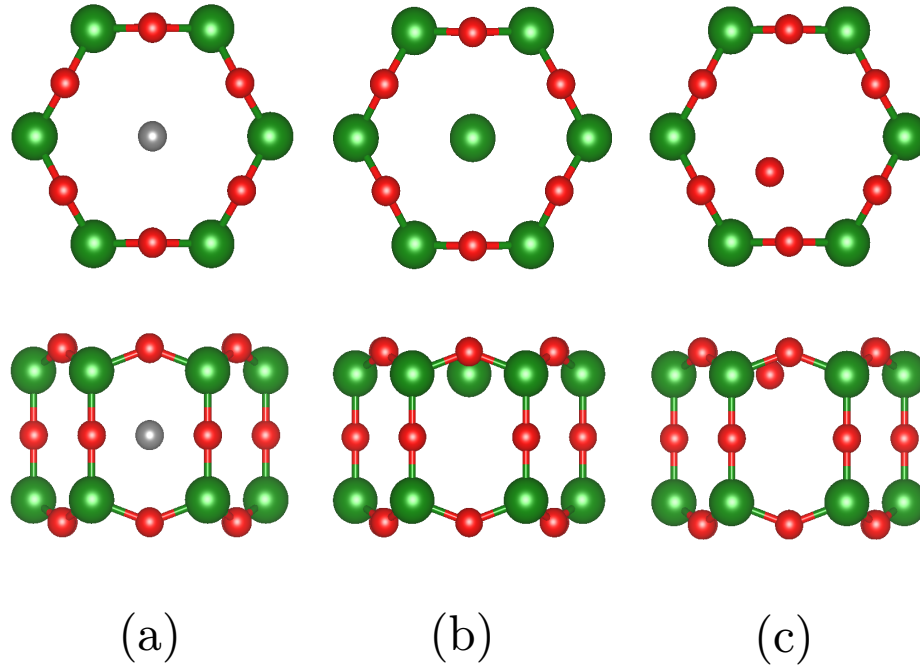


Figure 4.9: Detail of the initial positions of interstitial atoms at the start of the geometry-relaxation procedure. The figure shows only the hexagon where the interstitial atom is initially placed, and not the full supercell. (a) Top and side views of the initial position of a Si or an O interstitial (gray sphere) in the middle layer. (b) Top and side views of the initial position of a Si interstitial in the external layer. (c) Top and side views of the initial position of an O interstitial in the external layer. Si (O) atoms are shown as green (red) spheres.

Oxygen atoms are usually stabilized in low-coordination environments, such as in 2D-SiO<sub>2</sub> where each O atom is twofold coordinated. As a result, from the initial positions described above we obtain two stable configurations of oxygen split interstitials in 2D-SiO<sub>2</sub>. On the other hand, Si atoms prefer higher coordination environments, and for that reason, in the case of a single Si interstitial, we obtain only one equilibrium position where the Si atom moves inwards and bonds with the nearest O atom in the middle layer, for both initial positions shown in Fig. 4.9. We emphasize that even when initially placed on the external layer, an interstitial Si atom migrates to the middle layer and bonds with the closest middle-layer O atom, the driving force being the low-coordination of available external-layer sites that renders the puckered configuration of the oxygen vacancy unstable in 2D-SiO<sub>2</sub>, as discussed above.

The defect levels introduced in the fundamental band gap by the three interstitial species are shown in Fig. 4.10. Below, we discuss the geometry and electronic structure of each case separately.

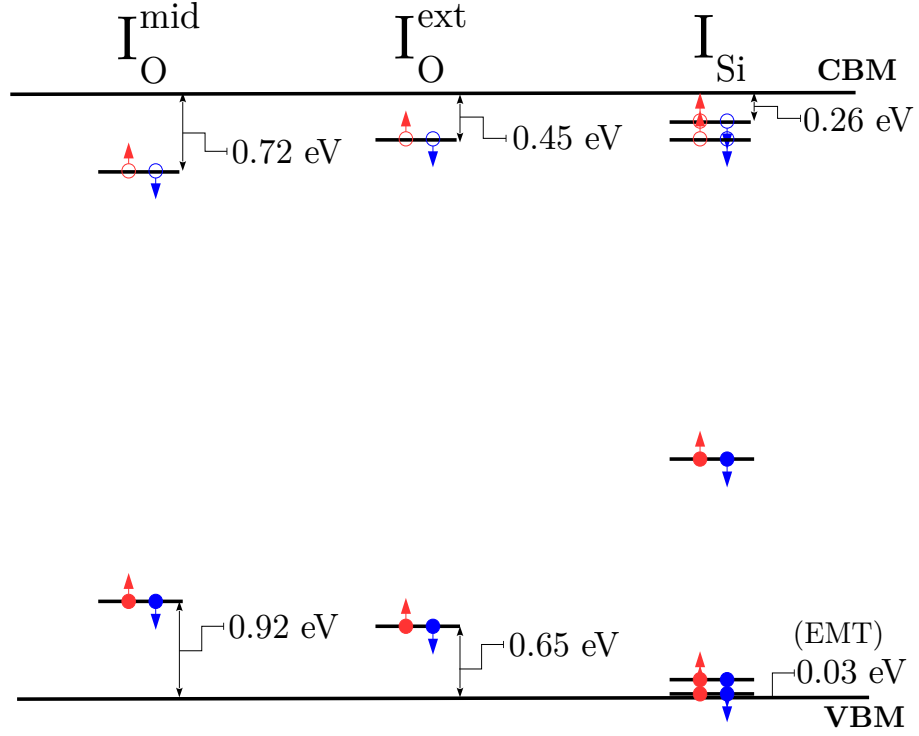


Figure 4.10: Schematic representation of the single-particle energy levels introduced in the fundamental band gap by oxygen and silicon interstitials in 2D-SiO<sub>2</sub>.

### 4.3.1 Oxygen Split-Interstitials: $I_{\text{O}}^{\text{ext}}$ and $I_{\text{O}}^{\text{mid}}$

For both initial positions we consider, after relaxation the interstitial O atom forms split interstitials in Si-O-O-Si chains at the defect core. Starting from the initial position in Fig. 4.9(a), a stable O-interstitial configuration is obtained, the  $I_{\text{O}}^{\text{mid}}$ , where the interstitial O atom bonds with a middle-layer O atom, forming a Si-O-O-Si chain with one Si atom from each of the external layers, as shown in Fig. 4.11. From the external layer position, the  $I_{\text{O}}^{\text{ext}}$  defect is formed, where the interstitial O atom bonds with the O atom from an external-layer Si-O-Si chain and with an external-layer Si atom, as shown in Fig. 4.12. The  $I_{\text{O}}^{\text{ext}}$  is the more stable form of an oxygen interstitial, with a formation energy that is 2.27 eV lower than  $I_{\text{O}}^{\text{mid}}$ , as discussed below.

In both cases, the positions of the two O atoms making up the split interstitial are very nearly symmetric with respect to the original position of the O atom in the Si-O-Si chain to which the interstitial atom attaches itself. Again, in both cases the local symmetry breaking induced by the formation of the interstitials is localized in the immediate neighborhood of defect core, and involves essentially scissor and rotation modes of the O atoms in the near vicinity of the defect core, along the zigzag line of Si-O-Si bonds where the interstitial is formed. The symmetry of the Si sublattice is only disturbed at the very core of the defects, as shown in Figs. 4.11(c) and (d) and 4.12(c) and (d).

The electronic structures of the two O interstitials are very similar. In both cases we obtain a pair of deep gap states, one in the lower half of the gap and the other in the upper half of the gap. The energies are, respectively,  $\varepsilon_{vb} + 0.91$  eV and  $\varepsilon_{cb} - 0.72$  eV, for the  $I_{\text{O}}^{\text{mid}}$ , and

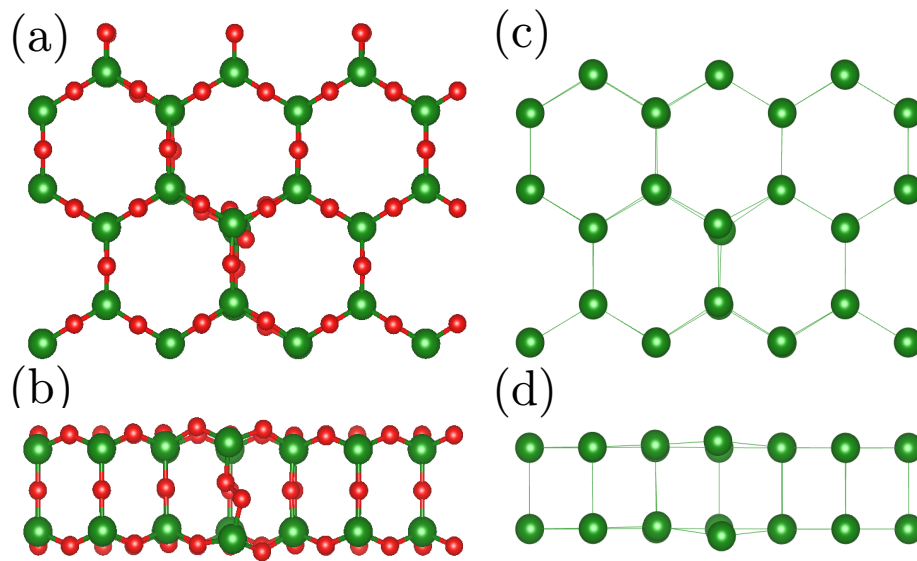


Figure 4.11: Relaxed geometry of the middle-layer oxygen interstitial,  $I_{\text{O}}^{\text{mid}}$ . (a) Top and (b) side views. Si (O) atoms are shown as green (red) spheres. (c) Top and (d) side views showing only the Si honeycomb sublayers - see caption in Fig. 4.2.

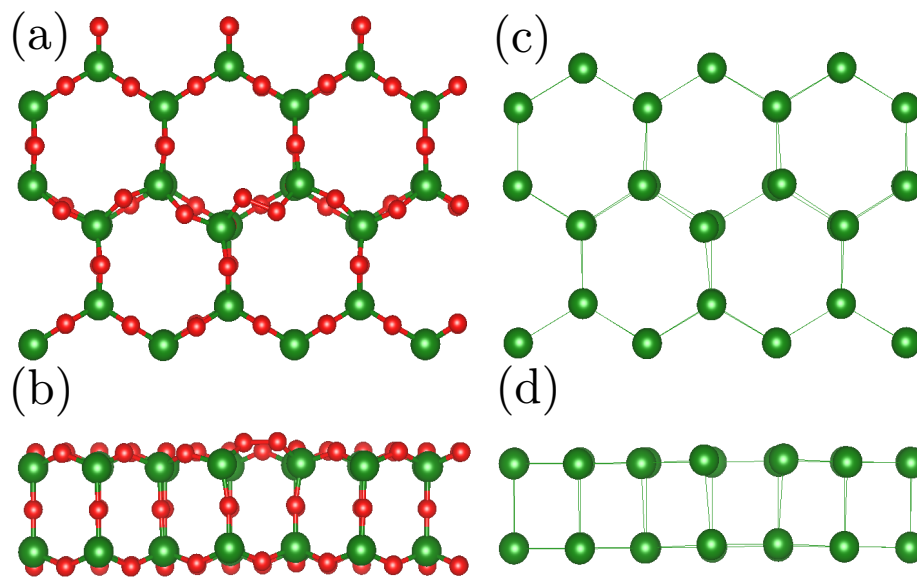


Figure 4.12: Relaxed geometry of the external-layer oxygen interstitial,  $I_{\text{O}}^{\text{ext}}$ . (a) Top and (b) side views. Si (O) atoms are shown as green (red) spheres. (c) Top and (d) side views showing only the Si honeycomb sublayers - see caption in Fig. 4.2.

$\varepsilon_{vb} + 0.65 \text{ eV}$  and  $\varepsilon_{cb} - 0.45 \text{ eV}$  for the  $I_{\text{O}}^{\text{ext}}$ . Hence, both  $I_{\text{O}}$  centers we identify are amphoteric, with deep donor and acceptor levels.

No spin splitting of the defect levels results from our spin-polarized calculations in either

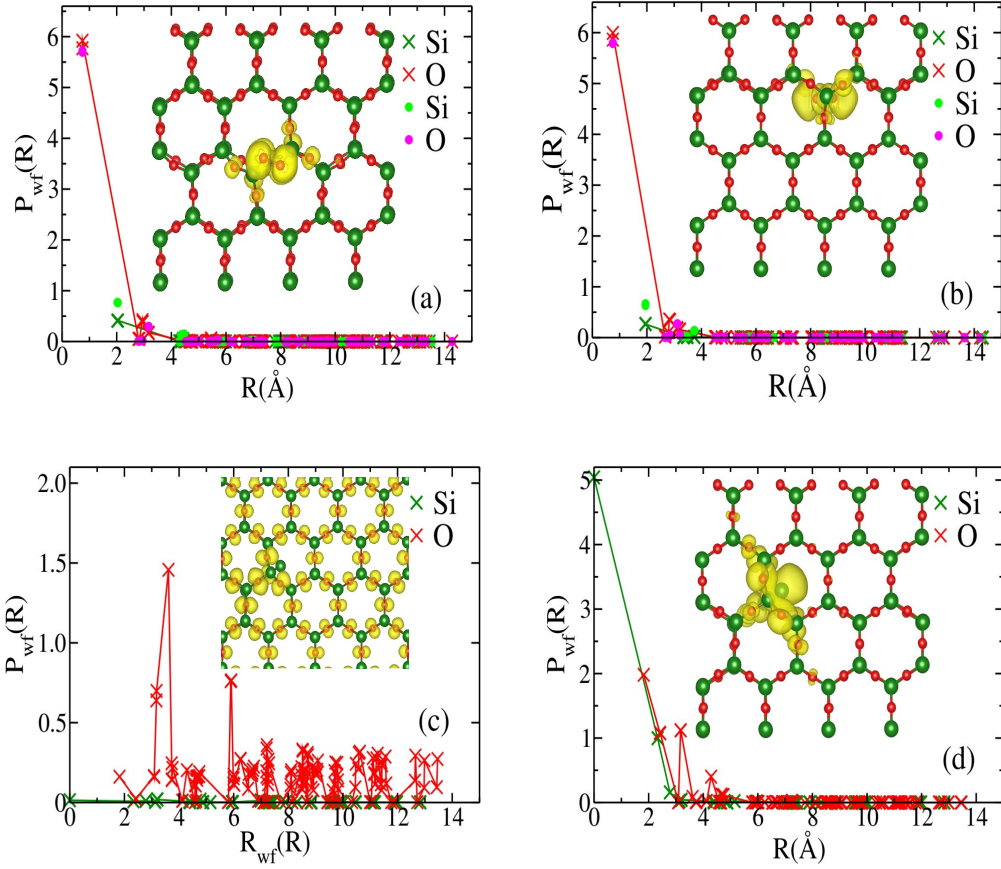


Figure 4.13: (a) Wave function spatial profile,  $P_{wf}(R)$ , of the two strongly-localized gap states introduced by the external-layer oxygen interstitial,  $I_O^{\text{ext}}$ . The inset shows an isosurface of charge density of the state in the lower part of the gap. (b)  $P_{wf}(R)$  of the two strongly-localized gap states introduced by the middle-layer oxygen interstitial,  $I_O^{\text{mid}}$ . The inset shows an isosurface of charge density of the state in the higher part of the gap. (c)  $P_{wf}(R)$  of the very shallow gap state at  $\epsilon_{vb} + 0.03$  eV, introduced by the silicon interstitial,  $I_{Si}$ . The inset shows an isosurface of charge density of this shallow state. The effective-mass-theory nature of the state is displayed by a wave-function that extends over the entire supercell. (d)  $P_{wf}(R)$  of the strongly-localized marginally-shallow gap state at  $\epsilon_{vb} + 0.15$  eV, introduced by  $I_{Si}$ . The inset shows an isosurface of charge density of this shallow state. In all cases, the contributions to  $P_{wf}(R)$  from Si (O) orbitals are shown as dark and light green (red and magenta) symbols and guide-to-the-eye lines.

$I_O^{\text{mid}}$  or  $I_O^{\text{ext}}$ . The wavefunctions for the two gap states, for both  $I_O$  species, are essentially the bonding and antibonding combinations of the O-O bond at the cores of the two  $I_O$  species. The orbitals in these two O atoms account for nearly the full wavefunction of both defect states, in each case. Figure 4.13(a) and (b) shows that these are very localized deep defect states, with their wavefunctions decaying to zero within  $\sim 3.5 \text{ \AA}$  from the defect center. The inset in Figure 4.13(a) shows a charge-density isosurface for the  $\epsilon_{vb} + 0.65$  eV level of  $I_O^{\text{ext}}$  and Fig. 4.13(b) shows the isosurface for the  $\epsilon_{cb} - 0.72$  eV of  $I_O^{\text{mid}}$ . Finally the density of states corresponding to both oxygen interstitials are showed in figure 4.14.

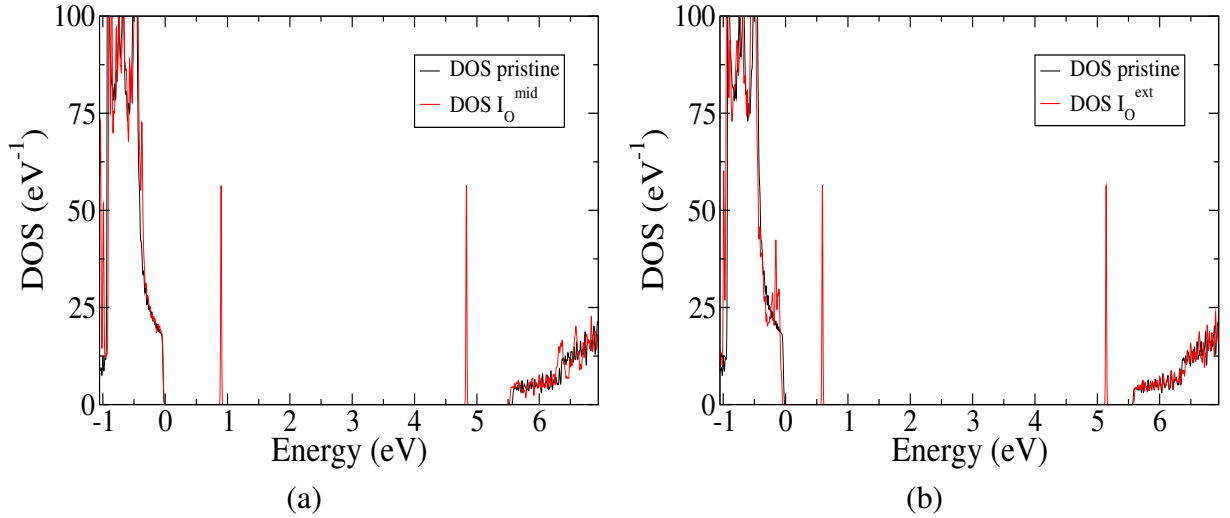


Figure 4.14: (a) Density of states (DOS) of the Middle interstitial oxygen (red lines) overlapped on the density of states from the bulk pristine supercell (black line). The defect states appear as two very well defined red peaks, each one near to the edge of each band. (b) Density of states (DOS) of the External interstitial oxygen (red lines) overlapped on the density of states from the bulk pristine supercell (black line). The defect states appear as two very well defined red peaks, each one near to the edge of each band.

### 4.3.2 Silicon Interstitial: $I_{Si}$

A Si interstitial in crystalline 2D-SiO<sub>2</sub> is stable only in an interstitial site of the intermediate oxygen layer, as shown in Fig. 4.15, where the relaxed configuration of the  $I_{Si}$  defect is displayed. In the figure, it is observed that a Si-O bond from the pristine bilayer, between a Si atom in the top layer and the O atom in the middle layer, is replaced by a Si-Si bond between the interstitial and the top layer Si atom, while the middle-layer O atom also bonds with the Si interstitial, forming a Si-Si-O-Si chain at the core of the defect. All core atoms but the interstitial Si atom itself recover their pristine-lattice coordination.

Again, the surrounding lattice retains the symmetry of the pristine system, with symmetry reduction confined to a small region surrounding the defect core. Thus, even in this case, where a large interstitial atom is inserted in the 2D-SiO<sub>2</sub> bilayer, we observe that the lattice responds to the perturbation through scissor and rotation modes of the O atoms in the vicinity of the defect, with the external honeycomb sublattices of Si atoms being disturbed only in a very small region surrounding the defect center.

The  $I_{Si}$  is in a rather low twofold coordination, which explains a plethora of five defect-state energy levels in the band gap associated with the  $I_{Si}$  defect, as shown in Fig. 4.10. Unlike in the case of the Si vacancy, in the neutral charge state no spin polarization effects are observed in this case, hence the neutral  $I_{Si}$  center is EPR inactive.

Of the five  $I_{Si}$  gap states in Fig. 4.10, the lowest one is a very shallow level at  $\epsilon_{vb} + 0.03$  eV, which wave function is shown in Fig. 4.13(c). The figure clearly shows an EMT state displaying a slow decay away from the defect center, with sizeable contributions to the wavefunction from atoms over the entire supercell, a profile that is confirmed by the charge-density isosurface in the inset. As expected, the wavefunction of this EMT state is dominated

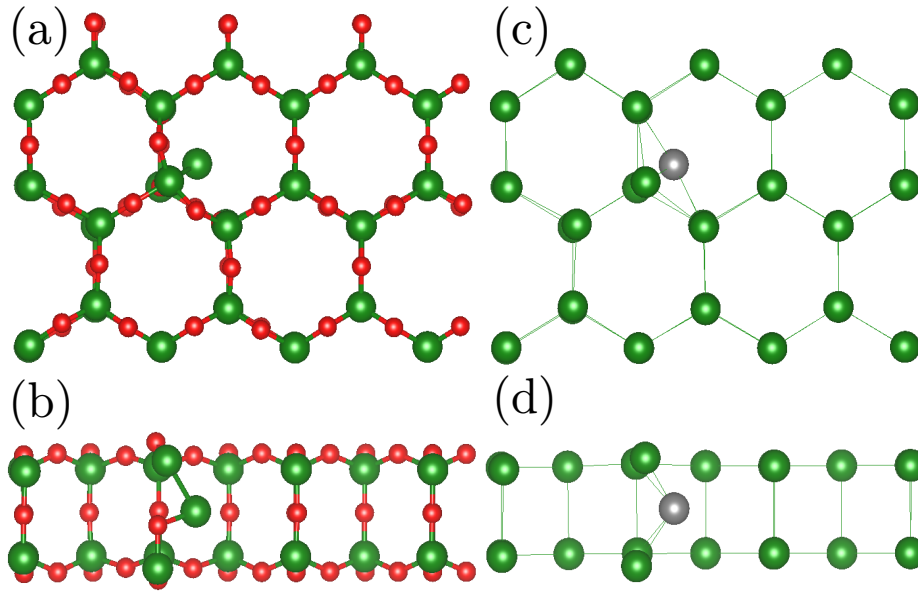


Figure 4.15: Relaxed geometry of the silicon interstitial,  $I_{Si}$ . (a) Top and (b) side views. Si (O) atoms are shown as green (red) spheres. Interstitial Si atom is shown as grey sphere. (c) Top and (d) side views showing only the Si honeycomb sublayers - see caption in Fig. 4.2.

by the  $p$ -orbitals of the external layers atoms, which is the character of the states at the top of the valence band.

Moving up in energy, in the band gap, we find a marginally shallow state at  $\epsilon_{vb} + 0.15$  eV, followed by a very deep level at  $\epsilon_{vb} + 2.23$  eV. The shallow state at  $\epsilon_{vb} + 0.15$  eV derives its wavefunction from atomic orbitals of the interstitial Si atom, the Si atom that bonds to it, the three middle-layer O atoms that are nearest to the interstitial Si, and the two top-layer O atoms that are nearest to the interstitial Si, as shown in Fig. 4.13(d). This is another example of a shallow state that is not an EMT state, being actually a very localized state with a wavefunction that is confined within  $\sim 3.5\text{\AA}$  from the defect center.

Further up in the higher part of the gap, we find another deep level at  $\epsilon_{cb} - 0.42$  eV, and another marginally shallow level  $\epsilon_{cb} - 0.26$  eV. Overall, except for the very shallow EMT state described above, the other four gap states introduced by the  $I_{Si}$  defect are strongly localized, within  $\sim 3.5\text{\AA}$  from the defect center. In particular the two marginally shallow levels, the acceptor at  $\epsilon_{vb} + 0.15$  eV and the donor at  $\epsilon_{cb} - 0.26$  eV, display strongly localized wavefunctions, as shown in figure 4.16b, i.e., despite being shallow states, neither is an EMT state. Also the density of states of the interstitial silicon is showed in fig 4.16a.

## 4.4 Formation energy of vacancies and interstitials

The formation energy of a neutral defect is essentially the difference between the energy of a supercell with the defect and that of a pristine supercell without the defect, taking into account the chemical potentials of each atomic species, in order to properly compare systems



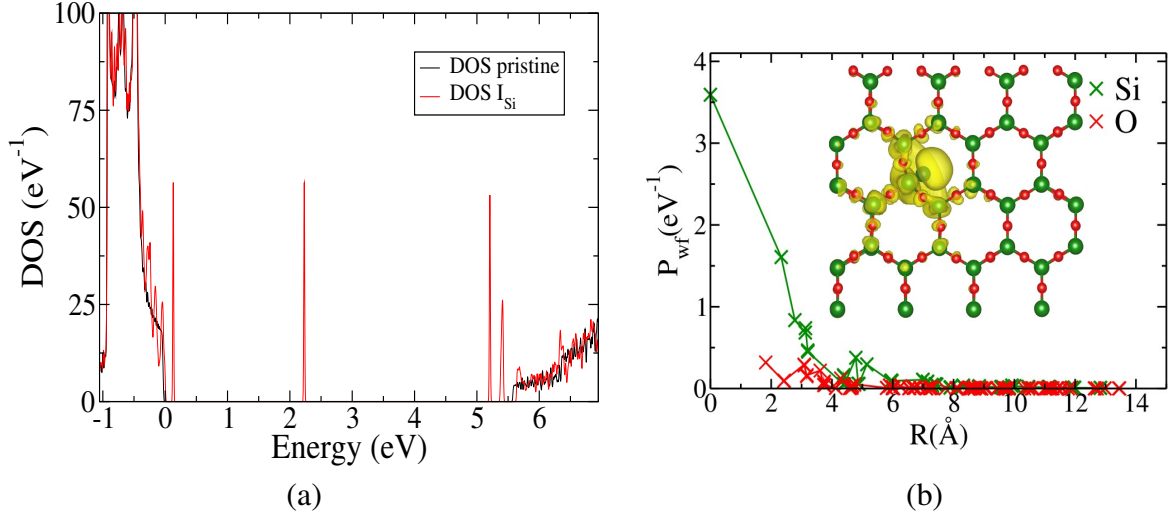


Figure 4.16: (a) Density of states (DOS) of the Interstitial silicon (red line) overlapped on the density of states from the bulk pristine supercell (black line). The defect states appear as very well defined blue and red peaks on the gap. The true EMT state appear as the first peak just in the edge of the valence band. (b)  $P_{\text{wf}}(R)$  of the strongly-localized marginally shallow gap state at  $\epsilon_{cb}-0.26$  eV, introduced by  $I_{\text{Si}}$ . The inset shows an isosurface of charge density of this gap state.

with different stoichiometries, as follows:

$$E_f^d = E_{\text{tot}}^d - E_{\text{tot}}^{\text{bulk}} + \sum_i n_i \mu_i ; \quad (4.1)$$

where  $E_{\text{tot}}^d$  is the total energy of a supercell with defect  $d$ ,  $E_{\text{tot}}^{\text{bulk}}$  is the total energy of the corresponding (same supercell size) pristine bulk supercell, and  $n_i$  and  $\mu_i$  are the quantities and chemical potentials of the atoms exchanged with the corresponding chemical-potential reservoirs, when the defect is created. In the cases we consider in this work, there is only one atom exchanged with the chemical-potential reservoirs: one atom is removed from the 2D-SiO<sub>2</sub> bilayer in the case of single vacancies, and one atom is added in the case of single interstitials.

The chemical potentials of Si and O are determined by imposing a condition of thermodynamical equilibrium between the 2D-SiO<sub>2</sub> bilayer and the reservoirs of Si or O atoms employed in the synthesis of the bulk material. The 2D-SiO<sub>2</sub> bulk is obtained by electron beam deposition (EBD) where a Si sample is exposed to an electron beam that heats it up, creating a vapour of silicon atoms in a gaseous O<sub>2</sub> environment [6]. The thermodynamical equilibrium condition requires:

$$\mu_{\text{SiO}_2} = \mu_{\text{Si}} + \mu_{\text{O}_2} = \mu_{\text{Si}} + 2\mu_{\text{O}} ; \quad (4.2)$$

where  $\mu_{\text{SiO}_2}$  is the calculated total energy per formula unit of a pristine SiO<sub>2</sub> bilayer. We define two limits for the synthesis: Si-rich and O-rich conditions.

In the Si-rich scenario, a gas of Si atoms in equilibrium with a bulk Si is present, and the value of  $\mu_{\text{Si}}$  is obtained from the calculated total energy per atom of diamond-lattice bulk Si.

Table 4.1: Chemical potentials of silicon and oxygen and formation energies (in eV) of neutral native defects in 2D-SiO<sub>2</sub>, for Si-rich and O-rich conditions.

	Si-rich limit (eV)	O-rich limit (eV)
$\mu_{\text{O}}$	-439.10	-434.74
$\mu_{\text{Si}}$	-245.02	-253.74
$V_{\text{O}}^{\text{mid}}$	0.59	4.95
$V_{\text{O}}^{\text{ext}}$	1.03	5.39
$V_{\text{Si}}$	13.23	4.53
$I_{\text{O}}^{\text{mid}}$	7.97	3.61
$I_{\text{O}}^{\text{ext}}$	5.70	1.34
$I_{\text{Si}}$	4.02	12.72

In this condition, the oxygen chemical potential is obtained from the equilibrium condition, Eq. 4.2, as

$$\begin{aligned} \text{Si-rich:} \quad \mu_{\text{Si}} &= \frac{E_{tot}^{\text{Si}}}{N_{\text{Si}}} ; \\ \mu_{\text{O}} &= \frac{(\mu_{\text{SiO}_2} - \mu_{\text{Si}})}{2} . \end{aligned} \quad (4.3)$$

where  $E_{tot}^{\text{Si}}$  is the total energy of an  $N_{\text{Si}}$ -atom Si-bulk unit cell.

On the other hand, in the O-rich scenario, the oxygen chemical potential  $\mu_{\text{O}}$  is obtained from a calculations for an O<sub>2</sub> molecular gas, and the Si chemical potential is given by the equilibrium condition, Eq 4.2, as

$$\begin{aligned} \text{O-rich:} \quad \mu_{\text{O}} &= \frac{E_{tot}^{\text{O}_2}}{2} ; \\ \mu_{\text{Si}} &= (\mu_{\text{SiO}_2} - 2\mu_{\text{O}}) . \end{aligned} \quad (4.4)$$

where  $E_{tot}^{\text{O}_2}$  is the total energy of a calculation for an O<sub>2</sub> molecule in a supercell with large vacuum regions in all three directions.

More specifically, for the the formation energy of a vacancy in the neutral charge state, from the total energy of a 2D-SiO<sub>2</sub> supercell with  $N_{\text{Si}}$  formula units and one missing O (Si) atom, we obtain:

$$E_f^{\text{V}_\text{O}} = E_{tot}^{\text{V}_\text{O}} + \mu_{\text{O}} - E_{tot}^{\text{SiO}_2}(N_{\text{Si}}) , \quad (4.5)$$

$$\begin{aligned} E_f^{\text{V}_\text{Si}} &= E_{tot}^{\text{V}_\text{Si}} + \mu_{\text{Si}} - E_{tot}^{\text{SiO}_2}(N_{\text{Si}}) \\ &= E_{tot}^{\text{V}_\text{Si}} + \mu_{\text{SiO}_2} - 2\mu_{\text{O}} - E_{tot}^{\text{SiO}_2}(N_{\text{Si}}) ; \end{aligned} \quad (4.6)$$

where  $E_{tot}^{\text{SiO}_2}(N_{\text{Si}})$  is the total energy of a pristine 2D-SiO<sub>2</sub> cell with  $N_{\text{Si}}$  formula units.

In the case of interstitials, we obtain:

$$E_f^{I_O} = E_{tot}^{I_O} - \mu_O - E_{tot}^{SiO_2}(N_{Si}) , \quad (4.7)$$

$$\begin{aligned} E_f^{I_{Si}} &= E_{tot}^{I_{Si}} - \mu_{Si} - E_{tot}^{SiO_2}(N_{Si}) \\ &= E_{tot}^{I_{Si}} - \mu_{SiO_2} + 2\mu_O - E_{tot}^{SiO_2}(N_{Si}) . \end{aligned} \quad (4.8)$$

The values we obtain for  $\mu_{Si}$  and  $\mu_O$  in the two limits are included in Table 4.1. The table also includes the values of  $E_f$  in the two limits for all native defects we consider, and Figure 4.17 shows  $E_f$  as a function of  $\mu_O$  over the chemical potential range between the Si-rich and O-rich limits. The results in Table 4.1 show that while oxygen vacancies are

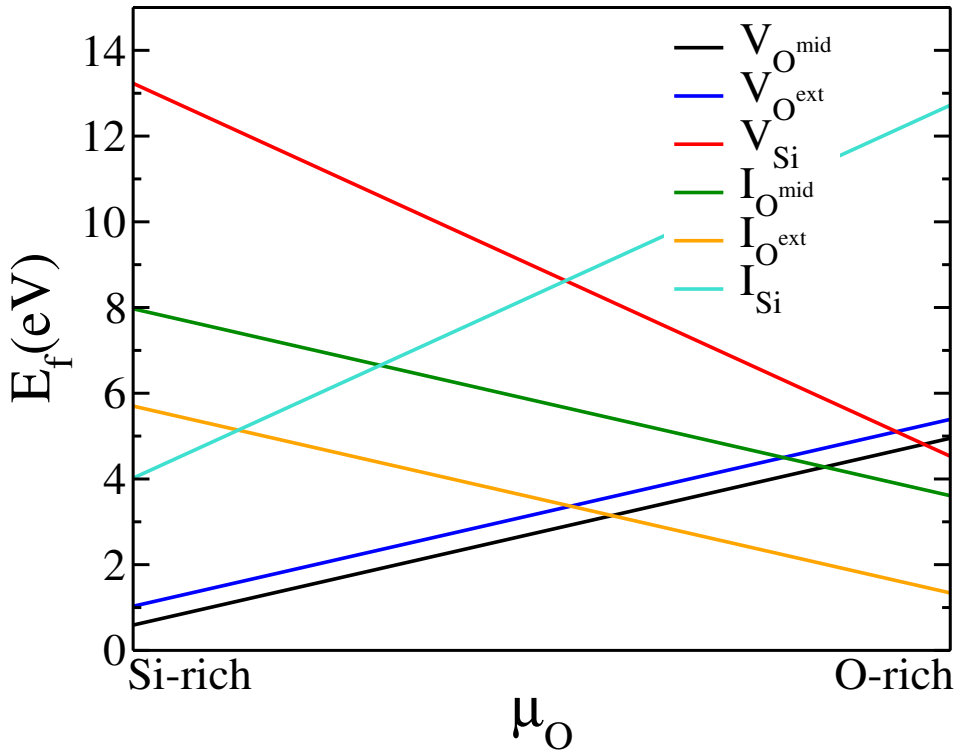


Figure 4.17: Formation energy,  $E_f$ , as a function of the oxygen chemical potential,  $\mu_O$ , for the six defect species considered in this work.  $\mu_O$  values range from a Si-rich value on the left up to an O-rich value on the right, as explained in the text.

more stable in the intermediate layer of O atoms than in the external layers, by 0.44 eV, the opposite is true for the oxygen interstitials, which are much more stable in the external layer, by 2.27 eV, than in the intermediate layer.

Figure 4.17 and Table 4.1 show that the  $V_O^{\text{mid}}$  vacancy is the most stable defect over the first three fifths of the range of chemical potentials we consider, starting from the Si-rich limit, and that the  $I_O^{\text{ext}}$  becomes the most stable defect from there up to the O-rich limit. These trends are expected, since in O-poor conditions we expect higher concentration of O vacancies and in O-rich conditions we expect higher concentrations of O interstitials, but the intervals of chemical potential values where each these two defect species are stable must be determined from the calculations such as presented here. Another non-straightforward

conclusion from our calculations is that in O-rich conditions, hence Si-poor conditions (given the  $\text{SiO}_2$ -bulk thermodynamical constraint on the sum of chemical potentials), O interstitials are more abundant than Si vacancies, and in O-poor conditions, hence Si-rich conditions, O vacancies are more abundant than Si interstitials. Note that in the Si-rich limit of chemical potentials we consider, the  $E_f$  values of the oxygen vacancies are much smaller (by at least 3 eV) than that of the silicon interstitial. Similar considerations apply in the O-rich limit, where  $E_f$  for the  $\text{I}_\text{O}^{\text{ext}}$  interstitial is smaller than  $E_f$  for the silicon vacancy by 4.2 eV.

To summarize, among the single native defects we consider, oxygen native defects are expected to be the most abundant species in thermal equilibrated samples under the synthesis conditions encoded in our choices of chemical potentials.

## 4.5 Partial Conclusions - native defects

In general, native point defects in 2D- $\text{SiO}_2$  introduce in the gap shallow levels strongly localized, and exhibit resonances near to the edge of the bands with a strongly localized nature. Comparing  $\alpha$ -quartz, as a representative of 3D silica crystals, we conclude that this peculiar behaviour is caused by quantum confinement and enhanced Coulomb interactions coming from the 2D nature of the bilayer silica. Despite of many shallow defect levels founded in the vacancies and interstitials studied, only one (in the silicon interstitial) is a truly mass effective state (EMT state), showing a typical more delocalized nature. Additionally, the narrow sub-band at the top of the valence band, as was mentioned above, joint with local distortions at the trapping site and excess of localized charge in a lattice site, suggest the possibility of polaron formation [95,96].

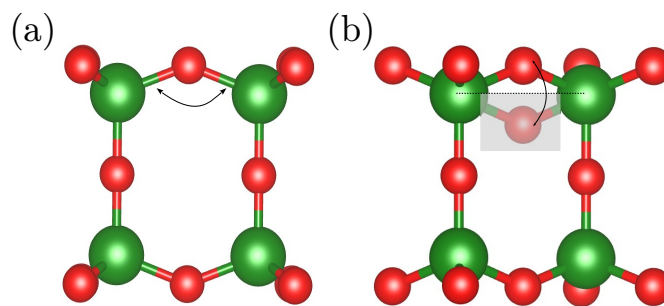


Figure 4.18: Soft modes proposed as the dominant mechanism the 2D- $\text{SiO}_2$  lattice responds to native defects. (a) Scissor mode. (b) Rotation mode.

The mechanical response to native point defects has been in all studied cases, a local deformation, leading the two honeycomb sublattices of Si atoms nearly unaffected by the presence of the defects, except in the very near vicinity of the defect core. We propose the system responds to point defects in a local way driven by two main low-energy structural

excitations of the  $\text{SiO}_2$  lattice, or soft modes present in the Si-O-Si chains: a scissor mode, where the Si-O-Si angle changes; and a rotation mode, where the Si-O-Si bond turns about the minimal distance between silicon atoms (see figure 4.18). It simple fact is believed to be in deeply relation with the anomalous behaviour of 2D silica.

Finally, oxygen monovacancies and single interstitials are found to be amphoteric trapping centers in 2D- $\text{SiO}_2$ , displaying acceptor and donor levels in the fundamental band gap of 2D- $\text{SiO}_2$ . Both silicon native defects we have considered introduce several strongly localized states spanning a large fraction of the gap. The energy of formation of the native defects shows that oxygen vacancies are the most abundant defect species in the thermal equilibrium, for the range of chemical potentials we have considered. The middle layer oxygen vacancy is the most stable defect over the first three-fifths of the range of chemical potentials considered, after this range, the interstitial oxygen appears as the most stable defective configuration until the O-rich limit.

# Chapter 5

## Substitutional impurities

### Introduction

A next step in the study of point defects in a 2D-SiO<sub>2</sub> bilayer silica is to consider the effect of replacing a native species atom by an impurity atom. In order to have a reference and to analyze and compare our results in the case of a 2D-SiO<sub>2</sub> bilayer silica, we consider previous results in the literature for  $\alpha$ -quartz as a representative of 3D-SiO<sub>2</sub>. Aluminium is by far the most typical substitute of Si in quartz [79] and it acts as a deep trapping center, and the "culprit" for the known color of smoky quartz, that can be produced by irradiation of natural or synthetic quartz. [97] Götze et. al. explore in an extensive review several types of dopants already present in varieties of quartz, determining optical emission bands and their correlation with point defects, as follows: a blue emission band ( $\sim 450$  nm - 2.75 eV) associated to oxygen deficiency centers (ODC); a red emission band ( $\sim 620$  - 650 nm - 1.95 - 1.9 eV) showing recombination of electrons in the non-bridging oxygen, with holes in the band gap; a yellow emission band ( $\sim 570$  nm - 2.15 eV) of hydrothermal origin; and finally, a blue emission band at  $\sim 385$  nm (3.15 eV) coming from Al paramagnetic centers. [79]. In the neutral charge state, the Al<sub>Si</sub><sup>0</sup> center traps a hole in one of the nearest-neighbor O atoms that bond to the Al impurity, [79, 89, 98, 99]. Electron paramagnetic resonance (EPR) studies by Nuttall and Weil [100] report also the occurrence of a positively-charged Al<sub>Si</sub><sup>+</sup> center that traps two holes, in a S=1 triplet spin state, on symmetry related oxygen atoms bonded to the Al impurity. While phosphorous and boron are found in lower concentrations in quartz, incorporation as substitutional impurities for Si has been proven in both cases. [79]

In the case of the Al<sub>Si</sub><sup>0</sup>, d' Avezac and collaborators, employing a density-functional-theory (DFT) *ab initio* approach, with a correction for electronic self-interaction effects, have examined the wavefunction of the trapped hole associated with this impurity in  $\alpha$ -quartz. The trapped-hole state was found to be strongly localized on one of the O atoms that bond to the Al impurity, in agreement with EPR evidence. [98, 101, 102] Intrinsic and extrinsic (involving Ge or Li impurities) electron trapping phenomena have also been investigated using *ab initio* methods in  $\alpha$ -quartz and amorphous SiO<sub>2</sub>. [89, 90] Han and *et al.* [103], employing first-principles calculations, conclude that substitutional Al<sub>Si</sub> and P<sub>Si</sub> would be the best candidates

for  $p$ -type and  $n$ -type doping of  $\alpha$ -quartz, respectively, despite the fact that in both cases carrier ionization levels are rather deep in the band gap, 0.86 eV and 0.74 eV, when compared to the room temperature thermal excitation energy of  $\sim 26$  meV, and that both exhibit strongly-localized defect-state wavefunctions that do not show an effective-mass-theory profile, being susceptible to trapping and polaron formation. [89, 90, 96, 98]

One of the consequences of deep defect states is the electron trapping, that has strong effects on the performance of electronic devices that employ  $\text{SiO}_2$  as substrate or gate insulator. It happens, for instance, in  $Ge_{Si}$  impurities in  $\alpha$ -quartz and amorphous  $\text{SiO}_2$ . However, describing the electron and hole trapping, within of framework of DFT is a challenge, due to the self-interaction error. In brief, the electrostatic repulsion between electrons is not exactly cancelled by the exchange and correlation energy, leading to a spurious self-interaction of an electron with itself. As a consequence, the energy of the system in function of the number of electrons appears as a convex function, preferring partial occupations over integer occupations, leading to a delocalized charge density [95]. This problem has been identified and addressed by several authors considering Al impurities in alpha-quartz [89, 97, 101, 102]. Furthermore, DFT interactions can show asymmetry between the behaviour of electrons and holes in point defects [102], in the case of 3D-  $\text{SiO}_2$  the electron trapping is correctly described but it fails to describe holes, DFT predicts a delocalized hole spreaded over the four oxygen neighbors of the  $Al_{Si}$  impurity, but experiments of electron paramagnetic resonance spectroscopy (EPR) shown the Al hole localized at one of the neighboring oxygen [97, 101]. d’Avezac et al. solve this problem while an self corrected interaction (SIC) scheme [104].

As matter of reference it is known that 3D- $\text{SiO}_2$  has a very large band gap of 9.7 eV [13], it leads to consider this inorganic material as an insulator. Although, Han et. al examine the possibility of doping 3D- $\text{SiO}_2$  to become a semiconductor for future ultraviolet optical devices, through systematic first principles calculations in the DFT and DFT+U framework [103]. Taking into account the valence electrons we expect as a general behaviour group III elements (B and Al) would lead to shallow acceptor gap states coming from a free hole; and group V elements (N and P) would lead to shallow donor states, coming from an free electron. According to Han et. al. the best candidate to  $p$ -type doping in 3D- $\text{SiO}_2$  is  $Al_{Si}$  (with an acceptor defect level placed at 0.86 eV above the VBM), and to  $n$ -type doping is  $P_{Si}$  (with a donor defect level placed at 0.74 below the CBM) [103]. In 2D- $\text{SiO}_2$  bilayer silica, due to quantum confinement and enhanced coulombic effects [16, 17], we expect deeper defect levels. Within Kohn-Sham DFT we find to  $Al_{Si}$  a shallower 0.018 eV above the VBM, and in the  $P_{Si}$  case: 2.13 eV below the CBM. The hole state, founded in our 2D material, is a shallow level strongly localized, that can not be considered an effective mass state.

The above examples of shallow levels and resonances with strongly localized wavefunctions motivate us to investigate this issue in the context of doping crystalline 2D- $\text{SiO}_2$  by chemical substitution. Several experimental and theoretical works have addressed the issue of doping of the 3D forms of 2D- $\text{SiO}_2$  with column III and column IV impurities [103].

The discovery of the giant magnetoresistance (GMR) [105] and the modern magnetic tunnel junction device (MTJ) [106, 107] as the building blocks of modern memory multilayer

devices lead to search for 2D materials that can be used as ultrathin electrical insulators between the magnetic layers. The tunneling magnetoresistance (TMR), induced by the insertion of a very thin insulator, results in a higher read-out signal [108] increasing the sensitivity and the density of magnetic information stored by unit of surface. We could think in 2D-SiO<sub>2</sub> as a candidate for the insulating barrier in building ferromagnetic multilayers. 2D silica bilayer has several chemical advantages: high degree of chemical stability; it is the thinnest material with SiO<sub>2</sub> stoichiometry without dangling bonds interacting with the substrate through van der Waals forces; and it is also hydrophobic and shows the highest gap among 2D materials of 6.5 eV [6, 10].

In this work, we examine two cases of column III atoms, aluminum (Al<sub>Si</sub>) and boron (B<sub>Si</sub>) and phosphorous (P<sub>Si</sub>) as an case of column V atoms. All of them, considered as substitutional impurities for a Si atom in the 2D-SiO<sub>2</sub> lattice. Below, we discuss each case separately.

## 5.1 Substitutional Aluminium

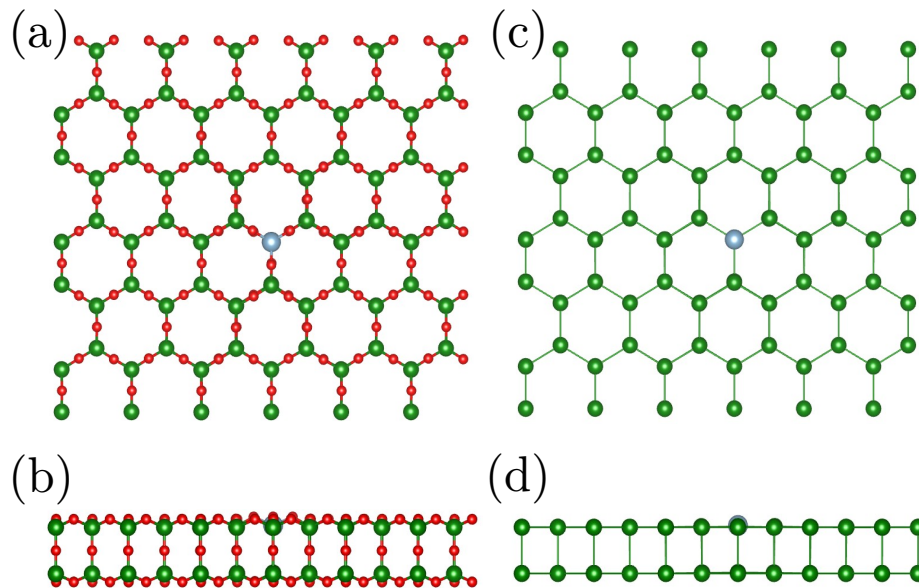


Figure 5.1: Relaxed geometry of the substitutional boron in place of silicon B<sub>Si</sub>. (a) Top and (b) side views. Si (O) atoms are shown as green (red) spheres and B atom is yellow color. (c) Top and (d) side views showing only the Si honeycomb sublattices. In (c) and (d), the two Si atoms that rebond at the defect core are shown as grey spheres, and the lines joining the Si atoms do not represent real bonds, and are drawn to show that the structure of the Si sublattices remain mostly undisturbed.

Aluminium substitutional is one of the group III possible acceptors. Figure 5.5 shows that Al substitutional in the Si place disturbs lightly the lattice. As we have shown in a previous work [109], point defects in 2D silica only changes the lattice locally, and it is a peculiar characteristic of this material, that we think is in relation with the existence of easy modes: scissor and rotation (see fig 4.18). The Al atom push gently away the three



surface oxygen atoms diminishing the pristine angle  $\alpha_{\text{Si-O-Si}}^{\text{ext}}$  from  $139.6^\circ$  to  $135.17^\circ$ . For the sake of clarity the electronic defect-level structure we will consider spin-unpolarized and spin-polarized calculations.

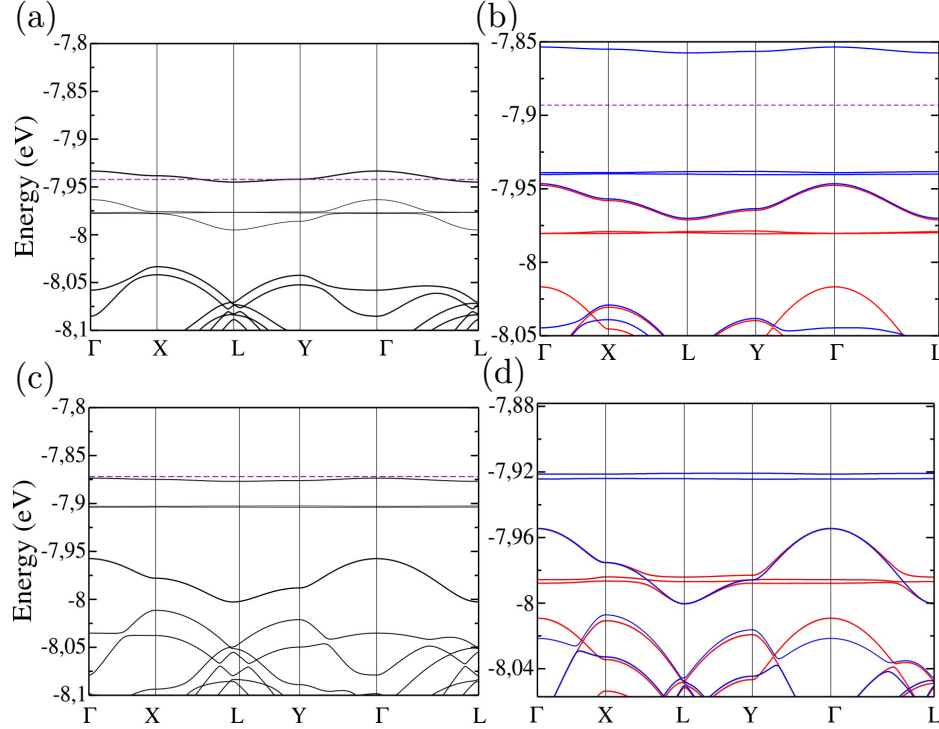


Figure 5.2: Band structure of Al and B substituting Si in 2D-SiO<sub>2</sub> bilayer. The effect of spin polarization is split the EMT state in the aluminium impurity from two plane defect states, while in the B substitutional the EMT state merges with the two states strongly localized. (a) and (b) show gap states near to the valence band induced by Al in the spin-unpolarized and spin-polarized calculation. (c) and (d) show the defect states induced by B in the spin-unpolarized and spin-polarized calculation. Blue line signals minority spin energy levels, and red line indicates majority spin levels.

In a spin-unpolarized calculation (see figure 5.2 a), the Al impurity creates four shallow defect states near to the top of the valence band. One of them is strongly localized and empty located at  $\epsilon_v + 0.12$  eV. Also two states are almost degenerate in energy, located at  $\epsilon_v + 80$  meV, and the last one shows a dispersion characteristic of a truly mass effective state (EMT), located at  $\epsilon_v + 95$  meV (at  $\Gamma$ ). The EMT state shows hybridization with one of the plane states. The charge density shows the degree of localization of each state, signaling the EMT state (see figure 5.3 b).

When the spin polarization is taken in count the EMT state (located at  $\epsilon_v + 70$  meV at  $\Gamma$ ) separates from the almost degenerate plane states located at  $\epsilon_v + 36$  meV, and the spin minority channel stay empty, at  $\epsilon_v + 0.16$  eV, while the 'partner' state go to the valence band leading to a remaining spin polarization of  $1\mu\text{B}$ , as we can see at the figure 5.2 b.

Examining carefully the EMT state we can see some degree of delocalization (figure 5.3 b). Now, examining the spin density, we can appreciate how the Al impurity induces a spin texture, where the minority spin population dominates the surface where the impurity is located, and the majority spin population occupies the middle oxygen and the other surface,

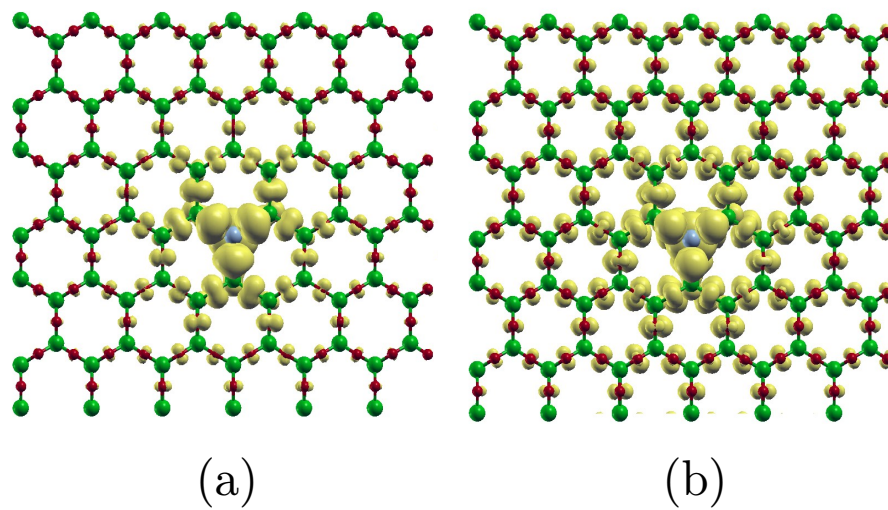


Figure 5.3: Charge density isosurfaces of defect states induced by the Al impurity in the spin-unpolarized regime. (a) Single state (b) hybridization of a truly EMT state and two plane almost degenerate states.

showing two different rates of spatial decaying (see figure 5.4).

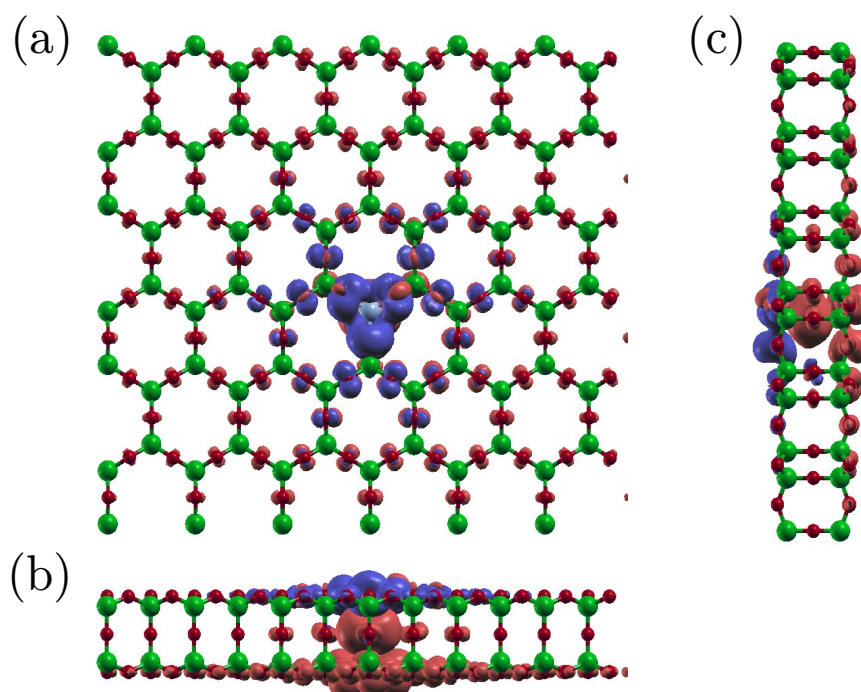


Figure 5.4: Net spin density showing the spin separation induced by Al substitutional on 2D-SiO<sub>2</sub> bilayer. (a) Top view; (b) and (c), side views. Blue color shows the density of the minority spin channel and red shows the density of the majority spin channel.

## 5.2 Substitutional Boron

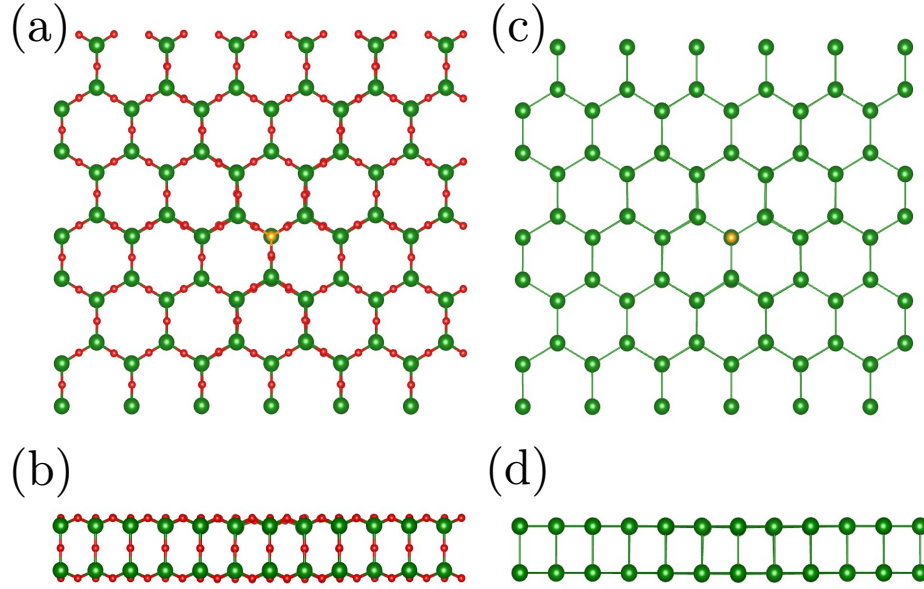


Figure 5.5: Boron substitutional (yellow). Relaxed geometry. (a) Top view;(b) Side view ; (c) Top view (only silicon);(d) Side view (only silicon)

Figure 5.5 shows that when boron substitutes for Si in crystalline 2D-SiO<sub>2</sub>, the symmetry of the lattice is only very mildly disturbed in the neighborhood of the B center, due to B-O bonds that are smaller than the Si-O bonds in the pristine lattice by  $\sim 0.2 \text{ \AA}$ , reflecting the difference in covalent radius between Si and B atoms. Such mild distortions are suggestive of a weak perturbation of the lattice potential-energy function due to the B<sub>Si</sub> impurity, with the concurrent emergence of a shallow EMT defect state. Our calculations, however, show otherwise. In order to understand the defect-level structure associated with the B<sub>Si</sub> (and Al<sub>Si</sub>) impurities, we discuss the results from spin-unpolarized and spin-polarized calculations

Starting with some general observations, we recall that states at the top of the VB are derived entirely from  $2p$  states of O atoms in the external layers, with sizeable contributions from the  $2p$  states of middle-layer O atoms starting deeper in the VB, at 0.5 eV below the top of the VB. In the higher 1.0 eV portion of the VB, Si-atom orbitals give negligible contributions to the band states. This character is mostly inherited by the B<sub>Si</sub> defect states. In particular, orbitals from the substitutional B impurity do not contribute to the defects states.

From a spin-unpolarized calculation, we obtain four shallow defect levels near the top of the valence band, as shown in Fig. 5.2(c), three of which are strongly localized. The shallowest level at  $\epsilon_v + 74 \text{ meV}$  (at the  $\Gamma$  point) is a genuine EMT level, with a wavefunction displaying the characteristic EMT envelope, extending out to  $\sim 15 \text{ \AA}$  from the defect center, as shown in Fig. 5.6(d). Interestingly, this EMT state is nearly entirely derived from the  $p$ -states

of the O atoms in the bottom layer, and shows the same orbital character of the bulk states at the top of the VB. In the neutral state of  $B_{Si}$  this nondegenerate level is fully occupied.

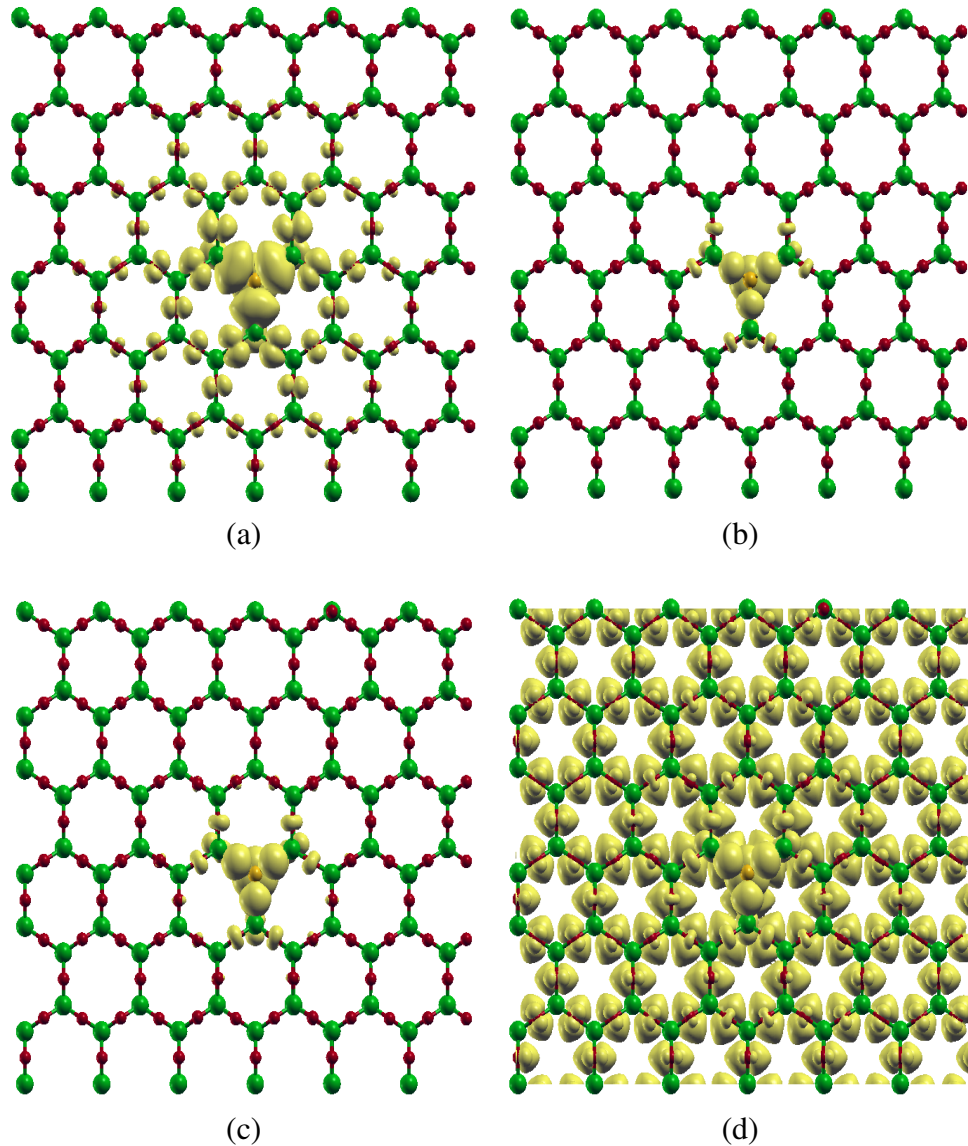


Figure 5.6: Charge density isosurfaces, induced by the boron impurity inside the energy gap, in the spin-unpolarized regime. (a) Localized deep state at  $\epsilon_{vb} + 0.148$  eV (b). (b) and (c) are two strongly localized states almost degenerate, located at  $\epsilon_{vb} + 0.125$  eV and  $\epsilon_{vb} + 0.126$  eV respectively. (d) Truly EMT state showing an extended charge density at  $\epsilon_{vb} + 74$  meV.

The other three defect levels are shallow levels at  $\epsilon_v + 0.125$  eV,  $\epsilon_v + 0.126$  eV, and  $\epsilon_v + 0.148$  eV. The very small splitting of 1 meV between the first two of these levels is within the precision of the DFT calculations, and could be of numerical origin, since the lattice retains enough symmetry (only the additional mirror plane symmetry that coincides with the middle layer of O atoms is absent) about the impurity site to sustain a doubly degenerate level. The spin-polarized calculations and the case of the aluminum impurity that we discuss next, indicate that the splitting is probably not a numerical artifact. The highest nondegenerate level at  $\epsilon_v + 0.148$  eV is partially occupied. The wave functions of these three defect states are very strongly localized on the O atoms in the near vicinity of the  $B_{Si}$ , and are also derived

from Oxygen  $p$  states (see figure 5.6(a),(b),(c)).

In the case of a column III impurity such as  $B_{Si}$  substituting for Si in 3D  $\alpha$ -quartz, previous theoretical studies obtain a single acceptor level with a (0/-) transition state at 1.18 eV above the VB edge. In order to understand the occurrence and occupations of four defects states associated with the neutral  $B_{Si}$  in 2D-SiO<sub>2</sub>, we recall that at 0 K integration of the density of states up to the Fermi level must account for the total number of electrons in the system, so it may appear strange that we find three fully occupied defect states near the top of BV. Charge conservation implies that such a plethora of occupied defect states in the band gap must be accompanied by the presence of antiresonances in the valence bands.

We also expect carrier trapping in the case of the  $B_{Si}$  defect, due to the strongly localized states that are close in energy to the EMT state.

### 5.3 Formation Energy of substitutional impurities

The density of point defects in the thermal equilibrium is controlled by the energy of formation. It is the difference between the energy of a supercell with the defect and the energy of the non-defective bulk supercell, regarding that take off or to insert some atomic specie, is taking in count with the respective chemical potential in order to compare systems with the same number of atoms. In general, to neutral defects, we have:

$$E_f^d = E_{tot}^d - E_{tot}^{bulk} + \sum_i n_i \mu_i; \quad (5.1)$$

where  $E_{tot}^d$  is the total energy of a supercell with defect  $d$ ,  $E_{tot}^{bulk}$  is the total energy of the corresponding (same supercell size) pristine bulk supercell, and  $n_i$  and  $\mu_i$  are the quantities and chemical potentials of the atoms exchanged with the corresponding chemical-potential reservoirs, when the defect is created. In the special case of Al impurity we have:

$$E_f^{AlSi} = (E_{tot}^{AlSi} - \mu_{Al}) - (E_{tot}^{bulk} - \mu_{Si}); \quad (5.2)$$

and, to the B substitutional impurity we have:

$$E_f^{BSi} = (E_{tot}^{BSi} - \mu_B) - (E_{tot}^{bulk} - \mu_{Si}). \quad (5.3)$$

The chemical potentials of native species are determined by the thermodynamical equilibrium condition between the 2D-SiO<sub>2</sub> bilayer and the sources of O and Si atoms. If the oxygen chemical potential is obtained from the diamond-lattice bulk Si, through the thermodynamical equilibrium condition, we have the called Si-rich situation. On the other hand, if the oxygen chemical potential is determined from an O<sub>2</sub> molecular gas, it fixes the silicon chemical potential establishing the O-rich limit to the reaction. The chemical potential to Al was calculated from a aluminium bulk in the standard one atom face-centered-cubic structure, and the chemical potential to B was obtained from a bulk of  $\alpha$ -rhombohedral boron, builded from icosahedral nanocages - 12 atoms unit cell (a more detailed explanation can be found in the

previous section 4.4).

The values we obtain for  $\mu_{\text{Si}}$  and  $\mu_{\text{O}}$  in the two limits and, the values for  $\mu_{\text{Al}}$  and  $\mu_{\text{B}}$  are included in Table 5.1. Formation energies to substitutional Al and B are presented in TABLE 5.1 with previous calculations of native neutral defects previously displayed in table 4.1 and published in [109]. They are presented again for comparison purpose.

Table 5.1: Chemical potentials of silicon, oxygen, aluminium and boron and formation energies of neutral defects in 2D-SiO<sub>2</sub>, for Si-rich and O-rich conditions. Formation energies of native defects were previously calculated. [109]

	Si-rich limit (eV)	O-rich limit (eV)
$\mu_{\text{O}}$	-439.10	-434.74
$\mu_{\text{Si}}$	-245.02	-253.74
$\mu_{\text{Al}}$	<b>-70.62</b>	<b>-70.62</b>
$\mu_{\text{B}}$	<b>-103.79</b>	<b>-103.79</b>
$V_{\text{O}}^{\text{mid}}$	0.59	4.95
$V_{\text{O}}^{\text{ext}}$	1.03	5.39
$V_{\text{Si}}$	13.23	4.53
$I_{\text{O}}^{\text{mid}}$	7.97	3.61
$I_{\text{O}}^{\text{ext}}$	5.70	1.34
$I_{\text{Si}}$	4.02	12.72
$\text{Al}_{\text{Si}}$	<b>-0.23</b>	<b>-8.95</b>
$\text{B}_{\text{Si}}$	<b>1.28</b>	<b>-7.44</b>

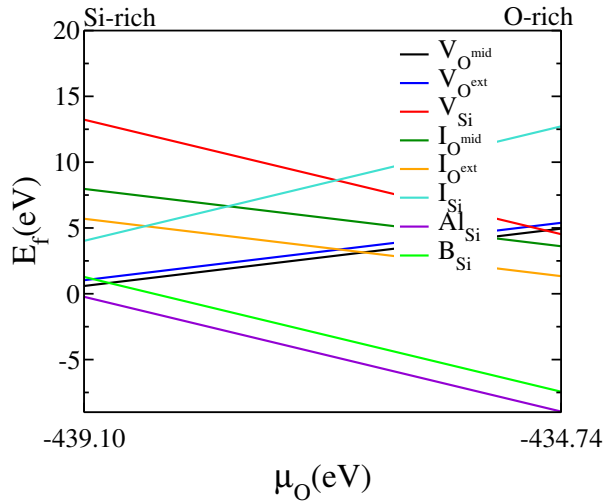


Figure 5.7: Formation energy of neutral defects in 2D silica bilayer as a function of the oxygen chemical potential  $\mu_{\text{O}}$ . Horizontal axis indicate the limit values of  $\mu_{\text{O}}$  for si-rich and O-rich environments.

In comparison with native defects, the formation energies from substitutional impurities have the same order of magnitude of the oxygen vacancies. Also, Al substitutional displays a more stable configuration in all the range of environment presented. Furthermore, in the Si-rich limit of chemical potentials we consider, the oxygen vacancies (at the middle and external) are still the more stable defects, but rapidly in the most of the range the B substitutional shows lower energy.

## 5.4 Partial Conclusions - substitutional impurities

Properties of electronic states induced by group III impurities: Al and B, in 2D silica, within Kohn-Sham DFT frame work are presented. Relaxed geometries from Al and B impurities strengthen our previous adressed conclusions [109]: point defects in this 2D material generate only local geometric perturbations. Both impurities have a defect induced magnetization coming from the energy spin-splitting of defect levels in the gap. Aluminium impurity induces spin separation in the 2D-SiO<sub>2</sub> bilayer, showing different degree of localization to each spin channel, and readjusting the spin population such as we have one spin channel in each 2D-SiO<sub>2</sub> surface. The absence of dangling bonds, chemical stability and wide gap of the ultrathin insulator 2D-SiO<sub>2</sub> suggests the possibility to use the pristine bilayer as tunneling barrier in magnetic multilayer memory devices. The spin separation, induced by the Al impurities in our 2D-SiO<sub>2</sub> silica, could lead to interesting phenomena in magnetic multilayers technology.

## Chapter 6

# Anomalous mechanical response of two-dimensional SiO<sub>2</sub>

### Introduction

The 3D crystalline and glassy forms of silica are brittle materials at room temperature, meaning that they do not undergo plastic deformation upon tensile or shear stresses. There is a vast number of experimental and molecular dynamics (MD) studies of the mechanical properties of 3D-SiO<sub>2</sub>. Results are not always consistent, varying among different studies due to varying experimental conditions and, in the case of MD studies, due to different MD numerical protocols and the use of classical potentials in many of these simulation works.

Another important mechanical property of 2D materials is the bending stiffness, which is the elastic constant that determines the linear-response of the material to bending deformations. In the case of graphene, for example, the bending stiffness can be obtained by studying the scaling of the curvature energy of nanotubes of different diameters, as a function of diameter, and extrapolating to the case of a nanotube of very large radius, with a curvature that is small enough for the response to bending to be linear.

In what follows, we argue that bending of 2D-SiO<sub>2</sub> is anomalous based on the tendency of 2D-SiO<sub>2</sub> high-curvature SiO<sub>2</sub> nanotubes to form kinks and on a quite unexpected nearly degeneracy in energy of several SiO<sub>2</sub> nanotubes of different chiralities and diameters. These kinks are another manifestation of the scissor and rotation modes of O atoms that we discussed in section 4.5 (see figure 4.18).

A stress-strain ( $\sigma \times \varepsilon$ ) relation for  $\alpha$ -quartz, obtained using molecular dynamics with a classical potential in Ref. [110], is shown in Fig.6.1. The top panel shows the curve for three different “samples” in the MD simulations at room temperature. The sudden drop to zero stress at 30% strain signals the fracture (formation of a crack) of the brittle material without the onset of plastic deformation. In the lower panel, effects of temperature are displayed, which amount to a decrease in the strain and stress at the onset of the crack with increasing temperature.

A  $\sigma \times \varepsilon$  curve for silica glass, also from an MD simulation, is shown in Fig. 6.2 (from Ref.



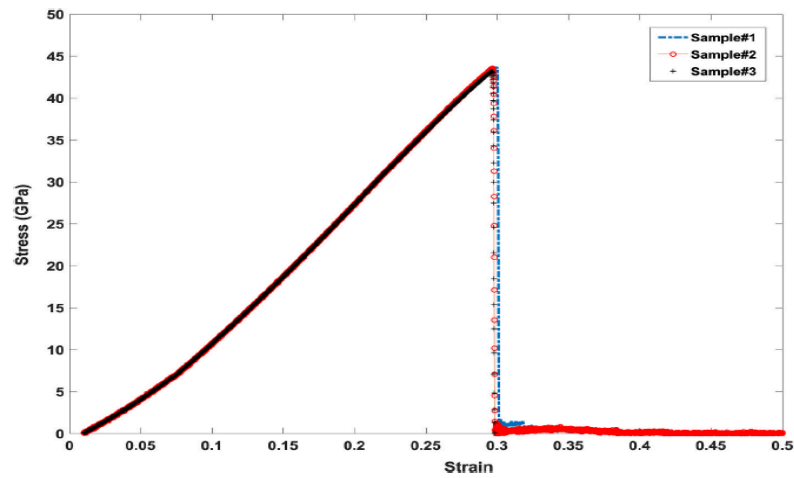


Fig. 7. Stress-strain curves of tensile loading test in the X direction for different sizes at 300 K.

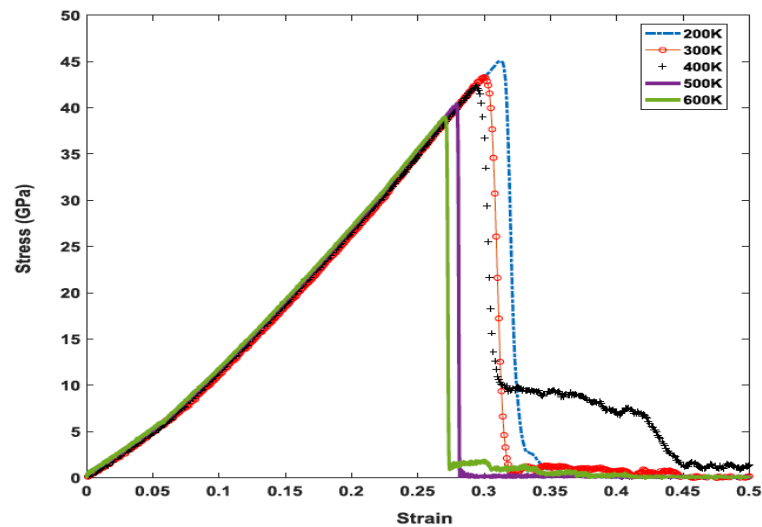


Figure 6.1: Uniaxial tensile stress-strain curves for  $\alpha$ -quartz. Top panel, molecular dynamics simulation of different numerical samples showing the brittle nature of the 3D silica with a critical strain of 30%. Lower panel, the maximum values of stress and strain are reduced when temperature increases. Source: [110].

[18]). The relevant curve in this figure is the continuous one. It shows failure at 30% strain, as in the 300 K curve in Fig. 6.1, but with a stress that is smaller by  $\sim 10$  GPa compared to the  $\alpha$ -quartz failure stress at the same temperature. Several different works on the mechanical properties of crystalline and glassy or amorphous forms of 3D-SiO<sub>2</sub> present similar stress x strain relations.

In the context of the results for the mechanical response of 2D-SiO<sub>2</sub>, that we discuss next, we call attention to the following features of the  $\sigma \times \varepsilon$  relations in Fig. 6.1: (i) the occurrence

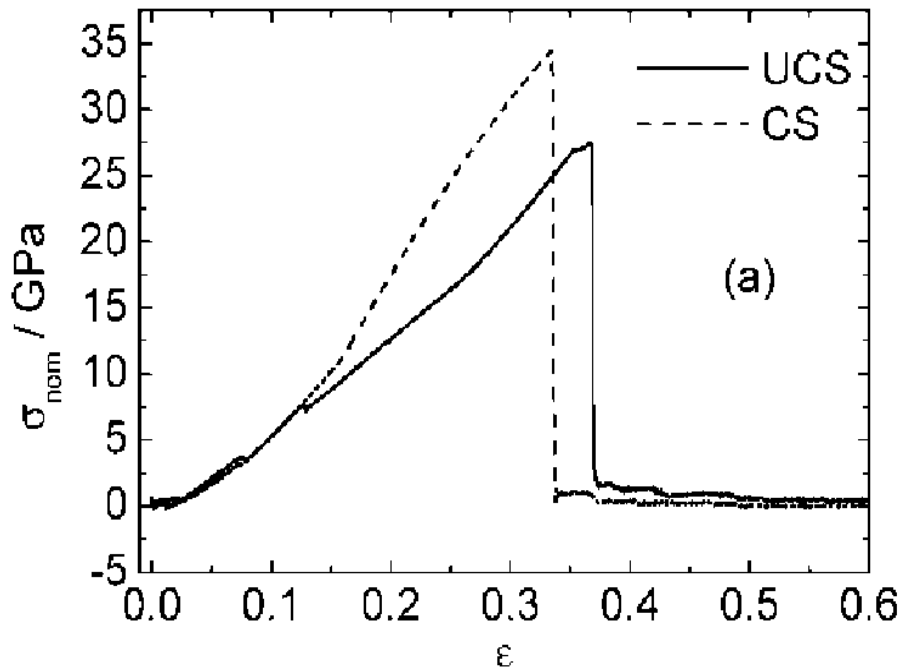


Figure 6.2: Stress-strain curve for silica glass (amorphous-cristobalite) strained along the [001] direction in which the [100] directions and [010] directions were constrained to initial values (dashed line) or free to relax (solid line). Source: [18].

of two linear regimes of elastic deformation, a first one at small strains  $0 \leq \varepsilon \leq 7\%$ , and a second one with a larger stiffness (the inclination of the  $\sigma \times \varepsilon$  curve) that extends from about 8% strain up to the breaking point at  $\sim 30\%$  strain. Moreover, as already mentioned above, no plastic deformation is observed.

## 6.1 The structural ground state of 2D-SiO<sub>2</sub>: methodological issues

Before addressing the response of 2D-SiO<sub>2</sub> to bending and uniaxial tensile strains, we present here a discussion on the structural ground state of this material. In all, but one geometry figures in this section, the plane of the layers is the  $xy$  plane, the armchair direction is along the  $x$ -axis and the zigzag direction is along the  $y$ -axis. The one exception is the auxetic structure we describe below, which lattice is not honeycomb as the other ones.

Figure 6.3(a) shows a top view of the structure that is proposed as the equilibrium geometry of a 2D-SiO<sub>2</sub> bilayer in the experimental works [6, 111]. In this geometry, which we label G1, an oxygen atom from an external layer appears, on projection, as making a straight line with the two Si atoms it is connected to. We recall that in both external layers, the O-atom sublayer is 0.58 Å above (below) the plane formed by the Si atoms. Thus, it is the projected position of the O atom onto the plane of the Si sublayer that is aligned with the Si atoms.

Figures 6.4(a) and 6.5(a), show top views of two alternative structures we have identified

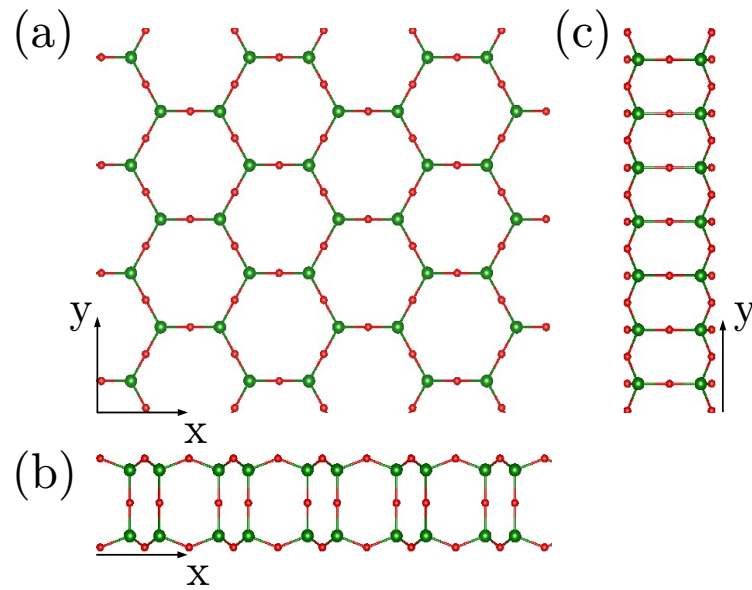


Figure 6.3: Experimental equilibrium geometry of 2D SiO<sub>2</sub>, characterized by stright Si-O-Si bonds (labeled G1 geometry). (a)Top view. (b) Front and (c) side views.

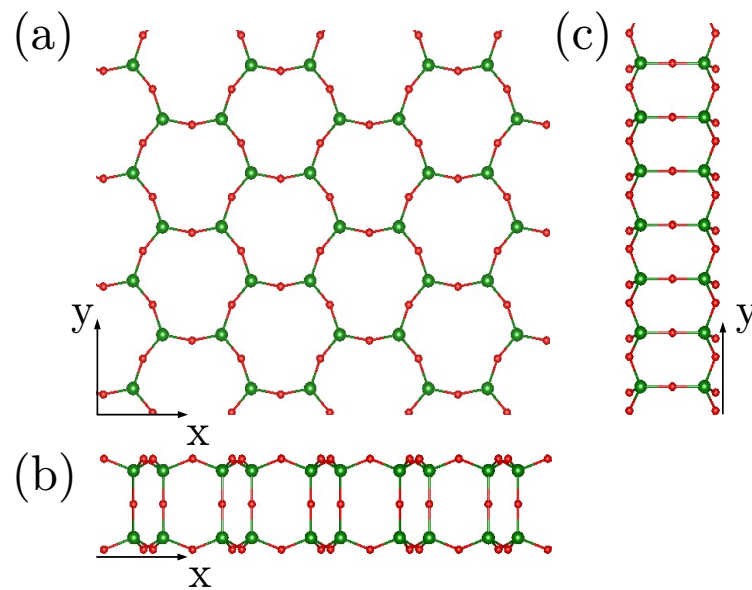


Figure 6.4: Equilibrium geometry of SiO<sub>2</sub>, characterized by "puckered" Si-O-Si bondings (labeled G2). (a)Top view. (b) front and (c) side views.

in our calculations, where the projected positions of the O atoms are not aligned with the two Si atoms. We label these as G2 and G3, respectively. The two geometries are related by a 60° rotation of the “bottom” external layer with respect to the “top” external layer, but the transformation leading from the geometry in Fig. 6.4 to the one in Fig. 6.5 is a rotation of the oxygens in one of the layers. More specifically, note that in Fig. 6.4(a), if we take one of the Si-atom hexagons in the top layer as a reference, the six O atoms along the hexagon edges alternate on inwards and outwards positions, and the O atoms on the bottom layer follow the

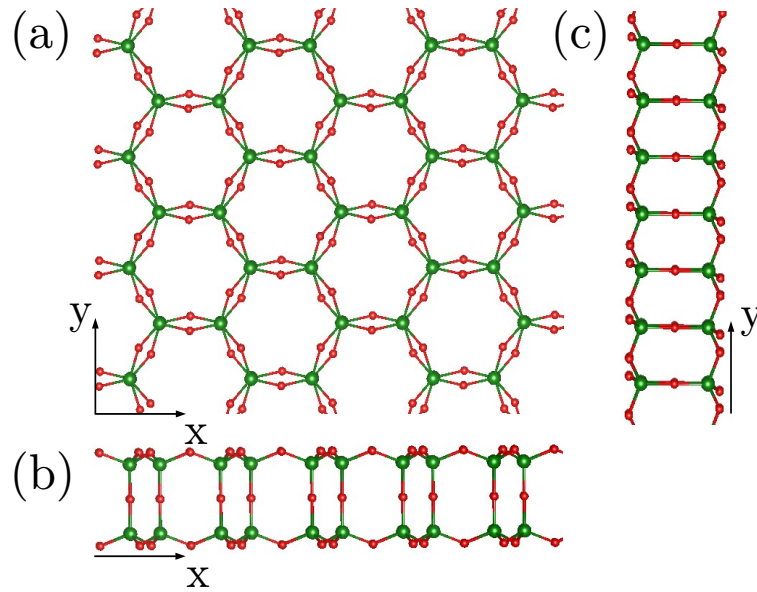


Figure 6.5: Equilibrium geometry of SiO<sub>2</sub>, characterized by alternating up and down "puckered" Si-O-Si bondings (labeled G3). (a) Top view. (b) front and (c) side views.

same pattern. In the G3 geometry in Fig. 6.5(a), the oxygen atoms on the bottom layer rotate around the axis joining the two Si atoms it connects, such that O atoms in the bottom layer, originally in a inward position are now in a outward position, and vice versa.

In our highly-converged calculations employing the SIESTA code, with 8x8x1 k-point grids, and a MeshCutoff of 700 Ry, the G2 and G3 geometries are degenerate equilibrium geometries, with a lattice constant of 5.27 Å. The STM experimental work in Ref. [6, 111], authors conclude that the G1 structure is the equilibrium geometry, with a lattice constant of 5.42 Å. When using the VASP and QE codes with, we obtain G1 as the equilibrium geometry, with a lattice constant of 5.31 Å and 5.30 Å respectively. The cohesion energy of the three structures, G1, G2, and G3 differ by only a few meV per atom. Specifically, in the VASP code we have a 10x10x1 k-points grid and a energy cutoff (ENCUT) of 500 eV, and in the QE code we have also a 10x10x1 k-points grid and a energy cutoff of 55 Ry (~750 eV).

Table 6.1: Comparison between G1 and G2 geometries using several codes. SIESTA code preserves the initial geometry. VASP and QE codes give as final relaxed geometry the straight Si-O-Si bonds characteristic of G1 geometry. The "puckered" Si-O-Si bonds or G2 geometry has lower energy.

Software	Ecut	Kpoints grid	Energy (eV)	Inp/Out Geometry	PP
SIESTA	400 Ry	64x64x1	-4492.86 eV	G1/G1	PBE-GGA
SIESTA	400 Ry	64x64x1	-4492.91 eV	G2/G2	PBE-GGA
VASP	500 eV	10x10x1	-94.7986 eV	G1/G1	PBE-PAW
VASP	500 eV	10x10x1	-94.7849 eV	G2/G1	PBE-PAW
QE	55 Ry	10x10x1	-521.5220 Ry	G1/G1	PBE-PAW
QE	55 Ry	10x10x1	-521.5219 Ry	G2/G1	PBE-PAW

Also using the SIESTA, VASP and QE codes (see Table 6.1), we did a comparison be-

tween final geometries as a function of the initial geometry. In the SIESTA code, if the initial positions were in a G2 geometry ("puckered" Si-O-Si bonds), the final geometry will be also a G2 geometry; and if the initial geometry were of type G1 ("stright" Si-O-Si bonds), the final Geometry will be also a G1 geometry. The energy difference between this two structures is 0.0125 meV per SiO<sub>2</sub> unit, approximately one half of the thermal fluctuation energy at room temperature. The "puckered" geometry (G2) show less energy that the "stright" geometry (G1). In the VASP and QE code the final relaxed geometry is always G1 type, regardless of the initial configuration.

Thus, there is an inconsistency between plane wave (VASP, QE) and localized orbitals (SIESTA) codes, which may be related to the different basis functions and/or the pseudopotentials employed in the two calculations. The SIESTA code employs an atomic-orbital basis and norm-conserving pseudopotentials, and no systematic procedure for convergence with respect to the basis function is available. The VASP and QE codes employ PAW pseudopotentials, which are more adequate to treat hard-core atoms such as oxygen, and a plane-wave basis which allows for systematic convergence.

Table 6.2: Comparison between DZP and TZP basis in SIESTA code. The TZP basis leads to a more "straight" Si-O-Si bonds as can see in figure 6.6.

Software	Basis	Ecut	Kpoints grid	Energy (eV)	Inp/Out Geometry	PP
SIESTA	DZP	400 Ry	64x64x1	-4492.91 eV	G2/G2	PBE-GGA
SIESTA	TZP	400 Ry	64x64x1	-4495.58 eV	G2/G2	PBE-GGA

This suspect was tested by highly converged calculations made in SIESTA code (see Table 6.2), also with a Meshcutoff of 400 Ry, and a very dense kpoints-grid of 64x64x1. In this case we take a type G2 structure (puckered bonds Si-O-Si) as initial geometry, but we compare the results between a double polarized basis (DZP or standard SIESTA basis) and a triple zeta polarized basis (TZP). The DZP basis provides 13 basis function per atom, and the TZP furnishes 17 basis functions by atom. The TZP basis results in more 'straight' bonds in comparison with the DZP basis (see figure 6.6), indicating that the inconsistency may be due to the lack of completeness of the atom-centered orbitals.

We remark, however, that if we apply a biaxial tensile strain of 2.5% or larger to both the G2 and G3 geometries, and perform SIESTA calculations for these strained geometries, they transform onto the G1 geometry. We are currently investigating this methodological issue in more detail, but it is safe to conclude that most likely the G1 geometry is the equilibrium geometry, and the G2 and G3 should be the stable geometry for small compressive strains of -2.5% or larger (in magnitude).

Besides the G1, G2, and G3 geometries, in the course of the quasistatic calculations, for the response of the 2D-SiO<sub>2</sub> bilayer to an uniaxial tensile strain, we describe in the following, we identified a transformation, under a quasistatic strain of 36%, to the geometry shown in Fig. 6.7. This is precisely the  $\beta$ -2D auxetic silica structure obtained in the work of Gao and collaborators [112] using an evolutionary algorithm.

In our SIESTA calculations, the total energy of the  $\beta$ -2D-SiO<sub>2</sub> is only 30 meV per atom

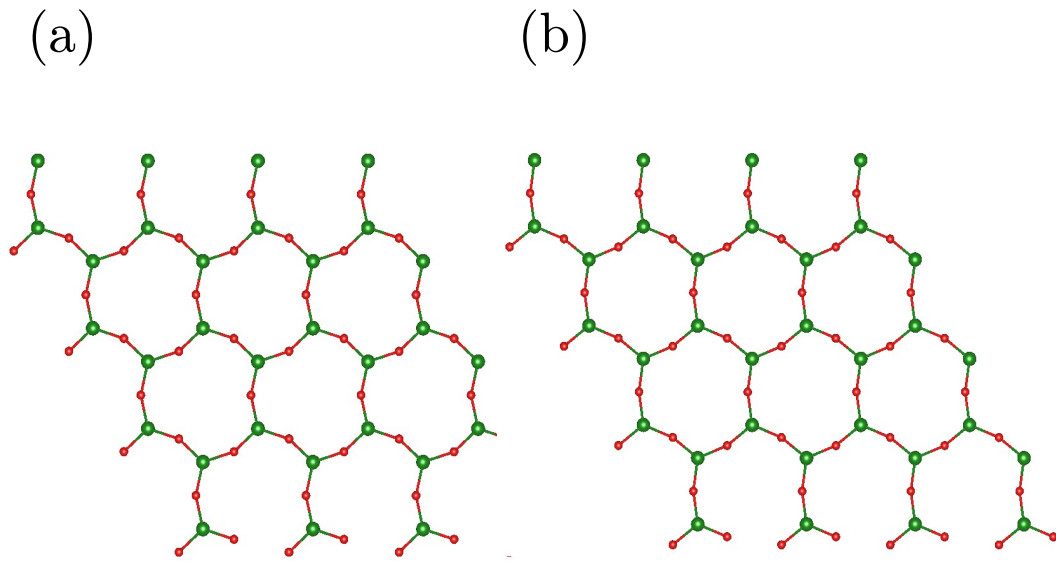


Figure 6.6: Top view of relaxed geometries of 2D SiO<sub>2</sub>, using two basis:(a)DZP and (b)TZP. It can be seen the TZP basis 'straighten out' more the Si-O-Si bondings.

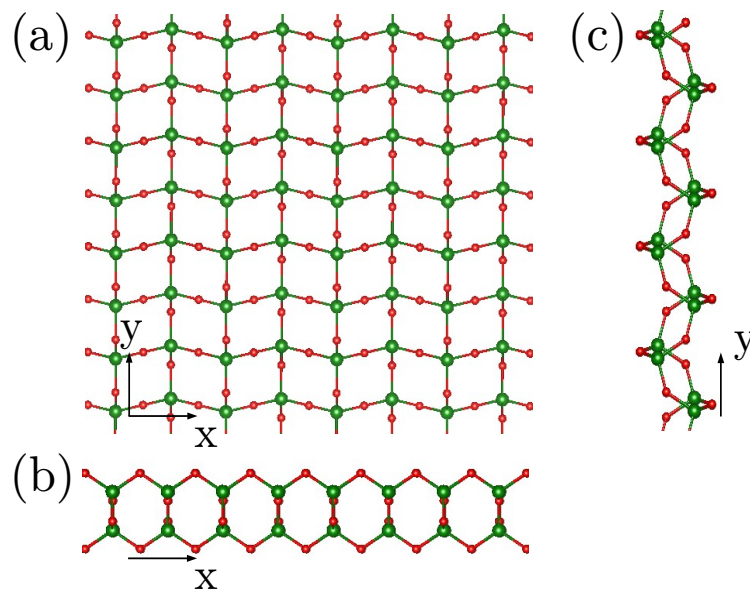


Figure 6.7: Equilibrium geometry of SiO<sub>2</sub> ( $\beta$ -2D silica), characterized by a "squared" top view.(a)Top view. (b) front and (c) side views.

higher than that of the SIESTA ground-state (G2 e G3) geometries. Gao *et al.* report a  $\beta$ -2D-SiO<sub>2</sub> energy that is 70 meV higher than that of the G1 geometry. The difference is probably related to the methodological issues discussed above. At any rate, the energy difference between the  $\beta$ -2D-SiO<sub>2</sub> and the G1, G2, and G3 geometries is of the order of the thermal fluctuation energy per atom at room temperature.

For the sake of completeness, we report also another structure that we obtained at even larger strains in our tensile-strain numerical simulations, shown in Fig. 6.8. This geometry

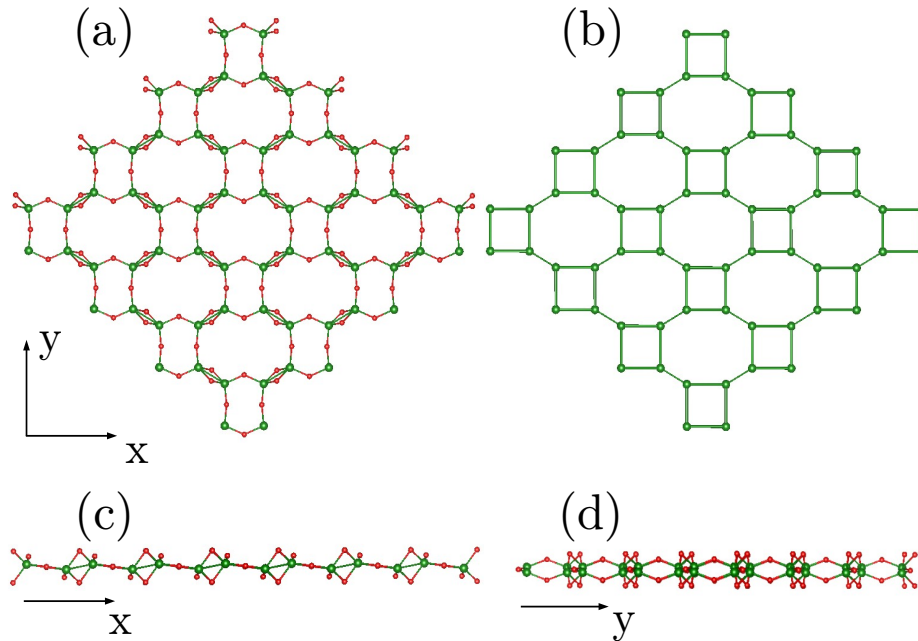


Figure 6.8: Equilibrium geometry of SiO<sub>2</sub>, reached to high tensile strain (labeled tetraoctite-2D silica). (a) Top view. (b) Only Si atoms top view. (c) frontal and (d) side views. Most of the green bonds between Si atoms in (b) are fictitious, but allow to appreciate clearly the 4-8 geometric pattern.

resulted from the relaxation of a highly-strained bilayer 2D-SiO<sub>2</sub> structure. The side views in the bottom panels show that relaxation has transformed the highly-strained 2D-SiO<sub>2</sub> bilayer into essentially a puckered monolayer. The scissor and rotation modes of the oxygen atoms, that we alluded to in the introduction of our paper [109] (or more explicitly in the section 4.5, figure 4.18), have driven the transformation.

In the top panel on the right (FIG. 6.8), we show only the Si atoms in this geometry. Most of the “bonds” shown in this figure are not really bonds (much longer than a Si-Si bond) but lines that were drawn to show the tetraoctite nature of this geometry. We observe that this is very similar to the so-called tetraoctite tiling of the plane, a geometry that has been considered as an alternative graphene structure and the motif of a fourfold plus an eightfold ring has been considered as a grain boundary in graphene and two-dimensional boron nitride [113, 114]. This tetraoctite structure is 0.21 eV per atom higher in energy than the G1, G2, and G3 geometries.

## 6.2 Anomalous response of 2D-SiO<sub>2</sub> to bending deformations

In order to obtain the bending stiffness of 2D-SiO<sub>2</sub>, we built several nanotubes of different chiralities and diameters, by rolling up a 2D-SiO<sub>2</sub> bilayer. These structures were fully relaxed, using the Siesta code. A DZP basis, with MeshCutoffs (MC) of 250 Ry, were employed in these calculations. For the majority of the nanotube structures we consider, relaxation with

larger cutoffs of  $MC = 350$  or  $450$  Ry were also performed, and these have shown rather small changes in the energy of the tubes. So, results with  $MC = 250$  Ry are already converged.

We performed two relaxation protocols: (i) in the first case we performed an initial relaxation with a small cutoff,  $MC = 150$  Ry, and a single-zeta basis (SZ), and then the resulting structure was further relaxed with  $MC = 250-450$  Ry and a DZP basis; (ii) in the second case, we relaxed the initial structure directly with DZP and  $MC = 250-450$  Ry, without a previous relaxation. This has led to more than one relaxed geometry for each nanotube.

Furthermore, we have observed a tendency for the formation of kinks in the nanotubes, as discussed in more detail below, specially in nanotubes with smaller radii, hence larger surface curvatures. For that reason, we have attempted to modify the initial structure of some of the nanotubes with larger radii (smaller curvatures) in attempts to induce the formation of such kinks. This was done by flattening the initial geometry of the tubes, such that they show an elliptical cross section, and in some cases a kink was also introduced by hand on the flattened geometry. These procedures have also led to the formation of new metastable nanotube geometries in some cases, as discussed in the following.

The resulting relaxed structures of the  $(n,0)$  zigzag (ZZ) tubes are shown in Fig. 6.9, and Figs. 6.10- 6.11 show the structures of the  $(n,n)$  armchair (AC) nanotubes. The three rightmost panels in the lower line in Fig. 6.11 show three nanotubes of mixed chiralities (MC):  $(n,m) = (10,4)$ ,  $(12,3)$ , and  $(16,4)$ .

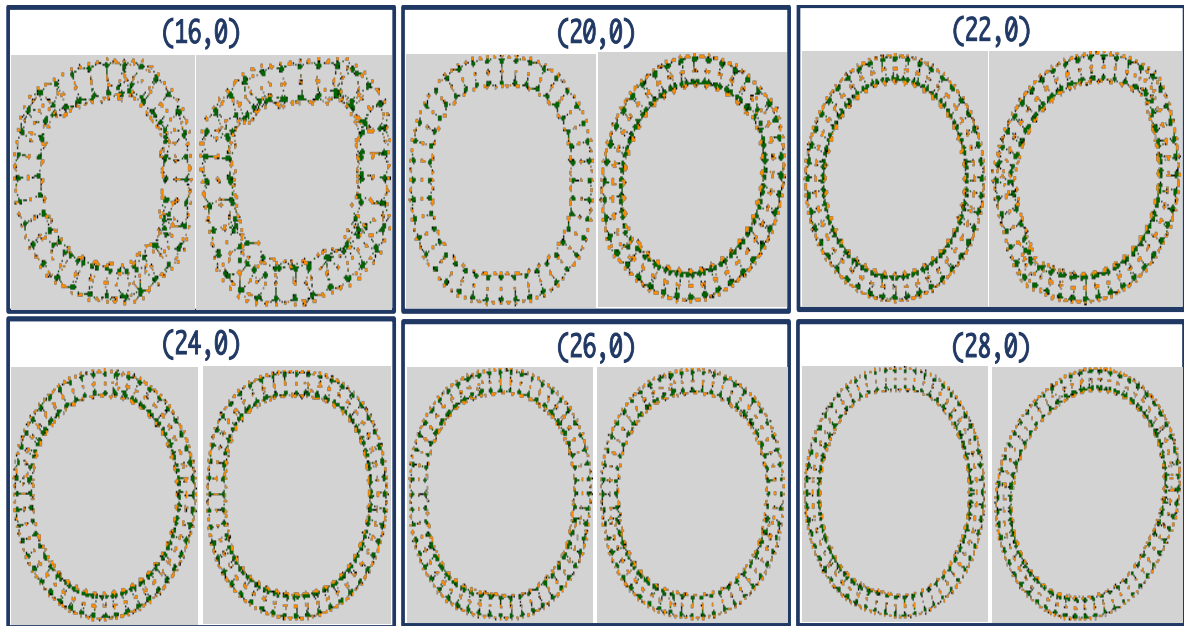


Figure 6.9: Relaxed geometries of 2D-SiO<sub>2</sub> nanotubes, zigzag (ZZ) quirkality  $(n,0)$ . The picture shows the occurrence of different final configurations to the same quirkality. Some of them are characterized by the formation of kinks and plane regions to reduce the final energy.

As can be observed in the figures, our different numerical protocols have produced several different metastable morphologies for AC, ZZ, and mixed-chirality tubes. We observe more than one kink morphology, in these different nanotube morphologies, particularly so for tubes



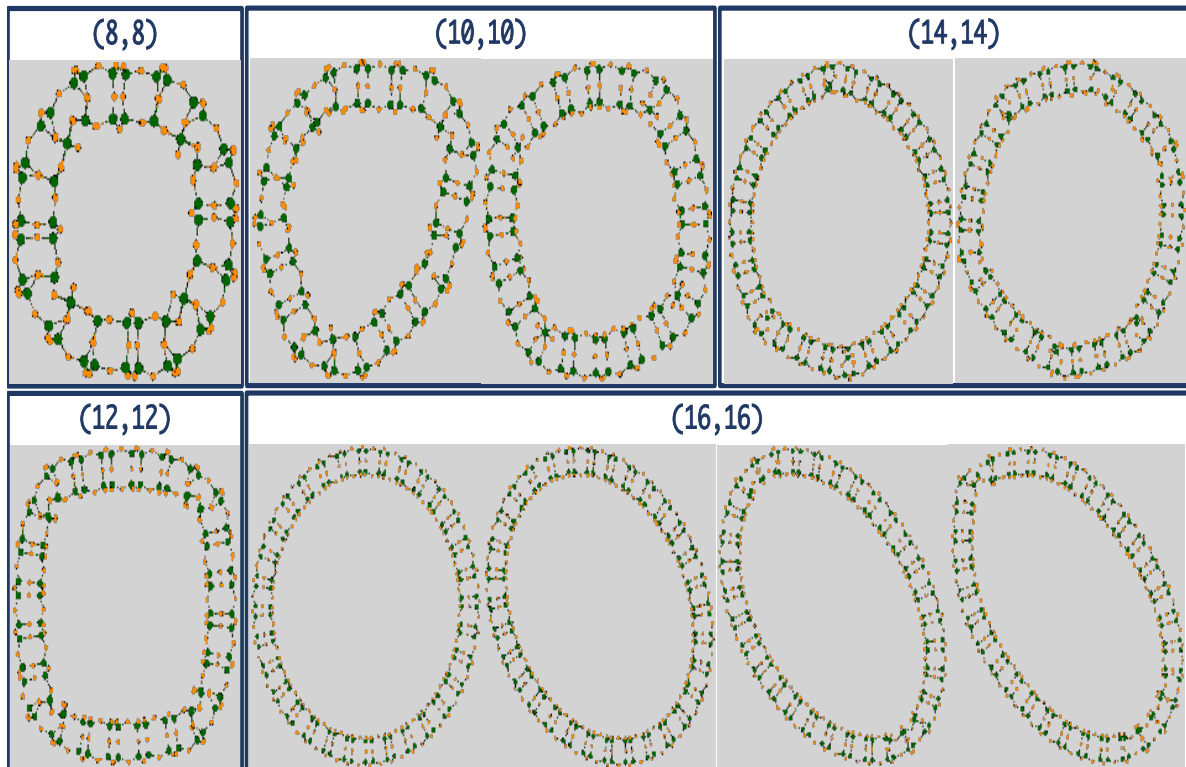


Figure 6.10: Relaxed geometries of 2D-SiO<sub>2</sub> nanotubes, arm-chair (AC) chirality (n,n). The (12,12) nanotube shows an almost square morphology with one kink at each vertex: introduction of kinks has very small energy cost. The nanotubes find various compromises between a curved surface and a kinked one.

with smaller radii. In particular, the process of inducing kink formation by flattening the nanotube cross section and/or imposing a kink in the structure by hand, have led to three different morphologies in the case of (16,16) AC tubes, in addition to the circular-cross-section tube.

The case of the (12,12) AC nanotube is a telling one: this tube shows an almost square morphology, with one kink at each vertex. It is clear from this example that when a 2D-SiO<sub>2</sub> bilayer is rolled up to form a tube, formation of these kinks allow the tube to maintain large almost flat portions that entail very small energy cost with respect to the flat bilayer. Overall, it appears that the tubes find various compromises between a curved surface and a kinked one, due to the small energy cost of the kinks in this system.

The formation of these kinks is driven by the structural “easy modes” involving rotation and scissor displacements of the oxygen atoms. In the higher curvature tubes, it appears that the kinks form spontaneously, without an energy barrier. As the tube diameter increases, the curvature decreases, and it appears that kink formation becomes an activated process. We expect this process to be one that involves small barriers, given the very small energy barriers involved in the rotation and scissor modes of “structural excitations” in this system. This hypothesis will be tested in the near future by means of *ab initio* molecular dynamics simulations.

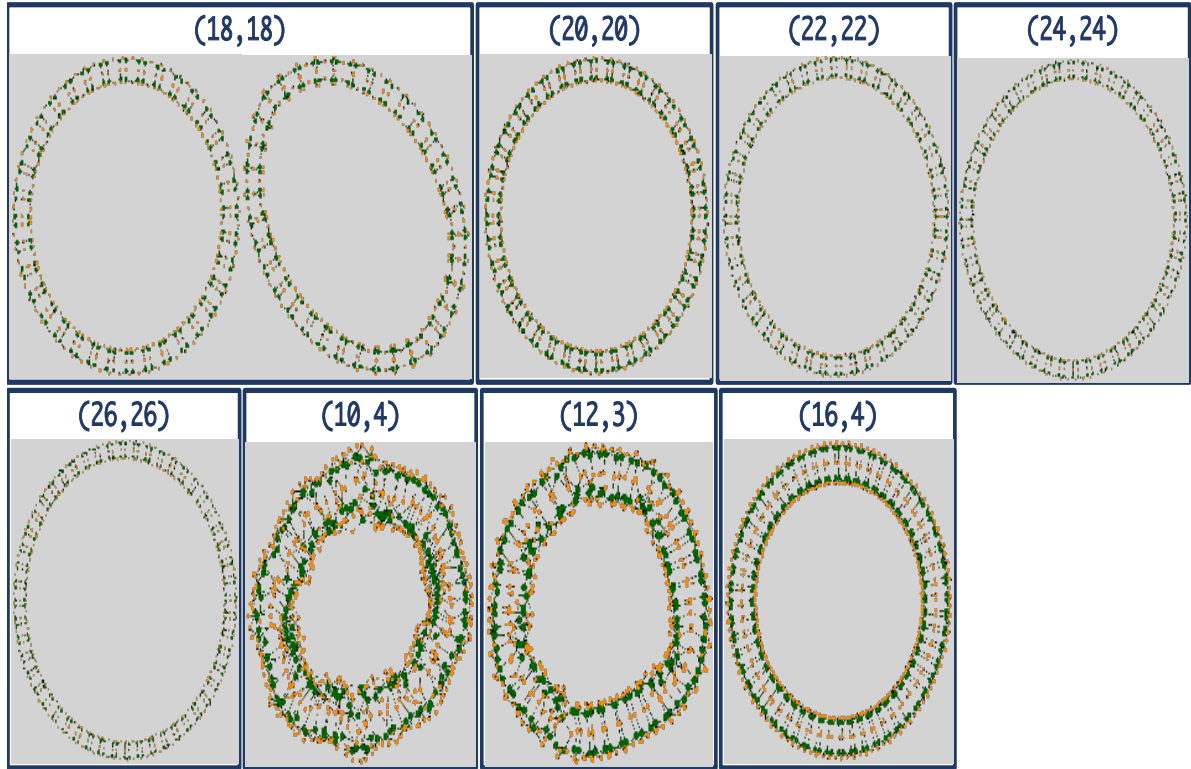


Figure 6.11: Relaxed geometries of 2D-SiO<sub>2</sub> nanotubes, some of them with mixed quirkality (n,m). Low radius nanotubes show a tendency to 'amorphize' to reduce the final energy. Small radii nanotubes are prone to form kinks spontaneously (without an energy barrier).

We now argue that kink formation may render the response to bending anomalous in 2D-SiO<sub>2</sub>, as follows. Figure 6.12 shows the total energy per formula unit of the tubes as a function of the radius. For comparison, the lower panel shows the energy of carbon nanotubes as a function of radius, from Ref. [115]. The red line in the upper panel shows the energy per formula unit of the flat 2D-SiO<sub>2</sub> bilayer, which is the limiting energy as the nanotube radius tends to infinity.

Note that the energy of all 32 2D-SiO<sub>2</sub> nanotubes in our study fall within a very small interval of  $\sim 0.360$  eV per formula unit, i.e., 0.120 eV per atom. Moreover, the energies for different morphologies of the same tube [same (n,m) indices] differ by less than the thermal fluctuation energy per atom at room temperature ( $\frac{3kT}{2} = 0.04$  eV).

In comparison with the case of the carbon nanotubes in the lower panel, the energy versus radius curves for the SiO<sub>2</sub> tubes is not smooth, and differs substantially in the behavior at small radius, where the energies of the carbon nanotube tend to large values due to the large uniform curvature of a small-radius carbon nanotube. In the SiO<sub>2</sub>, this energy divergence at small radius is avoided by the formation of the low-energy kinks. Furthermore, the presence of various different morphologies for each tube is absent in the case of carbon nanotubes.

The bending rigidity of 2D-SiO<sub>2</sub> has been measured in Ref. [116] through inelastic helium atom scattering (HAS). The authors report a value of  $\kappa = 8.8 \pm 0.5$  eV. The main idea of the inelastic helium atom scattering (HAS) is to bombard the elastic surface of the material

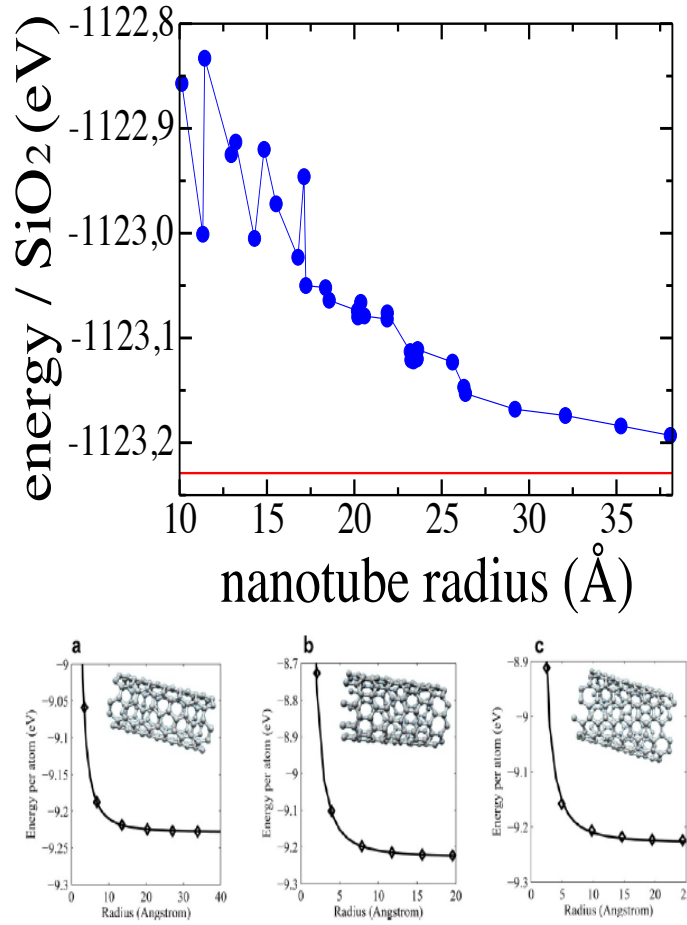


Figure 6.12: Upper Panel: Total energy per SiO<sub>2</sub> unit of 2D-SiO<sub>2</sub> nanotubes, as a function of nanotube radius. The red line signals the energy per unit of the flat 2D-SiO<sub>2</sub> bilayer. In the lower panel, to purpose of comparison, total energy per atom versus the radius of single-wall carbon nanotubes with different rolling up directions. The presence of different geometries associated to the same nanotube are absent. Source of the lower panel: [115]

with helium atoms exciting transversal vibrations of the 2D layer, measuring the change of momentum experienced by the helium atoms we can get the bending rigidity. This technique is well suited to investigate mechanical properties of fragile insulating materials, because the low energy of helium atoms assures that only the surfacial atomic layer interacts with the low energy He atoms, also without sample damage. Additionally, it prevents deeper interactions with the substract, doing a mapping of the topmost surface layer. In Fig. 6.12 we plot the formation energy  $E_f$  of SiO<sub>2</sub> nanotube as a function of  $1/R^2$ , where  $R$  is the tube radius.

In Ref. [115], the authors use the following parameterization for the energy of per atom of the carbon nanotubes:

$$E = E_0 + \frac{S_0 \kappa}{2R^2} ; \quad (6.1)$$

where  $E_0$  is the energy of the flat layer,  $S_0$  is the area per atom of graphene, and  $\kappa$  is the bending rigidity.

In Fig. 6.13, we plot the formation energy per formula unit of the SiO<sub>2</sub> tubes, and the red

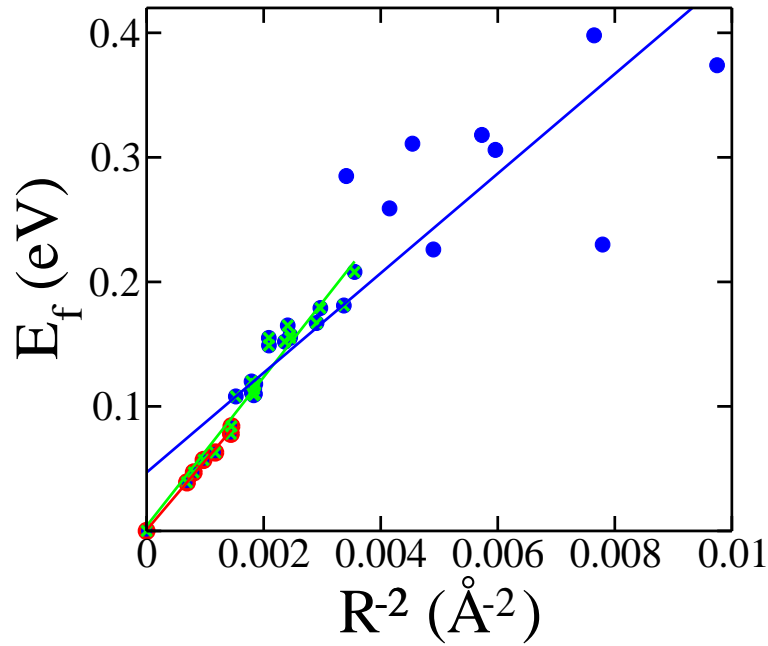


Figure 6.13: Total energy of 2D-SiO<sub>2</sub> nanotubes, as a function of the curvature radius ( $\frac{1}{R^2}$ ). The red line indicates the energy per SiO<sub>2</sub> unit corresponding to the flat SiO<sub>2</sub> bilayer. Red circles signals the first seven nanotubes with larger radii, and with more circular cross section, leading to a bending rigidity  $\kappa=18.5$  eV. Green crosses indicates 24 nanotubes with larger radii and less scattered energies, leading to a bending stiffness  $\kappa=18.5$ . Finally, a fitting of all nanotubes leads to a bending rigidity value of  $\kappa=13.31$  eV.

line shows the energy per formula unit of the flat SiO<sub>2</sub> bilayer. The formation energy is the excess energy of the nanotube with respect to the flat bilayer. We use the area per formula unit of the bilayer ( $S_0 = 6.01 \text{ \AA}^2$ ) and fit the energy by Eq. 6.1 above to obtain the bending rigidity of 2D-SiO<sub>2</sub>.

We computed three different fittings of the numerical data in Fig. 6.13: in the first one we fit only the energies of the seven nanotubes with larger radii (shown as red circles in the figure), that show a more circular cross section. This yields  $\kappa = 18.5$  eV. A second fitting considers only 24 nanotubes with larger radii ( $R^{-2} < 0.004 \text{ \AA}^{-2}$ ) and less scattered energies, shown by green crosses in the figure. This yields a value  $\kappa = 18.5$  eV. A fitting of all 32 nanotubes produces  $\kappa = 13.31$  eV, but it is quite clear from the figure that no straight line fits well the scatter of energy values of all tubes.

Therefore, our more reliable theoretical results are about twice as large as the experimental results. We conclude this section by speculating that interactions with the substrate may reduce or eliminate the likely existing barrier for kink formation in the flat SiO<sub>2</sub> layer, and the response to bending of the bilayer, even in the linear regime, may not follow the usual quadratic behavior of the energy with curvature and 2D-SiO<sub>2</sub> may show anomalous bending behavior. This would be the reason for the discrepancy between the experimental and theoretical values of the bending stiffness.

### 6.3 Response of 2D-SiO<sub>2</sub> to quasi-static(QS) tensile uniaxial strain

We have also performed numerical *ab initio* simulations for the response of 2D-SiO<sub>2</sub> to a quasi-static(QS) uniaxial tensile strain, in the armchair and zigzag directions of the SiO<sub>2</sub> bilayer. The protocol for these simulation is as follows: we apply strain increments of 1%, starting from the equilibrium geometry. At each step, we allow the bilayer to relax in the direction perpendicular to the applied strain. In this way, the system is allowed to fully relax under the constraint of the applied strain. In the next step, the 1% increase in strain is applied to the strained-equilibrium geometry obtained in the previous step.

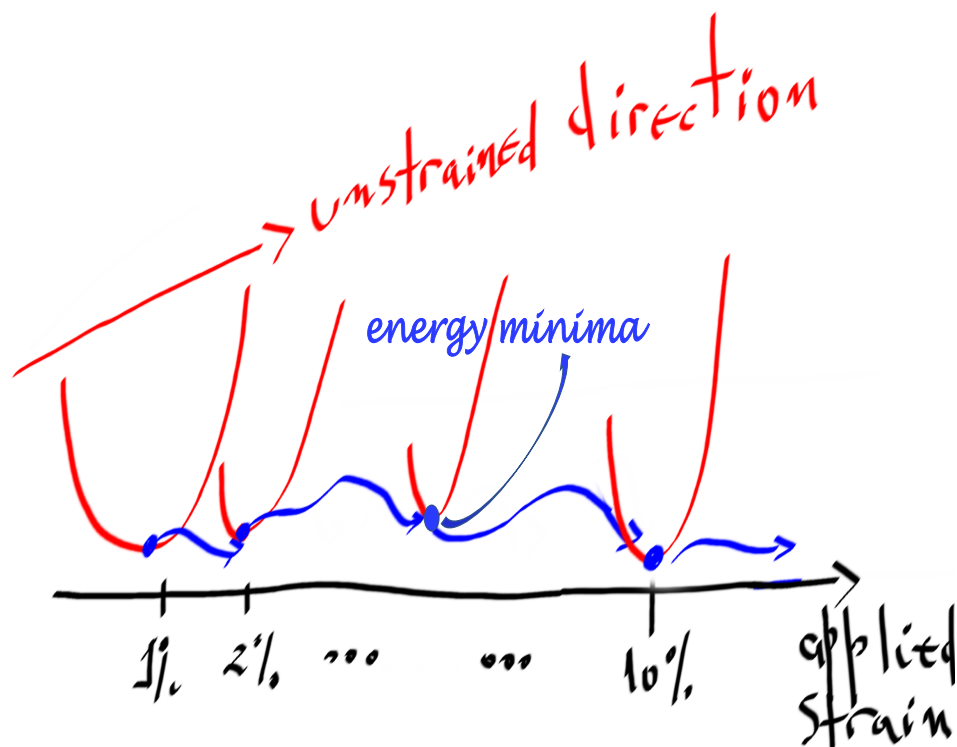


Figure 6.14: Illustration of the quasi-static(QS) process of application of a tensile strain to the 2D-SiO<sub>2</sub> bilayer. Starting from the equilibrium geometry, steps of tensile uniaxial strain of 1% are applied, generating a concatenated sequence of geometries of minimum energy (blue arrows), taking the last relaxed geometry as a starting point of the next step. Each equilibrium structure (blue points) corresponds to a constrained uniaxial strain, and the "red parables" correspond to the unconstrained direction, in which the relaxing process are allowed.

In this procedure, illustrated in Fig. 6.14, the system follows a path of quasi-static minima, as defined above. It corresponds to the physical process of tensile-strain experiments at sufficiently, low temperatures, at the tensile strain rates at which strain is applied in such experiments. A more conservative approach would use even smaller strain steps, but most, if not all, of the results we obtain are not affected by the somewhat large strain increase in our calculations, as described in the following. Figure. 6.15 shows the  $\sigma \times \varepsilon$  curve from our QS calculations. The following observations emerge from the figure:

- (1) similarly to the  $\sigma \times \varepsilon$  for three-dimensional SiO<sub>2</sub> in Fig. 6.1, we observe two linear

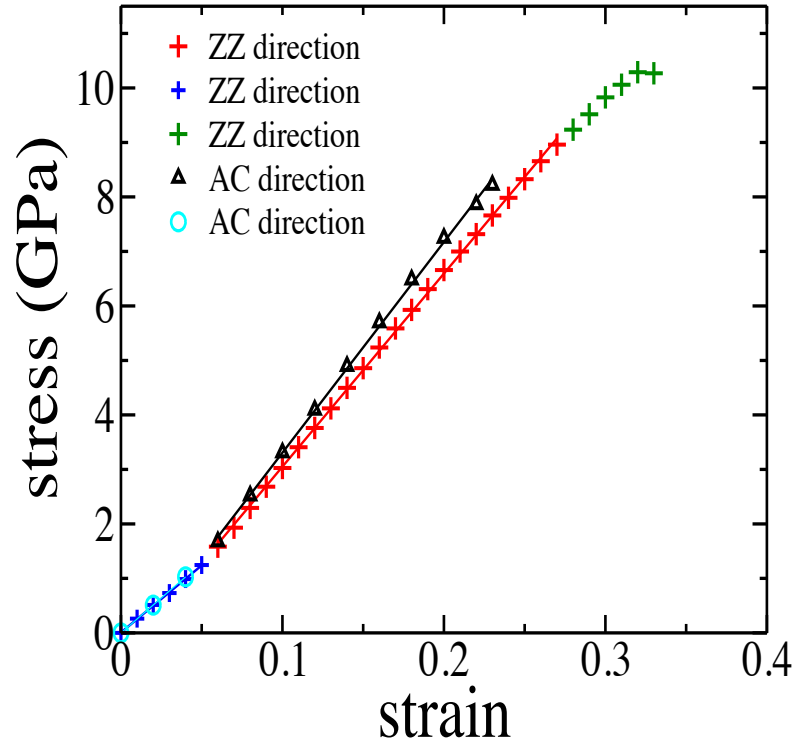


Figure 6.15: Stress-strain curve of 2D-SiO<sub>2</sub> bilayer, generated in the quasi-static(QS) sequence explained before. Tensile uniaxial strain is applied in the zig-zag(ZZ) and arm-chair(AC) directions. To small deformations  $\epsilon \leq 5\%$  AC and ZZ response overlap. As it happens in the 3D ( $\alpha$ -quartz) case, the mechanical response exhibits two linear elastic-deformation regimes.

elastic-deformation regimes, for both AC and ZZ directions;

(2) as expected due to hexagonal symmetry of 2D-SiO<sub>2</sub>, in the linear regime at small strains, the response to tensile strain is isotropic, and the AC and ZZ curves overlap for  $\epsilon \leq 5\%$ ;

(3) in the second elastic regime of deformation, the lattice is stiffer in the AC direction than in the ZZ direction;

(4) the 2D-SiO<sub>2</sub> shows an elastic response over a large interval of tensile strains, in both directions. The QS strain-constrained equilibrium structure at a strain  $\epsilon = 30\%$  relaxes back to the ground-state, if the applied strain is released. Below we propose a mechanism for the plastic response of 2D-SiO<sub>2</sub> based on instabilities of the QS minima at higher strains, that we observe in our calculations. But even in the regime of high strains, higher than  $\epsilon = 30\%$ , the QS minima relax to the strain-free ground state, for tensile strains in both AC and ZZ directions.

(5) at approximately the same value of strain,  $\sim \epsilon = 30\%$ , where the  $\sigma \times \epsilon$  relation for the 3D case in Fig. 6.1 indicates the onset of failure, the  $\sigma \times \epsilon$  curve for the 2D lattice suggests the onset of plastic deformation, for tensile strain in the ZZ direction. We comment on the case of the AC direction in the following.

Let us now examine the last one of the above observations in more detail. In what follows, we argue that the scissor and rotation modes of the 2D-SiO<sub>2</sub> lattice provide what would amount to a mechanism of plasticity without plastic flow for the material, at very small tem-

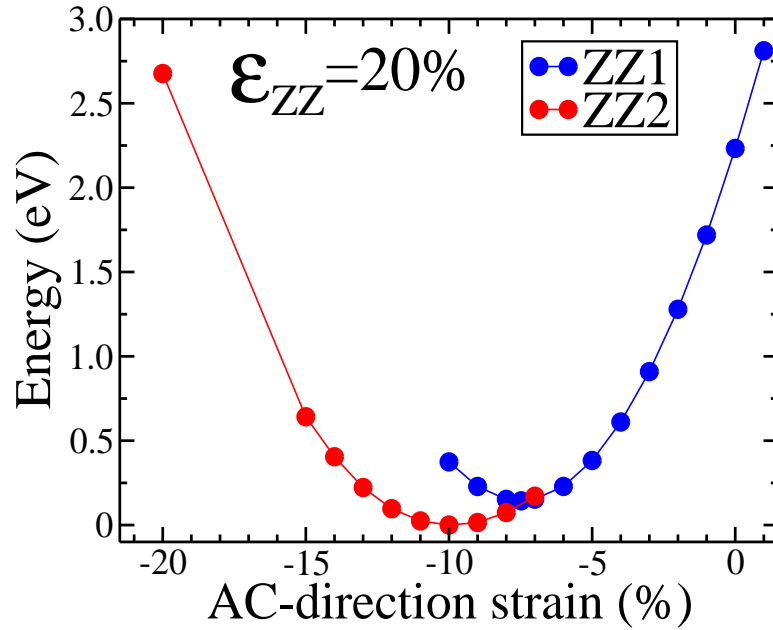


Figure 6.16: Quasi-static(QE) energy of the 2D-SiO<sub>2</sub> as a function of the strain in the arm-chair(AC) direction, corresponding to a fixed value of strain of 20% in the zig-zag(ZZ) direction. The strained situation leads to two branches of deformation labeled as ZZ1 and ZZ2, whose different geometries can be appreciated in the fig 6.18.

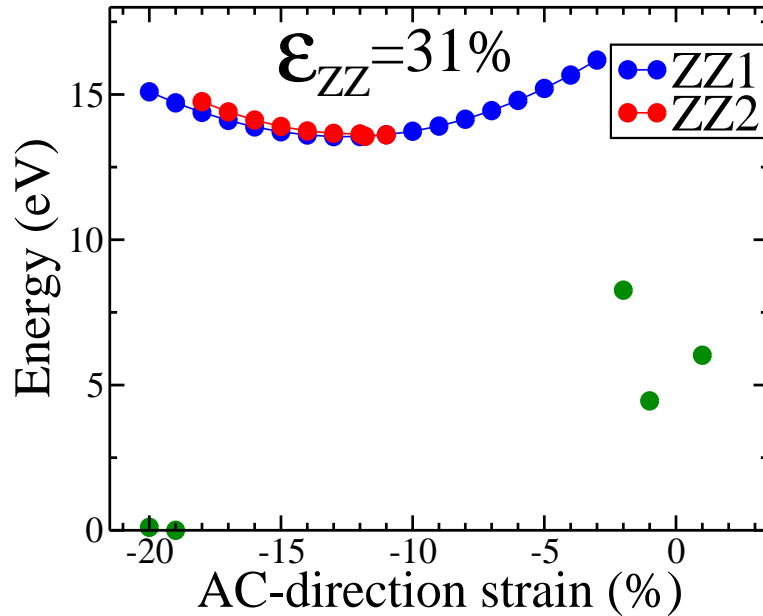


Figure 6.17: Quasi-static(QE) energy of the 2D-SiO<sub>2</sub> as a function of the strain in the arm-chair(AC) direction, corresponding to a fixed value of strain of 31% in the zig-zag(ZZ) direction. The strained situation leads to two branches of deformation labeled as ZZ1 and ZZ2, whose different geometries can be appreciated in the fig 6.19. The green circles indicate instabilities of the QS branches.

peratures (0 K is the temperature in our QS calculations).

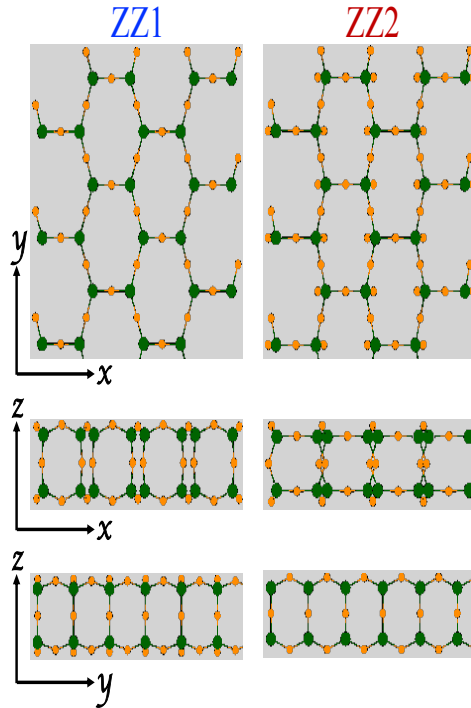


Figure 6.18: Equilibrium geometries corresponding to ZZ1 and ZZ2 branches from figure 6.16. The difference between the two geometries shows the role played by the scissor and rotation modes in allowing several low-energy structures available.

We start from the case of tensile strain along the ZZ direction. Figures 6.16 and 6.17 show the numerical results for the relaxation procedure illustrated in Fig. 6.14 for two values (20% and 31%) of applied strain in the ZZ direction. In the ZZ case, we recall that the curves shown in the figures display the energy as a function of the strain in the AC direction, for a fixed value of the strain in the ZZ direction.

By exploring high values of negative and positive of strain in the AC direction, we were able to identify two branches of deformation, which we label as ZZ1 and ZZ2, shown as red and blue circles in the figures. Fig. 6.16 shows the case of a fixed strain of 20% in the ZZ direction. The zero of the energy axis is at the minimum value of energy between the two curves. In the minimum of each curve, the strain vanishes in the AC direction.

In Fig. 6.18 we display a top view ( $xy$ -plane) of the QS minima for the two branches, as well as side views along the AC ( $x$ -axis) and ZZ ( $y$ -axis) in both cases. In the ZZ1 branch, the response to the applied strain involves the scissor and rotation modes of the external-layer oxygen atoms only. The middle-layer O atoms remain aligned with their two nearest-neighbor Si atoms from the external layers. On the other hand, in the ZZ2 branch, the middle-layer O atoms are also involved in the structural response to strain, being no longer aligned with their nearest neighbor Si atoms. Another difference is that, in the ZZ2 branch, O atoms joining Si atoms in a external layer along the AC direction are now on the same plane as the Si atoms, while O atoms joining Si atoms along the ZZ direction remain off plane. At a strain of  $\varepsilon_{ZZ} = 27\%$  the two branches remain distinct but become degenerate near the QS minimum.



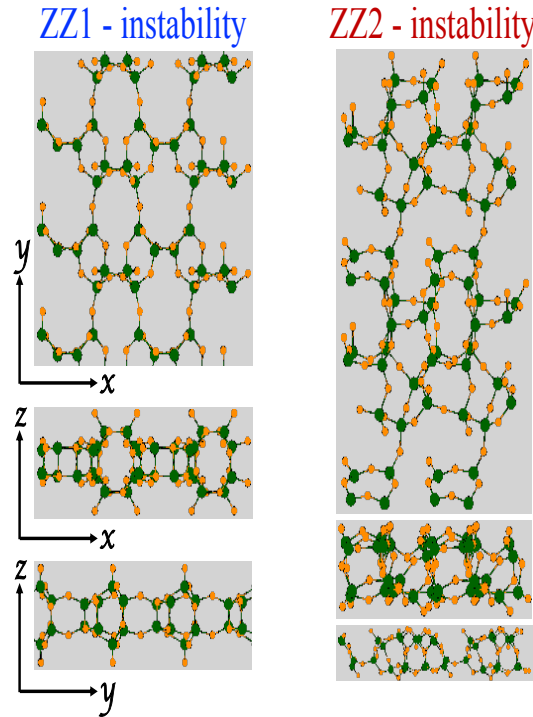


Figure 6.19: Lower energy geometries from unstable structures coming from the ZZ1 and ZZ2 branches. At the left, a final structure coming from a ZZ2 unstable geometry, characterized by a complex arrangement of SiO<sub>2</sub> tetrahedra, not cracked. At the right, the unstable structure coming from the ZZ2 branch converges in a disordered low energy geometry, characterized by undercoordinated O atoms, also not cracked.

Figure 6.17 shows the ZZ1 and ZZ2 branches for  $\varepsilon_{ZZ} = 31\%$ . The ZZ1 branch is slightly lower in energy and for  $\varepsilon_{AC} \geq -11\%$  the ZZ1 and ZZ2 branches become structurally identical. The green circles show instabilities of the QS branches. In the ZZ1 branch, the instability occurs for  $\varepsilon_{AC} \geq -2\%$ , and for  $\varepsilon_{AC} \leq -19\%$  in the ZZ2 branch. Unstable structures in the ZZ1 branch undergo a structural transition towards the lower-energy structure show on the left in Fig. 6.19. This is an ordered structure composed of a complex arrangement of SiO<sub>2</sub> tetrahedra, and is certainly a stiff, not cracked, lattice. In the ZZ2 branch, the unstable structures undergo a transition towards the structure show on the right in Fig. 6.19. This is a disordered structure, that shows undercoordinated O atoms. It is also a stiff lattice, with no fully formed crack.

Our view of the role of these instability in the response of 2D-SiO<sub>2</sub> is as follows. At  $\varepsilon_{ZZ} = 31\%$ , there is an energy difference of 55 meV/atom between the QS minimum of the ZZ1 branch and the structure with  $\varepsilon_{AC} \geq -3\%$ , the stable structure immediately to the left of the unstable geometry of the ZZ1 branch. In the ZZ2 branch, there is an energy difference of 25 meV between the minimum and the structure with  $\varepsilon_{AC} \geq -18\%$ , the stable structure immediately to the right of the unstable geometry. Both values are of the order of thermal-energy fluctuation per atom at room temperature ( $1.5kT = 39$  meV). Thus, rather than remain in the QS minimum until the lattice fractures, the 2D-SiO<sub>2</sub> lattice undergoes transformation to lower energy structure that are more stable at the high strains in our numerical experiment.

This picture of the problem rests on the availability of several low-energy structures in

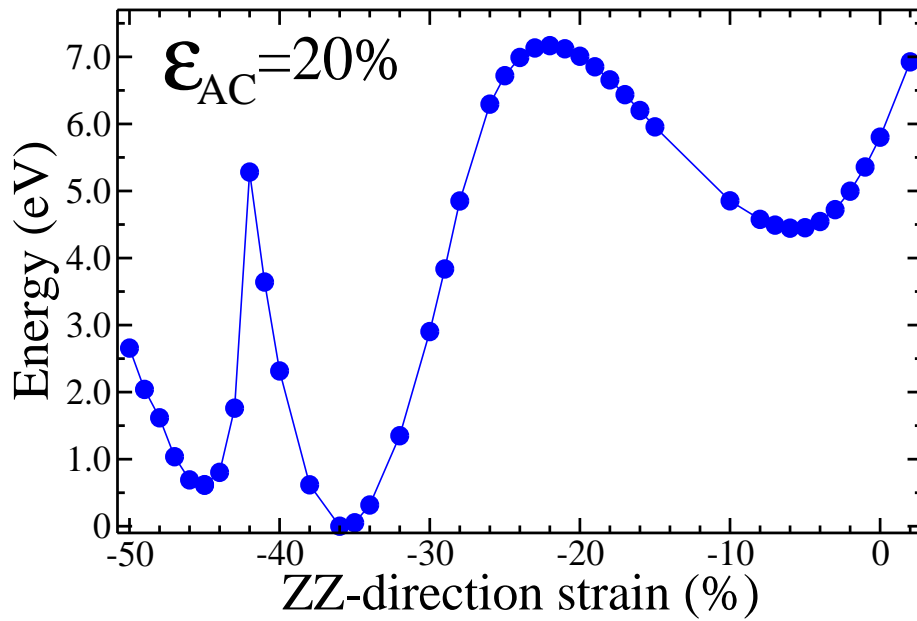


Figure 6.20: Quasi-static(QE) energy of the 2D-SiO<sub>2</sub> as a function of the strain in the zig-zag(ZZ) direction, corresponding to a fixed value of strain of 20% in the arm-chair(AC) direction. The behavior in the AC direction is different from the ZZ orientation, the QS curve develops two additional minima for high compressive strains.

the potential energy surface of the 2D-SiO<sub>2</sub> atomic lattice, connected with the low-energy structural excitations involving the scissor and rotation modes of the O atoms. Therefore, rather than forming a crack, the system makes a transition to a structure that is better adapted to the applied strain, and should start a new  $\sigma \times \varepsilon$  elastic response with respect to the new minimum. Plasticity in this case would be embodied not in the formation of dislocations and occurrence of plastic flow, but in the strain-induced transition to many available minima in the energy surface of the system.

Let us shift now to the case of the response of the 2D-SiO<sub>2</sub> bilayer to tensile strains in the AC direction. Figures 6.20 e 6.21 show the QS energy as a function of the strain in the ZZ direction, for two fixed values of the strain in the AC direction,  $\varepsilon_{AC} = \geq 20\%$  and  $\varepsilon_{AC} = \geq 25\%$ , respectively. Note that in the AC direction, the process evolves differently with strain. In Fig. 6.20, for  $\varepsilon_{AC} = \geq 20\%$ , we do not observe two deformation modes, but the QS energy curve develops two additional minima for very high compressive strains in the ZZ direction.

Because the two minima to the left of the QS minimum in Fig. 6.20 merge and become the same at an AC strain  $\varepsilon_{AC} = \geq 25\%$  where instabilities set in, we concentrate the discussion on the QS minimum at  $\varepsilon_{ZZ} = \geq -6\%$  and the second minimum at  $\varepsilon_{ZZ} = \geq -36\%$ . For  $\varepsilon_{AC} = \geq 20\%$  in Fig. 6.20, the barrier between these two minima is 57 meV/atom, already of the order of the thermal fluctuation energy per atom at room temperature.

The QS energy as a function of ZZ strain, for  $\varepsilon_{AC} = \geq 25\%$ , is shown as blue circles in

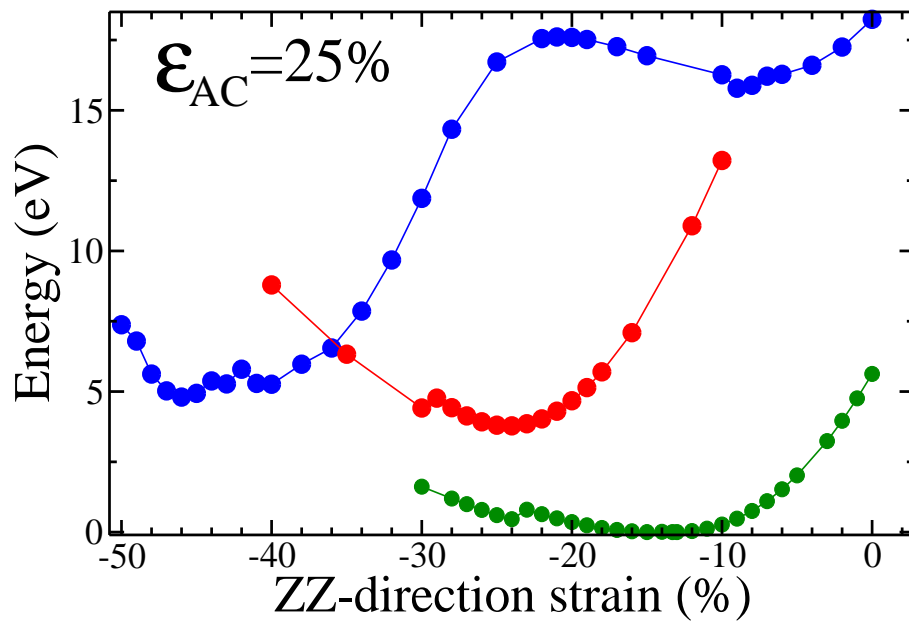


Figure 6.21: Quasi-static(QE) energy of the 2D-SiO<sub>2</sub> as a function of the strain in the zig-zag(ZZ) direction, corresponding to a fixed value of strain of 25% in the arm-chair(AC) direction (blue circles). Red circles show the QS curve derived from the numerical instability in the attraction basin of the lower minimum of the blue QS curve. Green circles indicate the QS energy derived from a instability in the attraction basin of the first higher-energy QS minimum of the blue curve.

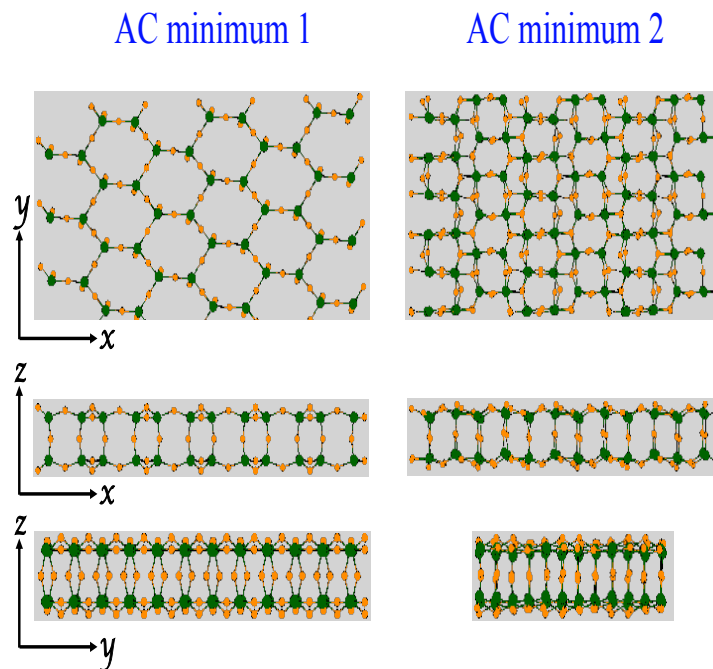


Figure 6.22: Structures associated with the two minima of the QS curve in fig 6.20. Strain in the AC direction involves displacements of O atoms from the middle layer, showing a tendency for corrugation.

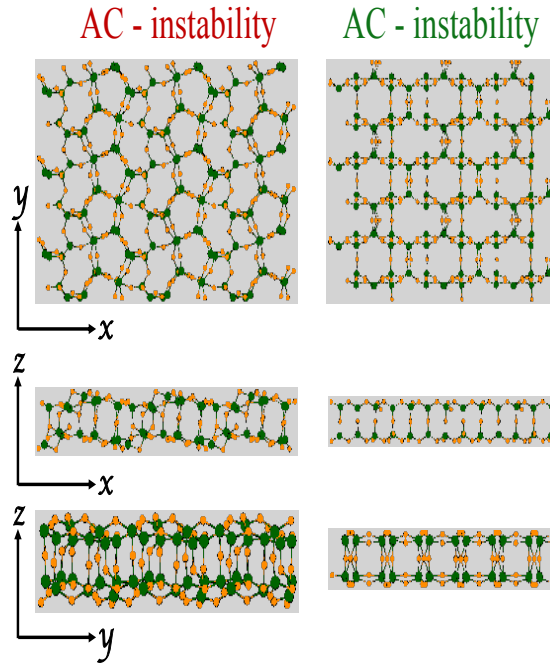


Figure 6.23: Structures associated with the two minima of the QS curve in fig 6.21. Strain in the AC direction involves displacements of O atoms from the middle layer, showing a tendency for corrugation.

Fig. 6.21. Numerical instabilities set in and we obtain two new deformation paths at much smaller energies. The QS energy curve shown as red circles in Fig. 6.21 derives from the numerical instability in the attraction basin of the lower minimum of the blue QS curve, while the green circles show the QS energy for a geometry that derives from an instability in the attraction basin of the first higher-energy QS minimum of the blue curve.

The structures for the two minima of the (blue) QS curve are shown in Fig. 6.22, and the QS minimum for the green and red curves are shown in Fig. 6.23. Response to tensile strain in the AC direction in general involves displacements of O atoms from the middle layer and show a tendency for corrugation in the external sublayers of the O atoms.

Therefore, again we observe that the 2D-SiO<sub>2</sub> lattice makes transition to lower-energy geometries at high AC-direction strains, and a “plasticity” mechanism operates, where the lattice rather than undergo fracture, makes a structural transition to another stiff configuration of the atomic lattice.

One final observation is that in all quasi-static energy curves we investigated here, the QS minimum relaxes back to the ground-state, even for very large strains in both directions.

## 6.4 Partial conclusions - anomalous mechanical response of two-dimensional SiO<sub>2</sub>

A singular mechanical behaviour of 2D-SiO<sub>2</sub> bilayer, within the framework of Kohn-Sham DFT, has been presented and addressed. The ground state geometry, experimentally established

as a straight bonds geometry (labeled G1 in the text), characteristic of the hexagonal pristine 2D-SiO<sub>2</sub> bilayer, has become matter of enlightenment in this work. Here we presented three different possible geometries to the ground state (labeled G1,G2 and G3), all of them with little energy differences and related between them through transformations involving our so called "soft modes". Our results suggest that however the three geometries are possible, the different final geometries, produced by plane waves and localized atomic orbitals codes, come from the incomplete nature of the localized basis. However, the happening of this three almost degenerate geometries, joint with two new equilibrium geometries ( $\beta$ -2D auxetic and tetraoctite-2D silica) shown early evidences of a very general statement observed in all our work: the existence of an energy surface characterized by many metastable states.

Our Study in the anomalous response to bending deformations, through building of 2D-SiO<sub>2</sub> nanotubes, showed the possibility of different final geometries associated with the same nanotube and almost degenerate energies. Also, we observe a pronounced trend despite of the quirkality, to form kinks in small radius nanotubes, in a competitive compromise between to curve continuously or to form a kink, leading to plane regions with very little stored elastic energy. In small radius nanotubes (high curvature) there are no energy barriers to form a kink, while in big radius nanotubes (small curvature) the kink formation process need to be activated. In contrast with graphene, where the energy per SiO<sub>2</sub> unit diverges to small radius, the 2D-SiO<sub>2</sub> nanotubes don't show divergent behaviour, precisely due to the kinks formation. Fitting the elastic energy to a quadratic expression in the deformation we obtain to the bending stiffness a medium value of  $\kappa = 18.5$  eV, using larger radii nanotubes, and  $\kappa = 13.31$  eV with all nanotubes, being clear that no straight line fits well the scatter of energy values. This value aproximates acceptably well to the experimental value of  $\kappa = 8.8 \pm 0.5$  eV obtained using inelastic helium atom scattering (HAS).

Finally, our studies in quasi-static(QS) tensil uniaxial strain, showed that the 2D behaviour shares with the 3D ( $\alpha$ -quartz) the interesting characteristic of two different linear regimes. In a second place, this material exhibits a pretty wide range of elastic response, being able to relax to the pristine geometry coming from strained geometries as far as  $\epsilon=30\%$ , and more surprisely, our observations shown that in all quasi-static energy curves investigated here the QS minimum relaxes to the ground state (pristine 2D SiO<sub>2</sub>), even for very large strains in both directions, zig-zag(ZZ) and arm-chair(AC). This 2D material offers the possibility of several low-energy structures accesible in the termal energy range, we propose scissor and rotation modes as the microscopic mechanisms of transit between this local minima. In this context, our system have a "crack avoiding", because it prefers to do a structural transition to more favorable geometry that acts as a new starting point for the mechanical strain, allowing the possibility of stretching withouth to crack. We propose that plasticity in this material is driven no by usual mechanisms such as formation of dislocations or plastic flow, but by the strain-induced transition to many available minima in the energy surface of the system.

## Chapter 7

### Topological defects

Stone-Wales (SW) and other topological defects are regularly observed in two dimensional materials [117], it consists in rotating a 16 atoms unit (or a Si-O-Si bond)  $90^\circ$  around the center, changing the pristine four hexagons arrangement to two units of pentagon-hexagon (so called 57 defect) (see FIG.7.1a). This bond rotation can be used to build supercell models of amorphous 2D silica, with distributions of polygons with different number of sides (from 4 to 9) [7] [9] [6]. At this time we did six models of topological defects: SW (complete and superior 7.1a,7.1b), 585 (complete and superior 7.1c,7.1d), and 555777 (complete and superior 7.1e,7.1f), the term superior means to rotate only the first layer of the bilayer and the term complete means to rotate both layers. In general terms, the effect of this kind of topological defects was to reduce the band gap through the introduction of plane states or narrow bands near to the conduction band. As expected, the defect states show a more delocalized nature highlighted in being necessary taking in count more and more atoms to determine atomic contributions to the defect states.

In the case of defects SW and SW-sup, the formation energy is just the difference between the supercell's energy with the defect and without it (the pristine bilayer), on the other cases (585, 585-sup, 555777 and 555777-sup) the formation energy is obtained subtracting the potential energy associated to two and four units of  $SiO_2$ , to take into account the supercells have different number of atoms. Obtained formation energies are presented in TABLE 7.1.

Majority energies of formation are between 0.59 and 5.70 eV. The defect more energetically favorable are the oxygen monovacancy at the middle of the bilayer with 0.59 eV. The less probable defects are: the Si monovacancy with a big 13.23 eV formation energy, and the 585 and 555777 topological defects, with 14.18 eV and 10.84 eV respectively. It is very interesting, comparing the formation energy of SW and SW-sup, contrary to common sense, that is more easy to turn both layers to build a SW complete defect than to turn only one layer, with a 1.45 eV difference. The 585 defect behaves as expected: is easier to turn just one layer than to twist both layers. Finally, the defects 555777 and 555777-sup show almost the same energy.

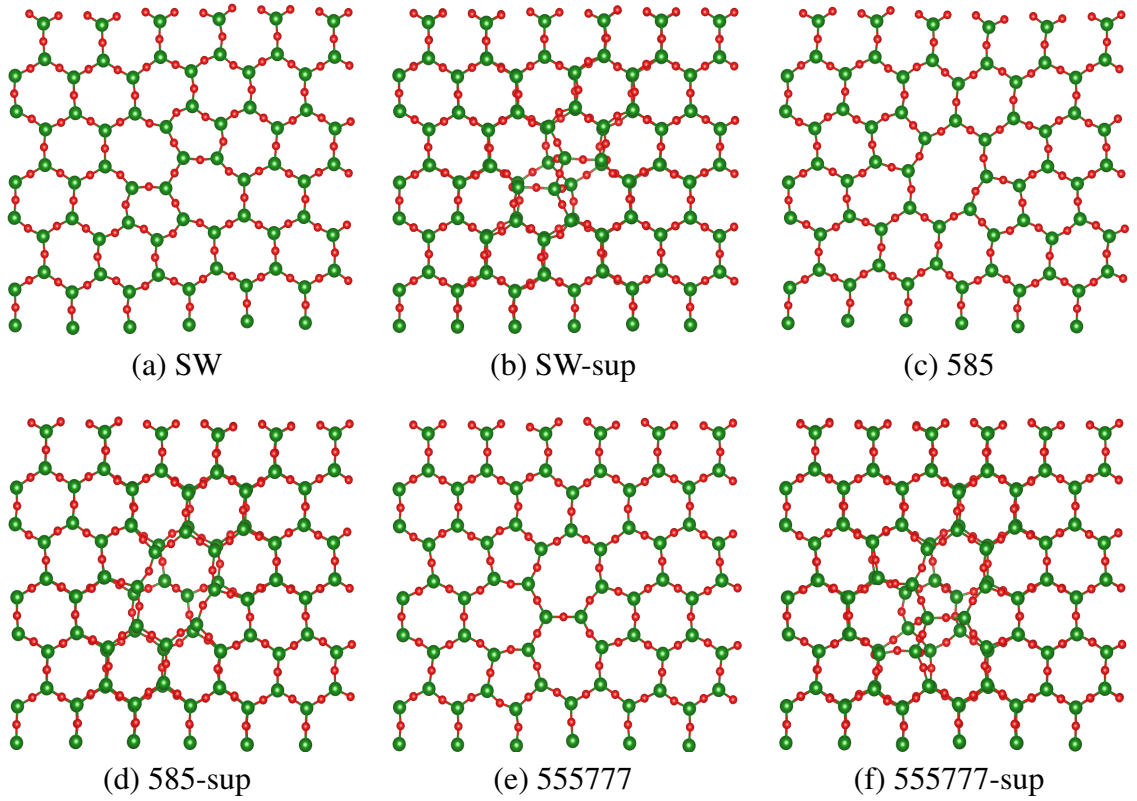


Figure 7.1: Relaxed geometry of Topological defects. The '-sup' label means that only the uppermost layer of 2D SiO<sub>2</sub> is involved in the built defect.

Table 7.1: Formation energy of neutral defects. In bold mode formation energies associated with topological defects.

Defect	Si-rich limit (eV)	O-rich limit (eV)
$V_O^{mid}$	0.59	4.95
$V_O^{ext}$	1.03	5.39
$V_{Si}$	13.23	4.53
$I_O^{mid}$	7.97	3.61
$I_O^{ext}$	5.70	1.34
$I_{Si}$	4.02	12.72
$Al_{Si}$	-0.23	-8.95
$B_{Si}$	1.28	-7.44
<b>SW – sup</b>	<b>4.34</b>	<b>4.34</b>
<b>585 – sup</b>	<b>10.63</b>	<b>10.63</b>
<b>555777 – sup</b>	<b>10.66</b>	<b>10.66</b>
<b>SW</b>	<b>2.89</b>	<b>2.89</b>
<b>585</b>	<b>14.18</b>	<b>14.18</b>
<b>555777</b>	<b>10.84</b>	<b>10.84</b>

## Chapter 8

### Charged defects

As it was emphasized in the theory of charged defects, a doped semiconductor is a ionized state of a neutral defect where charge has been transferred between the bands and the defect states, located in the band gap. This charge transfer is usually explained as a consequence of the more delocalized nature of the EMT states, this allows charge transfer due to the coupling between the defect state and the edge of the bands: in a doped type n semiconductor, with the edge of the conduction band; and in a type p doped semiconductor, with the edge of the valence band.

As a prototype of a complete study of charged defect we present the P substitutional impurity in 2D silica. The methodology used to study this defect is the usual DFT as implemented in the VASP software [37], but constraining the electronic population, in order to create the desired charged defect, using the Pantelides fundamental approach [23], avoiding the wide spread method of *ad hoc* corrections, of the spurious Coulomb interactions between charges from periodic images. Fixing electronic populations is a particular case of a more general method called constrained DFT (CDFT), that minimizes the functional of the energy, usually constrained to the number of electrons, but introducing a new Lagrange multiplier associated with the new constrain. In this case, the electronic population in the defect level, see for instance [118–120]. To charged defects calculations was used a 192 atoms supercell, with a vacuum dimension of 15 Ang to avoid interaction between the periodical images. A 400 eV Plane wave cutoff in a single  $\Gamma$  k-point grid. The Forces between the atoms were relaxed to values less than 0.01 eV/A. To describe the exchange and correlation effects was used the Perdew-Burke-Ernzehof generalized gradient approximation (GGA), while the VASP plane augmented wave pseudopotentials, provided by the VASP distribution. The Plane Augmented Wave (PAW) method was originally developed by Blöchl in 1994 [121], and the main idea is to combine the pseudopotential method with the augmented plane wave approach, in a such way that through a transformation, between the pseudo wavefunctions and the true wavefunctions, it is possible to recover the complete nodal structure into the atomic core, allowing an efficient and precise manipulation of valence orbitals considered 'core' as the 2p oxygen, or the d or f orbitals to the first row of periodic table, with a less number of plane waves. About PAW see for instance [37, 121, 122].

Just to understand in detail the emergence of defect levels induced by P substitutional,



we start with the bands structure without spin polarization. The effect of P is to introduce a deep level located at  $\epsilon_c - 1.74$  eV, partially occupied with energy equal to the Fermi energy (see figure 8.1 left). In the spin polarized calculation the defect level splits in two levels, one occupied and other unoccupied, around the Fermi energy, the split value is 1.32 eV. The unbalanced spin populations leads to a magnetic behavior of the P impurity.

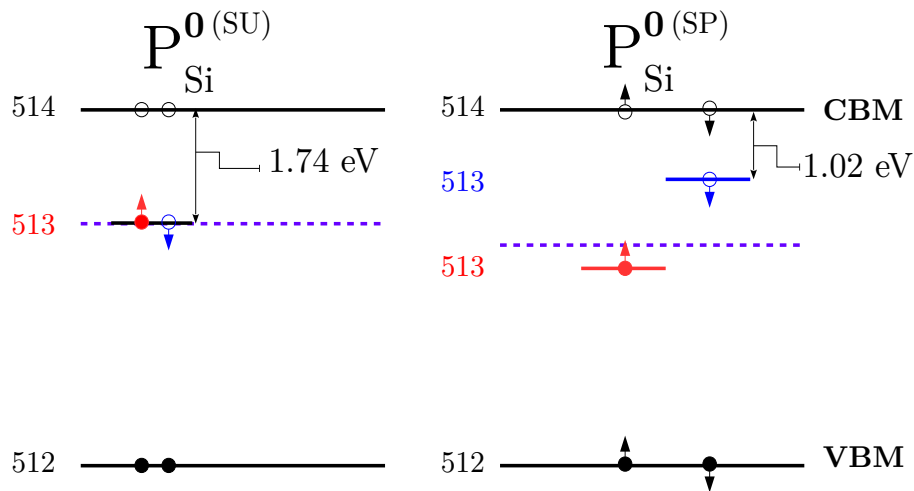


Figure 8.1: Scheme of energy levels of substitutional phosphorus to each charge state. Neutral defect. Spin unpolarized (SU) and spin polarized (SP) calculations. In the spin unpolarized calculation the defect level is half filled. In the Spin polarized case, we have a 1.32 eV spin-splitting, leading to a spin majority state filled and a spin minority state empty.

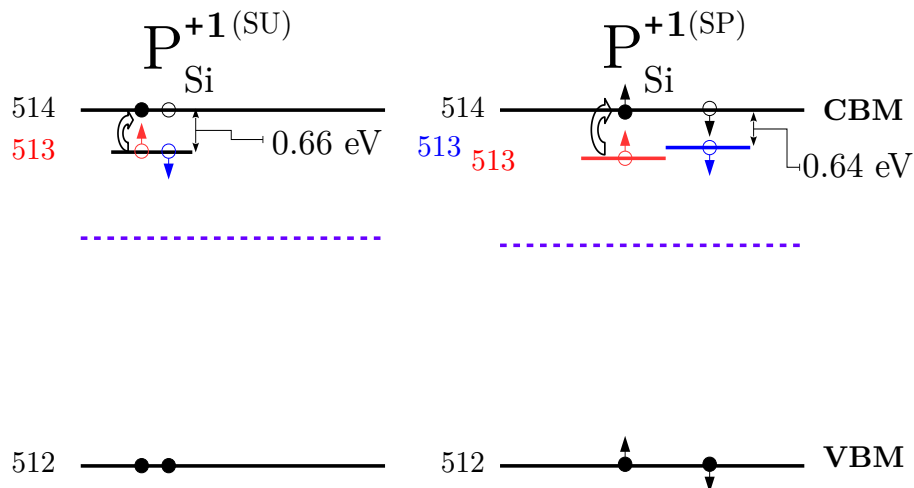


Figure 8.2: Scheme of energy levels of substitutional phosphorus to each charge state. Positively charged defect. Spin unpolarized (SU) and spin polarized (SP) calculations. In the spin unpolarized (SU) calculation the defect level is fill, because one electron initially in the defect state was promoted to the conduction band, leading the localized defect state positively charged. In the spin polarized (SP) case, we have a 0.11 eV spin-splitting. One electron was promoted to the conduction band, leading the localized defect positively charged.

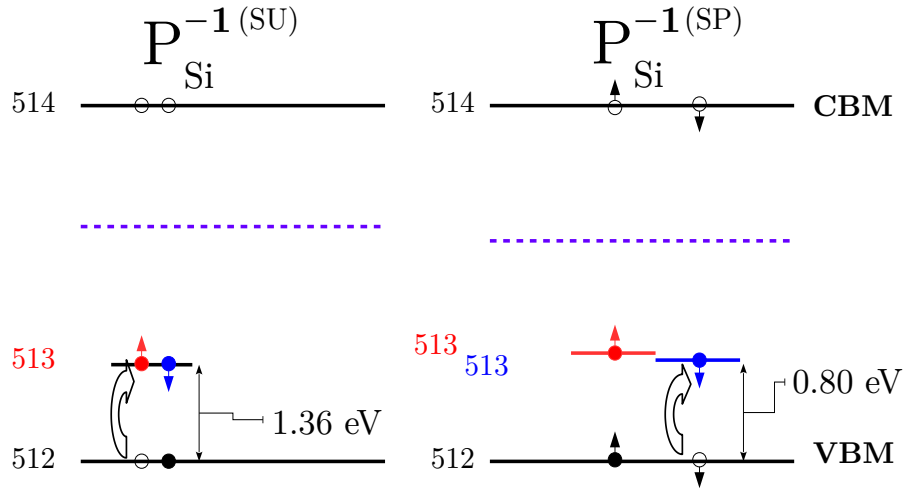


Figure 8.3: Scheme of energy levels of substitutional phosphorus to each charge state. Negatively charged defect. Spin unpolarized (SU) and spin polarized (SP) calculations. In the spin unpolarized (SU) calculation the defect level is full, one electron initially in the valence band was promoted to the defect state, leading the localized defect state negatively charged. In the spin polarized (SP) case, we have a 0.09 eV spin-splitting. One electron was promoted from the valence band, leading the localized defect negatively charged.

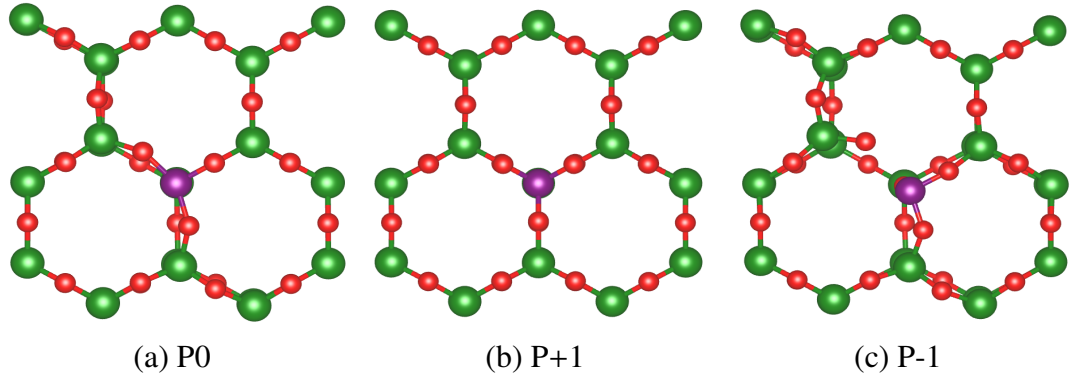


Figure 8.4: Detail of relaxed geometry of substitutional phosphorus to each charge state. a) Neutral defect b) Positively charged c) Negatively charged.

The formation energy is essentially the difference between the supercell with the defect and the pristine bulk, taking into account the energy inserted or drawn to the system by the replacement of the host for the impurity through the chemical potential of each atomic specie:

$$E_f^d = (E_{tot}^d - \mu_P) - (E_{tot}^{bulk} - \mu_{Si}); \quad (8.1)$$

where  $\mu_P$  and  $\mu_{Si}$  are the chemical potentials associated with each atomic specie. To charged defects the formation energy depends additionally on the position of the Fermi energy, that accounts the energy added or subtracted to the system associated by the addition or subtraction of an electron:

$$E_f^d = (E_{tot}^d - \mu_p) - (E_{tot}^{bulk} - \mu_{Si}) + q(\mu_e + \epsilon_v); \quad (8.2)$$

where,  $q$  is the electronic charge corresponding to the number of electrons added or subtracted, and  $\epsilon_v$  is the energy of the top of the valence band, it is taken generally as reference, and can be defined as zero.

The positively charged defect ( $q=+1$ ) is built from the neutral, taking as starting point the wavefunctions and density previously converged in the neutral charge state, but constraining or fixing by hand the electronic populations to guarantee the defect to be positively charged. In the P impurity case, we have to promote the only one electron in the defect level to the conduction band. To get a negatively charged defect we need to promote an electron from the valence band to the only one unoccupied state on the defect level. It is worthy to recall that in creating charge states plays an essential role the localized character of the defect level in contrast with the totally delocalized nature of the scattering solutions from the bands.

Looking to the relaxed geometries, the  $q=+1$  geometry fits in the original geometry without appreciable distortion, and shows a lower energy than the  $q=-1$  charge state. The neutral defect appears most like middle way between these two extremes. As a result is not surprising, the positively charged defect resembles the original electronic valence of the Si host atom.

Note that there are not more possible charge states to this defect level, because the defect level only has two states to occupy. However, in general, other charge states with more states in the gap, allow higher charge states just promoting electrons to the conduction band to generate positively charged states ( $q=+2,+3,\dots$ ); or from the valence band to the defect levels to generate negatively charged states ( $q=-2,-3,\dots$ ). Of course, the energy is increased to higher charge states and eventually those will be unstable.

According to the chemical environment we have two limiting conditions: Si-rich condition and O-rich condition. To each one we have different formation energies and stability conditions to the defect. In the Si-rich condition, the  $q=+1$  defect, despite of being possible in terms of available states, presents high energy in the disposable electronic chemical potential, that runs from zero to the gap value ( $E_g=5.6$  eV), so is unstable. Only neutral and negatively charged states are possible (see figure 8.5(a)). Furthermore, on the O-rich condition, is also unstable the  $q=+1$  charge state, in comparison with the neutral and negatively charged states (see figure 8.5(b)).

## 8.1 Partial Conclusions - Charged defects

The energy of formation of neutral defects is well defined and it does not offer a challenge, unless the natural computational cost associated with the number of atoms in the supercell. The problem of determining formation energy of charged defects, within first principles DFT supercell approach, deals with the Coulomb interaction between the periodical images, induced by the boundary periodic conditions. There are two basic methods to face with this problem: in first place, *ad hoc* corrections, through multipolar fittings of total energy from supercells with different size in the infinite supercell limit; and the fundamental WZP method [23, 67],

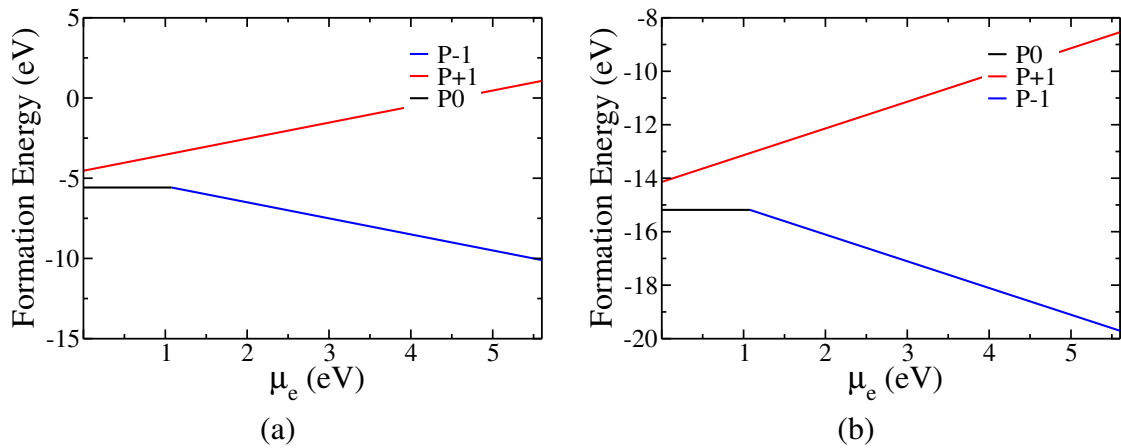


Figure 8.5: Formation energies, as a function of the Fermi level ( $\mu_e$ ), for P substituting Si in 2D SiO<sub>2</sub> bilayer. a) For silicon-rich condition. b) For oxygen-rich condition. The slope shows the charge state according with 8.2. Neutral: 0 (black horizontal line),  $q=+1$  (red line),  $q=-1$  (blue line).

avoiding spurious introduction of truly charged defects, keeping the charge neutrality in the supercell, allowing the charge transfer between the localized defect states and the delocalized bands.

We study the charge states induced by a phosphorus impurity, substituting silicon in 2D SiO<sub>2</sub>, through the WZP method. This methodology uses the usual DFT approach, but constraining the electronic population at the defect states by hand, transferring charge between the defect and the bands. The phosphorus (P) impurity generates an only one defect state half filled in the gap. In the neutral impurity this state is spin splitted, in two spin levels: the majority spin state is filled and the minority state is empty. Transferring charge between the localized defect level and the delocalized wavefunctions of the bands we attain a state positively charged, where both spin levels in the gap are empty; and a negatively charge state where both spin splitted defect levels are filled.

The minimum energy DFT algorithm, leads the supercell to three different relaxed geometries: The neutral defect, tilts two of the three Si-O-Si bonds in the external layer where the guest phosphorus is located; the positively charged defect leads the geometry almost unchanged, what is expectable because a positively ionized phosphorus have the same silicon's valence; finally, the negatively charged defect, where the geometry is strongly distorted originating oxygen and phosphorus dangling bonds. Analyzing the formation energies as a function of the electronic chemical potential, ranging through the gap (5.6 eV), show that only the neutral and the positively charged states are allowed, in both chemical environments considered: Si-rich and O-rich conditions.

# Chapter 9

## Publications

Our study of 2D-SiO<sub>2</sub> originated the following publications:


PHYSICAL REVIEW B **106**, 155416 (2022)

---

### Carrier trapping centers in a two-dimensional silica bilayer: Strongly localized shallow gap states and resonances induced by oxygen vacancies

Nestor Fajardo  and Ricardo Wagner Nunes \*

*Departamento de Física, Universidade Federal de Minas Gerais, Belo Horizonte, Minas Gerais, Brazil*

 (Received 6 May 2022; revised 11 August 2022; accepted 27 September 2022; published 18 October 2022)

Structural and electronic properties of neutral native defects in a two-dimensional SiO<sub>2</sub> bilayer (2D-SiO<sub>2</sub>) are examined using the SIESTA *ab initio* approach. We identify scissor and rotation modes of oxygen atoms, in the middle of Si-O-Si chains, as low-energy structural excitations responsible for the response of the 2D-SiO<sub>2</sub> lattice to the formation of all native defects in the present study. Furthermore, we find that oxygen native defects (single vacancies and interstitials) should be the most abundant defect species in thermal-equilibrated samples. Regarding native-defect electronic states, single oxygen vacancies and interstitials are found to be amphoteric trapping centers in 2D-SiO<sub>2</sub>. Silicon vacancies and interstitials introduce several strongly localized states spanning a large fraction of the gap. Generally, we identify a marked tendency for the appearance of strongly spatially localized defect states, be their energies shallow or deep within the band gap, as well as the emergence of strongly localized resonances in the valence and/or conduction bands. Strong spatial localization of defect states, a hallmark of systems displaying trapping and polaronic effects, is a result of quantum confinement and enhanced Coulombic effects in this 2D system. Carrier trapping and polaron formation are thus expected to be a common feature of defect states and added carriers in 2D-SiO<sub>2</sub>.

DOI: [10.1103/PhysRevB.106.155416](https://doi.org/10.1103/PhysRevB.106.155416)

Figure 9.1: Publication about structural and electronic properties induced in 2D-SiO<sub>2</sub> by native defects.

## Chapter 10

### Conclusion and perspectives

Structural, electronic and mechanical properties of the 2D-SiO<sub>2</sub> bilayer has been studied, within the Kohn-Sham DFT framework, using the PBE-GGA functional to describe exchange and correlation effects. The pristine bilayer is a ultrathin insulator with a direct band gap of 5.6 eV, underestimating the experimental value (6.7 eV) only in 16 %. In this insulator, dangling bonds are absent, displaying chemical bonds completely saturated. The valence band comes from non bonding p-like orbitals from the oxygen atoms located at the external layers, and the conduction band is derived from s and p orbitals from silicon atoms. As part of the valence band, 2D SiO<sub>2</sub> displays a strong van Hove singularity from p<sub>z</sub>-like orbitals from the external oxygens. This singularity should give rise to a strong peak in the ultraviolet absorption.

2D SiO<sub>2</sub> reacts locally to all the studied point defects: natives and substitutionals. The two honeycomb lattices remain practically unaffected by the presence of the defects, unless at the core region. In this study we propose the system responds to point defects while low-energy structural excitations: a scissor mode, where the Si-O-Si bonds change the angle, and a rotation mode where the Si-O-Si bond turns around the Si-Si minimal distance. We believe those soft modes are in deep relation with the anomalous behaviour of 2D SiO<sub>2</sub>.

In terms of electronic structure, oxygen monovacancies and single interstitials act as amphoteric trapping centers in 2D-SiO<sub>2</sub>. The novelty of this study rests in the strongly localized nature of shallow states induced by the defects. In a 3D material, the behaviour expected is shallow defects being EMT states, with certain degree of delocalization, and deep defects to be strongly localized. In 2D SiO<sub>2</sub> we find shallow states and resonances strongly localized, due to quantum confinement and enhanced Coulomb interactions. According with formation energies, we expect oxygen vacancies as the most abundant defect in 2D SiO<sub>2</sub>, in the range of chemical potentials considered. The middle layer oxygen vacancy is the most stable defect over the three-fifths of the energies ranging through the gap, from the valence to the conduction energies. Interstitial oxygen appears as the more stable defect in the O-rich limit.

In the study of Al and B as group III impurities, substituting the Si atom, Al shows a more stable configuration. Both substitutional species show spin-splitting of the levels in the gap. Strikingly, the Al impurity induces a spin separation, showing a different degree of localization to each spin channel. The chemical stability of the 2D silica permits, in principle,

the use of ultrathin 2D SiO<sub>2</sub> as insulating layers in magnetic tunnel junction devices, based in the tunneling magnetoresistance (TMR), induced by the insertion of a very thin insulator. Additionally, considering the spin separation, the inserting of a P doped 2D silica would lead to interesting phenomena.

Considering topological defects, builded in the silica bilayer, starting with the pristine cell and introducing stone-wales rotations, we find the SW as the more stable defect. It is interesting that in the SW and SW-sup defects, contrary to the common sense, it is more easy to turn both layers than to turn just one.

The phosphours substitutional is studied in their several charge states, through the Wu, Zhang and Pantelides's methodology, that avoids the spurious introduction of truly charged defects, keeping the charge neutrality in the supercell, transferring charge as happens in the nature: between the defect state and the bands. It admits only three charge states, neutral, positively and negatively charged. Only neutral and negatively charged states are allow in the range of considered chemical potentials.

A Singular mechanical behaviour was founded in 2D-SiO<sub>2</sub> silica. In first place, we identify three possible geometries to the ground state, in contrast with the only one reported by the experiments. This difference was adressed as a effect of the localized basis incompleteness. However, this numerical artifact showed early evidences of a very general statement observed throughout the entire work: the existence of an energy surface characterized by many metastable states. The study of bending stiffness, through building 2D silica nanotubes eliminates the divergent behaviour to small radius nanotubes, as observed in graphene for instance, due to the kink formation that reduces the energy of the system. To the bending stiffness we obtain a medium value of  $\kappa=13.31$  eV in a acceptably well agreement with the experimental value ( $\kappa=8.8\pm 0.5$  eV), obtained from a simple quadratic fitting. Finally, considering the quasi-static sequence where a tensile uniaxial strain is applied to the 2D silica, we found two linear elastic regimes, agreeing with the 3D ( $\alpha$ -quartz) behaviour obtained with molecular dynamics. Also our 2D silica exhibits a wide range elasticity, being able to recover to the unstrained ground state starting from: high tensile values of strain, or from a nanotube curved geometry. Overviewing all deformation tests applied, we conclude that the 2D silica has an energy surface offering many minima or metastable states, we propose the transit between them could be driven by the scissor and rotation low energy modes. The crack avoiding behaviour (kind of superelastic) is not driven by dislocations or plastic flow, but we propose a strain-induced transition that takes a more favorable energy as a starting point of a new deformation cicle, in certain way "resetting" the strained memory, thus allowing a highly flexible behaviour.

As perspectives, 2D SiO<sub>2</sub> silica bilayer despite its apparent simplicity hiddens many interesting details and potential applications. Along the way working with it in the computer DFT simulation, it leave a trace of interesting problems to be adressed:

In first place, as was stated in the introduction, to do a complete quasi-static cicles of loading and unloading to explore the complete stress-strain curve, taking into account the anomalous mechanical response and the wide elastic behaviour founded in this material.

Formation energies of topological defects (585, 555777) builded complete or only in the superior surface, appear higher than previous published results [117]. Where is the problem? Maybe the supercell size and interaction between the periodic images, give the size of the topological defects, far from point defects studied in the first part. In the paper they use thousands atoms supercell, while we use at most 432 atoms.

The Pantelides methodology is clean and appears more correct than doing *ad hoc* corrections. However, in the VASP code it was difficult to converge the calculations to the charge states in all the other defects studied (the only one converged quickly and easy was the P impurity).

Would be interesting to implement the Pantelides methodology in the SIESTA code (in fact it has a paper that claims to have made it), to take advantage of the previously converged supercells with all the point defect studied.

Quartz is a piezoelectric material. Silica 2D as a material based in the building tetrahedral units [SiO<sub>4</sub>] could be also enhanced piezoelectric response, it also doesn't have inversion symmetry. By other side, monolayer transition metal dichalcogenides (TMDC) exhibit stronger piezoelectric response [123]. it would be interesting to calculate piezoelectricity in 2D-SiO<sub>2</sub> using the modern polarization methodology (Vanderbilt-Resta).

To calculate polaronic behaviour in 2D-SiO<sub>2</sub>. It shows characteristics (such as the narrow top of the valence band) that could be interesting for polaron formation.



## Bibliography

- [1] Richard Bader. *Atoms in Molecules. A Quantum Theory*. Clarendon Press, Oxford, 1994. Cited in page 12.
- [2] R. Parr, P. Ayers, and R. Nalewajsky. What Is an Atom in a Molecule? *The Journal of Physical Chemistry A*, 109:3957, 2005. Cited in page 12.
- [3] M. Cohen, A. Wasserman, and K. Burke. Partition Theory: A Very Simple Illustration. *The Journal of Physical Chemistry A*, 111:12447, 2007. Cited in page 12.
- [4] M. Cohen and A. Wasserman. On the Foundations of Chemical Reactivity Theory. *The Journal of Physical Chemistry A*, 111:2229, 2007. Cited in page 12.
- [5] P. Elliot, K. Burke, M. Cohen, and A. Wasserman. Partition density-functional theory. *Physical Review A*, 82:024501, 2010. Cited in page 12.
- [6] K. Büchner and M. Heyde. Two dimensional silica opens new perspectives. *Progress in Surface Science*, 92:341–374, 2017. Cited 7 times in pages 13, 48, 64, 71, 81, 83, and 101.
- [7] L. Lichtenstein, C. Büchner, B. Yang, S. Shaikhutdinov, M. Heyde, M. Sierka, R. Włodarczyk, J. Sauer, and Hans-Joachim Freund. The Atomic Structure of a Metal-Supported Vitreous Thin Silica Film. *Angewandte Chemie International Edition*, 51(2):404–407, 2012. Cited 3 times in pages 13, 48, and 101.
- [8] M. Heyde, S. Shaikhutdinov, and H-J Freund. Two-dimensional silica: Crystalline and vitreous. *Chemical Physics Letters*, 550:1–7, 2012. Cited in page 13.
- [9] C. Büchner, L. Lichtenstein, X. Yu, J.A. Boscoboinik, B. Yang, W.E. Kaden, M. Heyde, S. Shaikhutdinov, R. Włodarczyk, M. Sierka, J. Sauer, and Hans-Joachim Freund. Ultrathin Silica Films: The Atomic Structure of Two-Dimensional Crystal and Glasses. *Chemistry - A European Journal*, 20:9176–9183, 2014. Cited 2 times in pages 13 and 101.
- [10] C. Büchner, Z. Jun Wang, K. Burson, M-G. Willinger, M. Heyde, R. Schlögl, and H-J. Freund. A Large-Area Transferable Wide Band Gap 2D Silicon Dioxide Layer. *ACS nano*, pages A–H, 2016. Cited 2 times in pages 13 and 71.

- [11] L Lichtenstein, M. Heyde, and H-J Freund. Atomic Arrangement in Two-Dimensional Silica: From Crystalline to Vitreous Structures. *The Journal of Physical Chemistry C*, 116:20426–20432, 2012. Cited in page 15.
- [12] Leonid Lichtenstein. The structure of two-dimensional vitreous silica. Dissertation, Freien Universität Berlin, 2012. Cited in page 15.
- [13] N. Binggelli, N. Troullier, J. Martins, and J. Chelikowsky. Electronic properties of alpha-quartz under pressure. *Physical Review B*, 44(10):4771–4777, 1991. Cited 2 times in pages 15 and 70.
- [14] K. Mak, C. Lee, J. Hone, J. Shan, and T. Heinz. Atomically Thin MoS<sub>2</sub>: A New Direct-Gap Semiconductor. *Physical Review Letters*, 105:136805, 2010. Cited in page 15.
- [15] Y. Zhang, T. Chang, B. Zhou, Y. Cui, H. Yan, Z. Liu, F. Schmidt, J. Lee, R. Moore, Y. Chen, H. Lin, H. Jeng, S. Mo, Z. Hussain, A. Bansil, and Z. Shen. Direct observation of the transition from indirect to direct bandgap in atomically thin epitaxial MoSe<sub>2</sub>. *Nature Nanotechnology*, 9:111–115, 2013. Cited in page 15.
- [16] D. Qiu, F. da Jornada, and S. Louie. Optical Spectrum of MoS<sub>2</sub>: Many-Body Effects and Diversity of Exciton States. *Physical Review Letters*, 111:216805, 2013. Cited 3 times in pages 18, 48, and 70.
- [17] M. Ugeda, A. Bradley, S. Shi, F. da Jornada, Y. Zhang, D. Qiu, W. Ruan, S. Mo, Z. Hussain, Z. Shen, F. Wang, S. Louie, and M. Crommie. Giant bandgap renormalization and excitonic effects in a monolayer transition metal dichalcogenide semiconductor. *Nature Materials*, 13:1091, 2014. Cited 3 times in pages 18, 48, and 70.
- [18] A. Pedone, G. Malavasi, C. Menziani, U. Segre, and A. Cormack. Molecular Dynamics Studies of Stress-Strain Behaviour of Silica Glass under a Tensile Load. *Chemistry of Materials*, 20(13):4356, 2008. Cited 3 times in pages 18, 80, and 81.
- [19] Y. Tanaka, Y. Himuro, R. Kainuma, Y. Sutou, T. Omory, and K. Ishida. Ferrous Polycrystalline Shape-Memory Alloy Showing Huge Superelasticity. *Science*, 327:1488, 2010. Cited in page 18.
- [20] D. Mutter and P. Nielaba. Simulation of structural phase transitions in NiTi. *Physical Review B*, 82:224201, 2010. Cited in page 18.
- [21] A. Ferrari, D. Sangiovanni, J. Rogal, and R. Drautz. First principles characterization of reversible martensitic transformations. *Physical Review B*, 99:094107, 2019. Cited in page 18.
- [22] D. Jiang, J. An, Y. Liu, Z. Ma, F. Liu, H. Yang, X. Ren, K. Yu, J Zhang, X. Jiang, Y. Ren, and L. Cui. Nanocrystalline strain glass TiNiPt and its superelastic behaviour. *Physical Review B*, 104:024102, 2021. Cited in page 18.

- [23] Y. Wu, X. Zhang, and S. Pantelides. Fundamental Resolution of Difficulties in the Theory of Charged Point Defects in Semiconductors. *Physical Review Letters*, 119:105501, 2017. Cited 5 times in pages 19, 41, 44, 103, and 106.
- [24] K. Capelle. A bird-eye view of density-functional theory. *Brazilian Journal of Physics*, 36(4A):1318, 2006. Cited 2 times in pages 21 and 28.
- [25] R. g. Parr and W. Yang. *Density Functional Theory of Atoms and Molecules*. Oxford University Press, New York - Oxford, 1989. Cited in page 21.
- [26] P. Hohenberg and W. Kohn. Inhomogeneous electron gas. *Physical Review*, 136(3B):B864, 1964. Cited 2 times in pages 22 and 23.
- [27] W. Kohn. Nobel lecture:electronic structure of wave-matter functions and density functionals. *Review of Modern Physics*, 71(5):1523, 1999. Cited 3 times in pages 22, 23, and 24.
- [28] M. Levy. Universal variational functionals of electron densities, first-order density matrices, and natural spin-orbitals and solution of the v-representability problem. *Proceedings of the National Academy of Sciences of the United States of America*, 76:6062–6065, 1979. Cited in page 23.
- [29] M. Levy. The constrained search formulation of density functional theory. *in, Density Functional Methods in Physics*, pages 11–30, 1985. Cited in page 23.
- [30] E.H. Lieb. Density functional methods for coulomb systems. *in, Density Functional Methods in Physics*, pages 31–80, 1985. Cited in page 23.
- [31] W. Kohn and L. Sham. Self-consistent equations including exchange and correlation effects. *Physical Review*, 140(4A):A1133, 1965. Cited in page 24.
- [32] N. Ashcroft and D. Mermin. *Solid State Physics*. BROOKS/COLE, United States of America, 3 edition, 1976. Cited 2 times in pages 26 and 32.
- [33] C. Herring. New method for calculating wavefunctions in crystals. *Physical Review*, 57:1169, 1940. Cited in page 26.
- [34] J. M. Ziman. *Principles of the theory of solids*. CAMBRIDGE UNIVERSITY PRESS, Cambridge, 2 edition, 1972. Cited in page 26.
- [35] J. Phillips and L. Kleinman. New method for calculating wavefunctions in crystals and molecules. *Physical Review*, 116(2):287, 1959. Cited in page 26.
- [36] P. Gianozzi, S. Baroni, N. Bonini, M. Calandra, R. Car, C. Cavazzoni, D. Ceresoli, G. Chiarotti, M. Cococcioni, I. Dabo, A. Dal Corso, S. de Gironcoli, S. Fabris, G. Fratesi, R. Gebauer, U. Gerstmann, C. Gougoussis, A. Kokalj, M. Lazzeri, L. Martin-Samos, N. Marzari, F. Mauri, R. Mazzarello, S. Paolini, A. Pasquarello,

- L. Paulato, C. Sbraccia, S. Scandolo, G. Sclauzero, A. Seitsonen, A. Smogunov, P. Umari, and R. Wentzcovitch. Quantum espresso:a modular and open-source software project for quantum simulations of materials. *Journal of Physics:Condensed Matter*, 21:395502, 2009. Cited in page 27.
- [37] G. Kresse and J. Furthmüller. Efficient iterative schemes for ab initio total-energy calculations using a plane wave basis set. *Physical Review B*, 54(16):11169, 1996. Cited 2 times in pages 27 and 103.
- [38] J.M. Soler, E. Artacho, J.D. Gale, A. García, J. Junquera, P. Ordejón, and D. Sánchez-Portal. The siesta method for ab initio order-n materials simulation. *Journal of Physics:Condensed Matter*, 14:2745–2779, 2002. Cited 2 times in pages 27 and 48.
- [39] Richard M. Martin. *Electronic Structure:Basic Theory and Practical Methods*. Cambridge University Press, New York (USA), 2004. Cited in page 28.
- [40] L.D. Landau and E.M. Lifshitz. *Theory of elasticity*. Pergamon Press, Oxford and New York and Beijing and Frankfurt and Sao Paulo and Sydney and Tokyo and Toronto, 3rd edition, 1986. Cited 3 times in pages 29, 30, and 31.
- [41] R Feynman and Leighton R. *Feynman: Fisica, volumen 2:Electromagnetismo y materia*. Adisson Wesley Longman de Mexico, Mexico and Argentina and Brasil and Colombia and Costa Rica and Chile and Espana and Guatemala and Peru and Puerto Rico and Venezuela, 2nd edition, 1987. Cited in page 29.
- [42] A. Sutton. *Physics of elasticity and crystal defects*. Oxford University Press, Oxford, 1st edition, 2020. Cited 3 times in pages 29, 30, and 31.
- [43] E Kittinger, J Tichy, and E Bertagnolli. Example of a negative Poisson ratio. *Physical Review Letters*, 47(10):712, 1981. Cited in page 31.
- [44] K Nitin and J Chelikovsky. Anomalous elastic behaviour in crystalline silica. *Physical Review B*, 48(22):16227, 1993. Cited in page 31.
- [45] A Alderson and K Evans. Molecular Origin of Auxetic Behaviour in Tetrahedral Framework Silicates. *Physical Review Letters*, 89(22):225503–1, 2002. Cited in page 31.
- [46] Martin H Sadd. *Elasticity:Theory,Applications, and Numerics*. Elsevier, Amsterdam and Boston and Heidelberg and London and New York and Oxford and Paris and San Diego and San Francisco and Singapore and Sydney and Tokyo, 3rd ed. edition, 2014. Cited in page 32.
- [47] Ana Paula Moreira Barbosa. Estudo da Injeção de Carga em Nanotubos por Microscopia de Força Eléctrica. Dissertation, Universidade Federal de Minas Gerais, 2008. Cited in page 33.

- [48] D Drabold and Estreicher S. *Theory of Defects in Semiconductors*. Springer Verlag, Berlin Heidelberg, 2007. Cited in page 34.
- [49] A Fowler. A Semicentury of Semiconductors. *Physics Today*, 46:59, 1993. Cited in page 34.
- [50] F Seitz. Research on Silicon and Germanium in World War II. *Physics Today*, 48:22, 1995. Cited in page 34.
- [51] M Riordan and L Hoddeson. The Moses of Silicon Valley. *Physics Today*, 50:42, 1997. Cited in page 34.
- [52] I Ross. The Foundation of the Silicon Age. *Physics Today*, 50:34, 1997. Cited in page 34.
- [53] Marvin Cohen. The Oppenheimer Lecture by Professor Marvin Cohen: The Goldilocks Science. Cited in page 34.
- [54] J Weber, W Koehl, J Varley, A Janotti, B Buckley, C Van de Walle, and D Awschalom. Quantum computing with defects. *Proceedings of the National Academy of Sciences*, 107(19):8513, 2010. Cited in page 34.
- [55] F Bloch. Über die Quantenmechanik der Elektronen in Krustallgittern. *Zsitschrift für Physik*, 52:555, 1928. Cited in page 36.
- [56] R Hofstadter. Felix Bloch. A Biographical Memoir by Robert Hofstadter. *National Academy of Sciences*, 64, 1994. Cited in page 36.
- [57] Sokrates T. Pantelides. The electronic structure of impurities and other point defects in semiconductors. *Review of Modern Physics*, 50(4):797–858, 1978. Cited 4 times in pages 37, 38, 39, and 41.
- [58] J Sakuray and J Napolitano. *Modern Quantum Mechanics*. Cambridge University Press, United Kingdom, 2 edition, 2011. Cited in page 37.
- [59] G Baym. *Lectures on Quantum Mechanics*. Westview Press, New York, 1990. Cited in page 37.
- [60] O Madelung. *Introduction to Solid State Theory*. Springer Verlag, Berlin and New York, 1978. Cited 2 times in pages 37 and 38.
- [61] M. Lanoo and J. Bourgoin. *Point Defects in Semiconductors I: Theoretical Aspects*. Springer Verlag, Berlin Heidelberg New York, 1981. Cited in page 38.
- [62] W Kohn. Shallow Impurity States in Silicon and Germanium. *Solid State Physics*, 5:257, 1957. Cited in page 39.

- [63] W Kohn. Analytical Properties of Bloch Waves and Wannier Functions. *Physical Review*, 115(4):809, 1959. Cited in page 40.
- [64] L He and D Vanderbilt. Exponential Decay Properties of Wannier Functions and Related Quantities. *Physical Review Letters*, 86(23):5341, 2001. Cited in page 40.
- [65] M. Lanoo and J. Bourgoin. *Point Defects in Semiconductors I: Theoretical Aspects*. Springer Verlag, Berlin Heidelberg New York, 1981. Cited in page 40.
- [66] M.Dresselhaus, G. Dresselhaus, and A. Jorio. *Group Theory. Applications to the Physics of Condensed Matter*. Springer-Verlag, Berlin and Heidelberg, 2008. Cited in page 40.
- [67] A. OHara, B. Tuttle, X. Zhang, and S. Pantelides. Formation energies of charged defects in two-dimensional materials - resolution of long-standing difficulties. Cited 4 times in pages 41, 42, 44, and 106.
- [68] M.Leslie and M. Gillan. The energy and elastic dipole tensor of defects in ionic crystals calculated by the supercell method. *Journal of Physics C:Solid State Physics*, 18:973, 1985. Cited in page 42.
- [69] C. Castleton, A. Hoglund, and S. Mirbt. Density functional theory calculations of defect energies using supercells. *Modelling and Simulation in Materials Science and Engineering*, 17:084003, 2009. Cited in page 42.
- [70] C. Castleton, A. Hoglund, and S. Mirbt. Managing the supercell approximation for charged defects in semiconductors: finite size scaling, charge correction factors, the band gap problem, and the ab initio dielectric constant. *Physical Review B*, 73:032215, 2006. Cited in page 42.
- [71] G. Makov and M. Payne. Periodic boundary conditions in ab initio calculations. *Physical review B*, 51(7):4014, 1995. Cited in page 42.
- [72] S. Lany and A. Zunger. Accurate prediction of defect properties in density functional supercell calculations. *Modelling and Simulation in Materials Science and Engineering*, 17:084002, 2009. Cited in page 42.
- [73] Xia. Evaluation of charged defect energy in two-dimensional semiconductors for nano-electronics: the WLZ extrapolation method. *Annalen der Physik*, 532(3), 2020. Cited in page 43.
- [74] D. Wang, D. Hang, X. Li, S. Xie, N. Chen, W. Tian, D. West, H. Sun, and S. Zhang. Determination of formation energies of charged defects on two-dimensional materials. *Physical Review Letters*, 114:196801, 2015. Cited in page 43.

- [75] D. Wang, D. Hang, X. Li, N. Chen, D. West, V. Meunier, S. Zhang, and H. Sun. Charged defects in two-dimensional semiconductors of arbitrary thickness and geometry: formulation and application to a few-layer black phosphorus. *Physical review B*, 96:155424, 2017. Cited in page 43.
- [76] R. Weeks. Paramagnetic resonance of lattice defects in irradiated quartz. *Journal of Applied Physics*, 27:1376, 1956. Cited in page 47.
- [77] M. Stapelbroek, D. Griscom, E. Friebele, and G. Sigel. Oxygen-associated trapped-hole centers in high-purity fused silicas. *Journal of Non-Crystalline Solids*, 32:313–326, 1979. Cited in page 47.
- [78] D. Griscom. Electron spin resonance characterization of self-trapped holes in amorphous silicon dioxide. *Journal of Non-Crystalline Solids*, 149:137–160, 1992. Cited in page 47.
- [79] J. Götze, Y. Pan, and A. Müller. Mineralogy and mineral chemistry of quartz: A review. *Mineralogical Magazine*, 85:639–664, 2021. Cited 6 times in pages 47, 48, 50, 52, 55, and 69.
- [80] Z. Lu, C. Nicklaw, D. Fleetwood, R. Schrimpf, and S. Pantelides. Structure, properties, and dynamics of oxygen vacancies in amorphous SiO<sub>2</sub>. *Physical Review Letters*, 89:285505, 2002. Cited 3 times in pages 47, 48, and 52.
- [81] N Richard, L Martin-Samos, G Roma, Y Limoge, and J Crocombette. First principle study of neutral and charged defects in amorphous SiO<sub>2</sub>. *Journal of Non-Crystalline Solids*, 351:1825, 2005. Cited in page 47.
- [82] Y Martin-Samos, Limoge, J Crocombette, G Roma, N Richard, E Anglada, and E Artacho. Neutral self-defects in a silica model: A first-principles study. *Physical review B*, 71:014116, 2005. Cited in page 47.
- [83] R. Salh. Defect Related Luminescence in Silicon Dioxide Network: A Review. *Crystalline Silicon: Properties and Uses*, 2011. Cited in page 47.
- [84] A. El-Sayed, K. Tanimura, and A. Shluger. Optical signatures of intrinsic electron localization in amorphous SiO<sub>2</sub>. *Journal of Physics: Condensed Matter*, 27:265501, 2015. Cited in page 47.
- [85] D. Griscom, D. Brown, and N. Saks. *Nature or radiation induced point defects in amorphous SiO<sub>2</sub> and their role in SiO<sub>2</sub> on Si structures*, page 287. Cited in page 47.
- [86] M Boero, A Pasquarello, J Sarnthein, and R Car. Structure and Hyperfine Parameters of E1 centers in  $\alpha$ -Quartz and Vitreous SiO<sub>2</sub>. *Physical Review Letters*, 78(5):887, 1997. Cited 3 times in pages 47, 48, and 52.

- [87] L. Giacomazzi, L. Martin-Samos, A. Boukenter, Y. Ouerdale, S. Girard, and N. Richard. Epr parameters of e centers in v-SiO<sub>2</sub> from first-principles calculations. *Physical Review B*, 90:014108, 2014. Cited in page 47.
- [88] L. Giacomazzi, L. Martin-Samos, A. Boukenter, Y. Ouerdane, S. Girard, A. Alessi, S. de Gironcoli, and N. Richard. Photoactivated processes in optical fibers: generation and conversion mechanisms of twofold coordinated Si and Ge atoms. *Nanotechnology*, 28(19):195202, 2017. Cited in page 47.
- [89] A. El-Sayed, M. Watkins, V. Afanas, and A. Shluger. Nature of intrinsic and extrinsic electron trapping in SiO<sub>2</sub>. *Physical Review B*, 89:125201, 2014. Cited 3 times in pages 48, 69, and 70.
- [90] G. Pacchioni and A. Basile. First principle calculations of the optical properties of a neutral oxygen vacancy in ge-doped silica. *Journal of Non-Crystalline Solids*, 254:17–25, 1999. Cited 3 times in pages 48, 69, and 70.
- [91] H. Monkhorst and J. Pack. Special points for brillouin-zone integrations. *Physical Review B*, 13(12):5188–5192, 1976. Cited in page 48.
- [92] J.P. Perdew, K. Burke, and M. Ernzerhof. Generalized gradient approximation made simple. *Physical Review Letters*, 77:3865–3868, 1997. Cited in page 48.
- [93] N. Troullier and J. Martins. Efficient pseudopotentials for plane wave calculations. *Physical Review B*, 43(3):1993–2006, 1991. Cited in page 48.
- [94] H. Malekpour, P. Ramnani, S. Srinivasan, G. Balasubramanian, D. Nika, A. Mulchandani, R. Lake, and A. Balandin. Thermal conductivity of graphene with defects induced by electron beam irradiation. *Nanoscale*, 8:14608–14616, 2016. Cited in page 55.
- [95] M. Reticcioli, U. Diebold, G. Kresse, and C. Franchini. *Small polarons in transition metal oxides*. Springer Nature, Switzerland, 2019. Cited 2 times in pages 67 and 70.
- [96] A. Stoneham, J. Gavartin, A. Shluger, A. Kimmel, R. Muñoz, H. Ronnow, and C. Renner. Trapping, self-trapping and the polaron family. *Journal of Physics: Condensed Matter*, 19:255208, 2007. Cited 2 times in pages 67 and 70.
- [97] J. Laegsgaard and K. Stokbro. Hole Trapping at Al impurities in Silica: A Challenge for Density Functional Theories. *Physical Review Letters*, 86(13):2834, 2001. Cited 2 times in pages 69 and 70.
- [98] M. Avezac, M Calandra, and F. Mauri. Density functional theory description of hole trapping in SiO<sub>2</sub>: A self-interaction-corrected approach. *Physical Review B*, 71:205210, 2005. Cited 2 times in pages 69 and 70.



- [99] R. Nuttall and J. Weil. The magnetic properties of the oxygen-hole aluminium centers in crystalline  $\text{SiO}_2$ .i.[ $\text{AlO}_4$ ]. *Canadian Journal of Physics*, 59:1886–1892, 1981. Cited in page 69.
- [100] R. Nuttall and J. Weil. The magnetic properties of the oxygen-hole aluminium centers in crystalline  $\text{SiO}_2$ .iii.[ $\text{AlO}_4$ ]. *Canadian Journal of Physics*, 59:1886–1892, 1981. Cited in page 69.
- [101] J. Laegsgaard and K. Stokbro. Local chemistry of Al and P impurities in silica. *Physical Review B*, 61(19):12590, 2000. Cited 2 times in pages 69 and 70.
- [102] J. Laegsgaard and K. Stokbro. Electronic structure and hyperfine parameters of substitutional Al and P impurities in silica. *Physical Review B*, 65:075208, 2002. Cited 2 times in pages 69 and 70.
- [103] D. Han, D. West, X. Li, S. Xie, H. Sun, and S. Zhang. Impurity doping in  $\text{SiO}_2$ : Formation energies and defect levels from first-principles calculations. *Physical Review B*, 82:155132, 2010. Cited 2 times in pages 69 and 70.
- [104] M. dAvezac, M. Calandra, and F. Mauri. Density functional theory description of hole trapping in  $\text{SiO}_2$ : A self interaction corrected approach. *Physical Review B*, 71:205210, 2005. Cited in page 70.
- [105] P Grünberg. Nobel lecture: From spin waves to giant magnetoresistance and beyond. *Reviews of Modern Physics*, 80:1531, 2008. Cited in page 70.
- [106] J S Moodera, L R Kinder, T Wong, and R Meservey. Large Magnetoresistance at Room Temperature in Ferromagnetic Thin Film Tunnel Junctions. *Physical Review Letters*, 74(16):1531, 2008. Cited in page 70.
- [107] Y Lee, C Ahn, B Min, K Shin, J M Lee, K Lee, S Lim, S Park, Y Jo, J Langer, B Ocker, and W Maass. Critical switching current and thermal stability of magnetic tunnel junctions with uncompensated CoFeB/Ru/CoFeB synthetic free layers. *Journal of Applied Physics*, 113:093906, 2013. Cited in page 70.
- [108] E C Ahn. 2D materials for spintronics devices. *npj 2D Materials and Applications*, 4, 2020. Cited in page 71.
- [109] N Fajardo and R W Nunes. Carrier trapping centers in a two dimensional silica bilayer: Strongly localized shallow gap states and resonances induced by oxygen vacancies. *Physical Review B*, 106:155416, 2022. Cited 4 times in pages 71, 77, 78, and 86.
- [110] F. Molaei and H. Siavoshi. Molecular dynamics studies of thermal conductivity and mechanical properties of single crystalline  $\alpha$ -quartz. *Solid State Communications*, 320:114020, 2020. Cited 2 times in pages 79 and 80.

- [111] D. Löffler, J. Uhlrich, M. Baron, B. Yang, L. Lichtenstein, L. Heinke, C. Büchner, M. Heyde, S. Shaikhutdinov, H. Freund, R. Wlodarczyk, M. Sierka, and J. Sauer. Growth and Structure of Crystalline Silica Sheet on Ru(0001). *Physical Review Letters*, 105:146104, 2010. Cited 2 times in pages 81 and 83.
- [112] Z Gao, X Dong, N Li, and J Ren. Nobel Two Dimensional Silicon Dioxide with in-Plane Negative Poisson's Ratio. *Nano Letters*, 17:772, 2017. Cited in page 84.
- [113] J. Elguero and I Alkorta. Polyhedra, Tiles and Graphene Defects: The Case of Tetraoctite. *Mini-Reviews in Organic Chemistry*, 19(2):138, 2021. Cited in page 86.
- [114] L. Gomes, S. Alexandre, H. Chacham, and R. W. Nunes. Stability of Edges and Extended Defects on Boron Nitride and Graphene Monolayers: The Role of Chemical Environment. *The Journal of Physical Chemistry*, 117:11770, 2013. Cited in page 86.
- [115] Y. Wei, B. Wang, J. Wu, R. Yang, and M. Dunn. Bending Rigidity and Gaussian Bending Stiffness of a Single-Layered Graphene. *Nano Letters*, 13:26, 2013. Cited 2 times in pages 89 and 90.
- [116] C. Büchner, S.D. Eder, T. Nesse, D. Kuhness, P. Schlexer, G. Pacchioni, J.R. Manson, M. Heyde, B. Holst, and H.J. Freund. Bending Rigidity of 2d Silica. *Physical Review Letters*, 120:226101–1–226101–6, 2018. Cited in page 89.
- [117] T. Björkman, S. Kurash, O. Lehtinen, J. Kotakoshi, O. Yazyev, A. Srivastava, V. Skakalova, J. Smet, U. Kaiser, and A. Krashennnikov. Defects in bilayer silica and graphene: common trends in diverse hexagonal two-dimensional systems. *Scientific Reports*, 3:3482, 2013. Cited 2 times in pages 101 and 111.
- [118] A Souza, I Runger, C Pemmaraju, Schwingenschoegl, and S Sanvito. Constrained-DFT method for accurate energy-level alignment of metal/molecule interfaces. *Physical Review B*, 88:164112, 2013. Cited in page 103.
- [119] Q Wu and T Van Voorhis. Extracting electron transfer coupling elements from constrained density functional theory. *The Journal of Chemical Physics*, 125:164501, 2006. Cited in page 103.
- [120] B Kaduk, T Kowalczyk, and T Van Voorhis. Constrained Density Functional Theory. *Chemical Reviews*, 112:321, 2011. Cited in page 103.
- [121] P E Blöchl. Projector augmented-wave method. *Physical Review B*, 50(24):17953, 1994. Cited in page 103.
- [122] P E Blöchl, C Först, and J Schimpl. Projector augmented wave method: ab initio molecular dynamics with full wavefunctions. *Bulletin of Materials Science*, 26(1):33, 2003. Cited in page 103.

- 
- [123] K Duerloo, M Ong, and E. Reed. Intrinsic Piezoelectricity in Two-Dimensional Materials. *The Journal of Physical Chemistry Letters*, 3:2871, 2012. Cited in page 111.